Pulsatile Flow in a Conical Tube

by

Faouzi Trabelsi

A thesis submitted to the
School of Graduate Studies and Research
in partial fulfillment of the requirements
for the degree of

Master of Applied Science

Ottawa-Carleton Institute for Mechanical and Aerospace Engineering

Department of Mechanical Engineering
Faculty of Engineering
University of Ottawa
May 1993

ISBN 0-315-89720-1

Canada

UNIVERSITÉ D'OTTAWA
UNIVERSITY OF OTTAWA

To my Mother

for her Perpetual Love and Support

and

To the Memory of my Father

M.B.H. Trabelsi

Teacher and Friend

Abstract

Pulsatile flows occur in many biological and technological systems, most notably in the human cardiovascular system. The present study of pulsatile flow in a conical tube, although fundamental in nature, may be used to determine blood flow characteristics in cannulae; these are tubes used to connect a weak natural heart to an artificial heart ("inflow cannulae") and the artificial heart to the aorta ("outflow cannulae"). Hydraulic losses in a cannula must be minimal to ensure adequate blood flow, low trauma and good power efficiency.

For the experimental study, a transparent conical tube was connected to a mock circulation loop. Pulsatile flow was supplied by a pump ("artificial heart"), with controlled "pulse rate" and systolic time period ratio. Tests include flow visualization, pressure measurement with miniature piezo-resistive pressure transducers and velocity measurement with a two-component, frequency shifted, fibre optic, laser Doppler velocimeter. The results presented here were taken using water as a medium.

Flow visualization has revealed the formation of a high speed jet in the core of the conical tube during "diastole" as well as the appearance of separated and recirculating regions near the inclined wall. The formation of weak backflow ("regurgitation") was also observed during "systole", especially immediately upstream of the valve.

Pressure variation in the tube was fairly complex, containing substantial fluctuations that are caused by the opening and closing of the valve. Measurements of the axial velocity along the centerline of the test section demonstrate an emerging

downstream asymmetry of the "active" part of the velocity cycle, which is a clear indication of separation and recirculation in the conical tube. A large set of measurements have been analyzed in order to describe the detailed flow pattern during the cycle. Reverse flow took place at both the conical and the straight sections of the tube. However, in the conical section, the flow shows more unsteady and complex variation during the cycle. Also, the reverse flow near the wall region in the conical section occurred earlier in the diastolic phase, which is a clear indication of separation caused by the expansion.

Acknowledgements

The author wishes to express his sincere appreciation and gratitude to his supervisor, Dr. Stavros Tavoularis, for his continued support, guidance and understanding. Likewise, great appreciation is expressed to Dr. Tofigh Mussivand, as well as the Cardio-Vascular Devices Division of the University of Ottawa Heart Institute for their help and for providing the pump, valves and other components needed in the experiment.

Special thanks to all my friends, particularly to Mr. Sadok Guellouz, Mr. Tayeb Damerji, Mr. Elias Farah, Ms. Zeinab Keita, Mr. Brahim Chebbi, Mr. Youssef Touhammi, and Mr. Robert Tjoa, for their help.

Financial assistance by the Scientific Mission of Tunisia and the Natural Science and Engineering Research Council of Canada is greatly appreciated.

Finally, the author thanks his mother, his brothers and his sisters for their love and constant support.

Contents

List of Plates

List of Tables

List of Figures

Nomenclature

A	amplitude parameter
c	speed of sound
C, C_{blue}, C_{green}	calibration factors
d	beam separation
d_a	particle's aerodynamic size
d_f	spacing between fringes
d_g	particle's size, e.g. diameter of spherical particles
d_m	diameter of focussed laser beam
D	laser beam diameter defined to $\frac{1}{e^2}$ of maximum intensity
D_o	characteristic length
f	focal length of lens, also used as the frequency of the signal produced by a particle moving across the fringe pattern
f_D	Doppler frequency
f_s	frequency shift
h_m	height of the measuring volume
H	inflow head
l_m	length of measuring volume

L	pipe length, also used as a characteristic length
L_u	unsteady entry length
LDA	laser Doppler anemometry
n, n_1, n_2, n_f	indices of refraction
N	number of fringes in the measuring volume
N_p	number density of particles in the flow
P_o	initial Pressure
P_1, P_2, P_3, P_4	positions of pressure measurements
ΔP	pressure Variation
r	tube inner diameter
R	Reynolds number
R_{ave}	average Reynolds number
R_c	critical Reynolds number
R_δ	Reynolds number based on Stokes layer thickness
R_m	modified Reynolds number for slowly varying cross section
R_p	peak Reynolds number
S	distance between two fringes
t	time
t_1, t_2,..., t_{19}	intervals of time used to analyze one cycle of pulsation
u_{pp}	fluctuating velocity in streamwise direction from peak to peak
u_x	velocity in the free stream just outside the boundary layer
U	instantaneous velocity in the streamwise direction
$\hat{U}$	cross sectional mean velocity amplitude

U_b	bulk velocity
U_s	steady component of the instantaneous local velocity of the pulsatile flow
U_t	oscillating component
V	measuring volume, also used as velocity of particle moving normal to the fringes, also used as the instantaneous velocity in the azimuthal direction

Greek symbols

α	frequency parameter or Womersley number
$\frac{\alpha}{2}$	Bragg angle
δ	Stokes layer thickness
Δ	parameter representing the order of magnitude of the rate of change of the pipe radius for slowly varying cross section
θ	angle of intersection of the laser beams, also used as taper angle
θ_1, θ_2	angles of incidence of light rays
θ_{1c}	critical incidence angle
λ	laser light wavelength, also used as Stokes parameter
λ_A	acoustic wavelength
ν	kinematic viscosity
ρ	particle or fluid density
ω	angular frequency of oscillation

Chapter 1

Introduction

1.1 Motivation for the Present Investigation

The function of the heart is to keep blood flowing through the circulatory system. The heart actually consists of two separate pumps, known as the right ventricle and left ventricle, as shown in figure 1.1. The right ventricle pumps blood from the systemic circulation into and through the lungs, while the left ventricle pumps blood from the lungs through the remainder of the body and back again to the heart. Thus, the blood flows around a continuous circuit. Figure 1.2 shows the functional details of the heart as a pump.

Cardiac failure is one of the leading causes of death in North America. The term cardiac failure means depressed pumping effectiveness of the heart, and its most frequent cause is actual damage to the heart itself by some disease process. When it is primarily the left side of the heart that is failing, the right ventricle may continue to pump blood into the lungs with normal vigor, while the left ventricle is unable to move the blood on into the systemic circulation (figure 1.1).

The resulting accumulation of blood in the lungs increases the pressure in all the pulmonary vessels and engorges them with blood. If the pressure becomes high enough, fluid will leak out of the pulmonary capillaries into the lung tissues and even into the air spaces of the lungs, resulting in pulmonary edema. To prevent such problems, a partial artificial heart pump, replacing the left ventricle, can be used to pump the blood into the systemic circulation at normal rates. For this purpose, the left ventricle is connected to the artificial heart through a tube called "inflow cannula" or "inflow conduit" as shown in figure 1.3. The output of the artificial heart is connected to the aorta through an "outflow conduit". In other words, the task of the left ventricle is limited only to pump the blood into the artificial heart through the inflow cannula.

In cases when these cannulae present high flow resistance, the blood flow rate pumped to the artificial heart may decrease below the level required for normal operation. Therefore, it is important to maintain hydraulic losses through the cannulae as low as possible.

Several other problems are encountered when using these cannulae, such as thrombogenesis, hemolysis and platelet activation. These complications are related to the dynamics of blood flow through the cannulae, or as they are sometimes called, the hemodynamic parameters, including turbulence, recirculation, shear stress and stagnation. Thrombogenesis, which is the formation of blood clots, can take place in the regions of recirculation. In addition, regions of high shear stress and stagnation may destroy the red cells by disrupting the integrity of the cell membrane, known as "hemolysis", as well as cause platelet activation, which

may trigger the coagulation process to cause thrombogenesis and possible death. Therefore, flow characteristics through cannulae must be investigated, with the objective to produce designs and operating conditions that minimize turbulence, recirculation, stagnation and high shear stresses, in order to reduce thrombogenesis and other malformations.

Inflow cannulae are available in different shapes, as shown in figure 1.4; however, they generally appear as short, curved and tapered tubes. Despite their importance, a survey of published literature on blood flow through cannulae has not revealed any readily available detailed study.

Although this project did not focus on heart valves, their operation influences the flow in cannulae. Due to their important role, the development of artificial heart valves has become a major biomedical activity during the last few decades. Such valves are made from both biomaterials or tissues. Some of the thromboelism problems (e.g. hemolysis) are directly related to the hemodynamics of these valves (see Yoganathan et.al., 1983). Several types of commercial valves are shown in figures 1.5, 1.6, 1.7, 1.8 and 1.9.

1.2 Objectives

The first objective of the present work was to assemble and test all equipment required, in order to create a reliable facility for experimental research on pulsatile flow through cannulae. This included an artificial heart pump and its driving

system, a mock circulatory system, a laser Doppler velocimetry system and other minor accessories.

As a main objective, it is intended to measure the pulsating velocity field in an idealized model of a cannula under conditions simulating, as much as possible, artificial heart implantation. Furthermore, it is intended to measure the pulsating pressure at the ends of the cannula, using sensitive pressure transducers, in order to determine, if possible, the pressure drop through the cannula over the period of the pumping cycle and the nature of the pressure variations.

These results are expected to be useful in understanding blood flow in cannulae and in establishing the useful ranges of operation of existing models and could serve as a guide for the design of more efficient products.

It is anticipated that the present study will lead to further use of the facility in research on the fluid dynamics of artificial hearts and other cardiac assist devices and on pulsatile fluid flow in different types of biological systems.

Chapter 2

Literature Review

2.1 Classification of Periodic Flows in Tubes

Periodic flows in tubes can be divided into two classes, depending on whether the time-averaged velocity is zero or not. (a) Pulsatile or pulsating flows, in which the instantaneous local velocity consists of a component, U_t, oscillating with time, superposed on a steady component, U_s. Pulsatile flows can be laminar, transitional or turbulent. Three similarity parameters are commonly used to describe such flows: the average Reynolds number, R_{ave}, the frequency parameter, α (to be defined later), and the amplitude parameter, A, of the oscillations. (b) Oscillating or oscillatory flows, in which the steady velocity is zero ($U_s = 0$). An oscillating flow can be considered as a particular case of pulsating flow and it is commonly described with the use of two similarity parameters, the peak Reynolds number, R_p, and the frequency parameter, α.

Laminar pulsatile flow can, in many cases, be adequately resolved analytically. However, analysis of turbulent pulsatile flow is much more difficult and generally

requires experimental knowledge of some of the properties of the flow.

2.2 Periodic Flows in Tubes with a Uniform Cross Section

Grace (1928) and Szymanski (1930) have analytically determined the laminar oscillatory flow of a Newtonian fluid in a round tube with a uniform cross section, disregarding end effects.

Grace (1928) found that, for very slow oscillatory motion along a uniform circular tube, the velocity distribution resembled that for steady motion along the tube, the velocity being in phase with the applied oscillatory force. As the period of oscillation decreased, the magnitude of the velocity in the central region of the tube tended to become uniform and the breadth of this central region gradually increased, while the phase of the velocity tended to lag more and more behind that of the applied force.

Szymanski (1930) examined unsteady, incompressible, viscous flow in a cylindrical tube. His objective was to obtain the exact solutions for the Stokes equations (for $R \ll 1$, in which case inertia is negligible), which constituted the generalization of the well-known Poiseuille solution, representing laminar steady flow of a viscous fluid in a circular tube. He assumed the velocity of the fluid to be always parallel to the axis of the tube and to be initially zero. He also considered the pressure difference at the ends of the tube to be a known and given function of

time. First, he found the solution to the problem in a series form and he showed how the laminar flow developed from rest. Then, he demonstrated that, at infinite time, the solution tended uniformly to the Poiseuille solution.

Richardson and Tyler (1929) appear to be the first to have conducted an experimental investigation of oscillatory pipe flow. Hot-wire measurements were obtained of the transverse velocity profiles near the mouth of a square tube, 48 mm wide. The alternating flow was produced by an electric motor oscillating a disc at the end of a long crank with an adjustable stroke. A peak of high average velocity was found near the walls of the pipe. The measured velocity profiles showed the same trends that the analytical solution predicted for oscillatory flow in a round pipe.

Womersley (1955) derived theoretical equations for pulsatile laminar flow in rigid straight tubes. These equations gave the fluid flow rate as a function of the pressure gradient-time relationship, pulse frequency, fluid properties, and tube radius. Also, they gave the fluid velocity as a function of the above quantities and the radial position in the tube. It was shown that there is a phase-lag between the motion of the liquid and the pressure gradient which causes it. Womersley assumed that, for laminar pulsatile flow in a straight rigid tube, the radial and azimuthal components of the velocity and pressure gradient are zero. Then, starting from the equations of motion, he obtained a linear form of the Navier-Stokes equations, which he solved by assuming a sinusoidal time-dependent pressure gradient to get the velocity and the total flow rate as functions of time. These functions depend on a dimensionless parameter, α, which characterizes laminar pulsatile flow. This

parameter, called the Womersley number, is defined as

$$\alpha = r(\omega/\nu)^{1/2} \tag{2.1}$$

where r is the tube inner radius, ν is the kinematic viscosity of the fluid and ω is the angular frequency of oscillation (in radians/second). If the frequency ω is zero, then α is zero and therefore the total flow rate reduces to the familiar form for Poiseuille flow. It is recalled that the Stokes layer was defined for the flow near an oscillating flat plate (Stokes'second problem) as the layer carried by the wall motion and having a thickness of the order

$$\delta = (\nu/\omega)^{1/2} \tag{2.2}$$

This is called the "Stokes layer thickness" and decreases with decreasing kinematic viscosity and increasing frequency. Thus, the Womersley number can be written as

$$\alpha = r/\delta \tag{2.3}$$

To examine critically the theoretical equations derived by Womersley, Linford and Ryan (1965) carried out some flow measurements in laminar oscillatory pipe flow. The test apparatus used consisted essentially of a straight tube in which the pulsatile flow could be observed, a pulsatile flow generator (reciprocating piston in a cylinder driven by an adjustable cam on a variable-speed drive) and means for measuring flow rate, local velocity (using photography), and pressure gradients (using two pressure transducers) as functions of time. The flow channel was a glass tube, 25.4 mm in diameter, 6400 mm long and terminated at one end by a vented reservoir. A computer program based on Womersley's equations was used

to calculate the fluid flow rate and velocity profile from the pressure gradient-time relationship, fluid properties and tube radius. Thus, a comparison between measured and calculated values of flow rate and velocity could be made. Both calculations and data agreed within the estimated experimental error, thus providing evidence for the validity of Womersley's equations in the range of α from 1.83 to 21.0. In addition, in spite of the fact that these equations are properly applicable only to laminar flow, they gave a good agreement with the data collected in turbulent flow, which occurs for high α.

Predicting the transition from laminar to turbulent flow is a difficult problem, requiring experimental results. Experiments on this subject have been conducted by Sergeev (1966), Merkli and Thomann (1975), Hino et al. (1976), Grassman and Tuma (1979) and Ohmi et al. (1982).

Sergeev (1966) conducted his experiment in a test stand consisting of a glass pipe with bellows connected to it. The oscillations of the bellows and the fluid in the pipe were recorded by means of a strain gage, amplifying bridge and an oscillograph. The observations were made for both free oscillations of the fluid and kinematically forced oscillations created by a motor and a crank mechanism. Pipes with diameters 12.1, 8.6, 6.0 and 3.8 mm and with heights in the range between 175 and 1000 mm were used. The amplitudes and circular frequencies of the oscillations were from 3.0 to 300.0 mm and from 4 to 25 sec^{-1} respectively, which corresponded to values of the Womersley parameter, α, between 4 and 40 and of the Reynolds number, R, between 50 and 30×10^3. By increasing the oscillation frequency (thus, increasing α) transition from the laminar to turbulent

regime of fluid oscillations was observed very clearly. The critical values of the Reynolds number, R_c, corresponding to this transition, in the above range of α and R, were approximately proportional to the number α, as

$$R_c = 700\alpha \tag{2.4}$$

It was concluded that the transition to turbulence in oscillatory flow in round tubes is a function of α, whereas the flow regime (laminar or turbulent) is a function of both α and R.

Merkli and Thomann (1975) performed a similar experiment, for which they used air in a tube closed at one end and driven by an oscillating piston at the other end. A piezo-electric pressure transducer was used to measure oscillation frequency. The amplitude of the piston was between 2.85 and 13.8 mm and the frequency of the piston motion was between 0 and 817 rad/sec. Both hot wire anemometry and flow visualization techniques were used to describe the flow pattern and its stability. The hot wire was positioned very close to the tube wall to detect turbulence, because the boundary layers were very thin. For flow visualization, the tube was made of plexiglas, a plane was illuminated by a stroboscope synchronized with the piston motion and cigarette smoke was used. This study considered two possible forms in which turbulence may occur: (a) as turbulent flow throughout the whole cycle of oscillation; or (b) as turbulent bursts, followed by relaminarization during other parts of the same cycle. After conducting the experiments, it was concluded that only the second case occurred. Furthermore, vortex patterns were observed along the tube wall. The main observations of this study were that transition occurred in the Stokes layer and that the critical Reynolds

number was

$$R_c = 400\alpha \tag{2.5}$$

which had the same order of magnitude as the one found earlier by Sergeev (1966). Furthermore, it was clear that turbulence occurred in the form of periodic bursts, which were followed by relaminarization in the same cycle and did not lead to turbulent flow during the whole cycle. Finally, it was noticed that the flow was disturbed by the hot wire probe and that these disturbances became larger at higher frequencies of oscillation.

One year later, Hino et al. (1976) performed experiments on transition to turbulence in a purely oscillating pipe flow, for values of the Reynolds number R_δ, based on the Stokes-layer thickness δ and the cross-sectional mean velocity amplitude, $\hat{U}$, from 13.4 to 1081.9 (or R, based on the pipe diameter and $\hat{U}$, from 105 to 5830) and for values of the parameter α from 1.91 to 8.75. Lucite circular pipes were used with inner diameters of 14.5 and 29.7 mm and lengths of 4000 and 6000 mm. The pipes were connected to a piston chamber in which the piston was driven by a constant speed electric motor, whose rotating period was varied by exchanging the gear-box attachment. A hot wire anemometer was used to measure the velocity. Three types of turbulent flow regime were detected: weakly turbulent flow, conditionally turbulent flow and fully turbulent flow. Therefore, the types of oscillatory flow may be classified in terms of the Reynolds number, R or R_δ, and the Stokes parameter, λ, into : (a) laminar flow, (b) disturbed laminar flow, (c) weakly turbulent flow, (d) conditional turbulence and (e) fully turbulent flow, based on the experimental results summarized in a stability diagram on λ, R or

λ, R_δ plots (figure 2.1). The first transition from laminar flow to distorted laminar flow or weakly turbulent flow appeared in the accelerating phase of the cycle and its critical Reynolds number decreased as λ (or α) increased. In the conditionally turbulent flow, turbulence was generated suddenly in the decelerating phase and the velocity distribution changed drastically, whereas the flow relaminarized during the acceleration phase. This type of transition seems to have a close connection with the phenomenon of relaminarization or reverse transition. For this regime, a critical Reynolds number of $R_{\delta c} = 550$ was found , but it applied only to cases with λ greater than 1.6.

Similarly, Grassmann and Tuma (1979) measured the transition from laminar to turbulent flow for oscillating and pulsating flow within a pipe by means of the electrolytic method. They concluded that for the oscillating flows the critical Reynolds number, R_c, depends on the amplitude and the frequency of the oscillation. In addition, pulsating flows were found to depend also on the superimposed stationary flow.

Ohmi et al. (1982) conducted an experiment similar to that of Hino et al. (1976). Velocity distribution and pressure gradient were measured over wide ranges of Reynolds number and dimensionless frequency (Womersley number α). To obtain the wall shear stress, experimental values of the cross-sectional mean velocity and pressure gradient were substituted into an unsteady momentum integral equation. Frictional losses and four describing characteristic parameters of the flow pattern were calculated. In the laminar regime, the measured quantities of Ohmi et al. (1982) agreed with the values obtained from their laminar the-

oretical solutions. Meanwhile, the turbulent regime was well represented by the turbulent quasi-steady relations. This turbulent quasi-steady state is defined here as the state in which a relationship between cross-sectional mean velocity and wall shear stress for steady turbulent pipe flow holds at any moment in the cycle. Affirmatively, it was found that the characteristic parameters and friction factors can be calculated from their individual turbulent quasi-steady relations with sufficient accuracy in the range of Reynolds number R sufficiently larger than the critical value, $R_c = 800\ \alpha$. The realization of turbulent quasi-steady state was obtained for $R \gg 2800\ \alpha$ when α is between 4 and 24. In the turbulent regime, where turbulent bursts followed by relaminarization in the same cycle occur, the instantaneous velocity distribution was found to obey the well known 1/7 power law in the phase where turbulence appears and the extent of turbulent phase increased with R.

Gerrard (1971) conducted an experimental investigation of pulsating turbulent water flow in a tube. The mean flow Reynolds number was 3770 and the tube diameter was 38 mm. An oscillating piston in simple harmonic motion with a 12 sec period was used to produce the pulsations. Flow visualization was obtained by means of a wire stretched across the tube, using the thymol blue technique. Cine-photography was used to find the convection velocity which was assumed to be the flow speed. This technique could not distinguish velocity direction and so reverse flow had to be avoided. Therefore, this factor limited the acceptable range of Reynolds number, the frequency and the amplitude of oscillations. In the case of laminar flow, the velocity profile changed because vorticity production at the

wall was constantly changing and vorticity diffused across the flow. Increasing the Reynolds number to the transitional range showed the effect of pulsation on the turbulent structure. In this range, the flow appeared almost laminar for nearly half the cycle, but the velocity profile was essentially a turbulent one with relatively weak laminarization. At high enough Reynolds number the structure of the turbulence changed during the cycle of pulsation. The intensity of turbulence diminished during acceleration (tendency towards laminarization) and increased during deceleration.

As mentioned earlier, most of the measurements described above were taken far away from the entrance of the tube. The first experimental investigation dealing with oscillatory flow in short pipes was conducted by Parato et al. (1986) in an apparatus consisting of interchangeable test pipes of 38.8 mm inside diameter and varying length-to-diameter ratios from 9.60 to 57.6, connected between two large alternately pressurized reservoirs at frequencies between 0.63 and 2.62 rad/sec. The alternating pressures were obtained by the movement of a double-acting variable-stroke hydraulic cylinder. The working fluid was air (assumed to be incompressible), moving with a maximum velocity of 2.13 m/s. Velocity and pressure were measured using hot wire anemometry and temperature-compensated strain gauge transducers, respectively. The flow under consideration combines simultaneously effects of convective and temporal accelerations. Therefore, it is not readily tractable by closed-form mathematical analysis and experiments were required to get the necessary information. Over the whole range of the experimental variables, the results of the velocity measurements indicated that the flow

was never fully developed. The boundary layer thickness was expected to increase with frequency. However, the boundary layer thickness was found to increase till the midpoint of pipe length and after that it was decreasing. This was a result of the reciprocating nature of the flow. In addition, it was found that the longitudinal pressure gradients in the unsteady boundary-layer flow were sensitive to the effects of temporal acceleration, i.e. the effects of temporal acceleration on the correction coefficients for pressure drop along the tube were orders of magnitude greater than their convective counterparts.

Fishler and Brodkey (1990) investigated the transitional and turbulent oscillatory flow in a rigid pipe with long entry sections. The experimental procedure was to suspend tracer particles in a Newtonian fluid to mark the fluid motions, to illuminate the fluid and particles and to take high speed motion pictures of the fluid motions in a moving frame. The flow was driven by a simple harmonic motion of a piston and cylinder. The objective was to obtain a better visual picture of the phenomena occurring in oscillatory flow. For this type of flow, the two similarity parameters needed were R_p (peak Reynolds number based on the maximum velocity and the diameter of the pipe) and the Womersley number, α. The values of R_p and α were varied independently from 7200 to 22000 and from 6.6 to 16.6, respectively. These values corresponded to the range where transition to turbulence occurred. Coherent flow structures for transitional and turbulent oscillatory flow were presented and it was noticed that they occurred randomly, but deterministic sequences of events were also observed in the flow. These oscillatory flow structures were compared with other results from the literature for

pulsatile and oscillatory flow and with the previously determined steady turbulent flow structures. Also, the variation of turbulence according to the flow structures with R_p and α was discussed. It was found that the oscillatory flow structures were a series of deterministic events (as mentioned earlier), like the steady turbulent flow structures. However, the oscillating events were not totally random in time and space, in contrast to the events observed in steady turbulent flow, but they exhibited time dependence that was phase locked with the deceleration part of the cycle. The values of similarity parameters for which these structures were readily observable were $R_p = 22000$ and $\alpha = 11.6$. Five events were postulated: local deceleration, local acceleration, excitation-transverse vortex, ejection and sweep. During local deceleration, it was observed that the fluid near the wall was moving slower than the fluid at a previous time in the same position. This phase exhibited a normal turbulent velocity profile with the region of steep velocity gradient shifted away from the wall. Following the local deceleration phase, large inflows towards the wall were observed, known as local acceleration. This phase was caused by the large velocity gradient in the retarded region, combined with the instability of the locally decelerated flow. Local accelerations were observed to originate upstream from the retarded region near the wall and they interacted with the retarded fluid and accelerated it. The third observed event of the flow structure (i.e. the excitation-transverse vortex) was a combination of two separate events. Whenever a transverse vortex or vortices were observed, it was always at the same time as the excitation event. The latter caused fluid in the wall region to mix. It is characterized by random chaotic radial motion throughout the entire

wall region. Meanwhile, the transverse vortices were observed to occur simultaneously with the excitation event and appeared as vortical structures which were being convected downstream. The fourth event (ejection) was characterized by a large amount of radial motion. However, unlike the random chaotic motions of the excitation event, ejections were always directed downstream away from the wall, as opposed to local accelerations which were directed towards the wall. The position of origin of the ejections was anywhere in the wall region and the position of termination was usually outside or in the outer portion of the wall region. Following ejection, the sweep phase took place, which was simply the return of the flow field to basically rectilinear motions until the next sequence of events. This phase was mainly associated with the relaminarization effect. The above study documented the coherent nature of distinct events during a cycle. Local acceleration, excitation and ejection events were characterized by large radial motions of the fluid and were believed to play an important role in the generation of turbulence. In addition, it was noticed that turbulence activity decreased with increasing α and increased with increasing R_p. The observations done in this study were compared to some results of previous investigators, with which they were found to be in good agreement. Finally, using the transitional and turbulent oscillatory flow structures as a measure of the degree of turbulence, they concluded that these structures were a good indicator of the transition to turbulence.

Grotberg (1991) conducted an experiment on transition to turbulence in oscillatory pipe flow. It was designed to identify the parameter range over which transition to turbulence occurs and to demonstrate whether or not, on transition

to turbulence, the core region in a volume-cycled oscillatory pipe flow retains its structure as an inviscid plug showing no instability. The test section consisted of a cylindrical pipe of diameter D = 31.75 mm bored inside two 254 mm long plexiglas plates bolted together. The connecting tubes used were of sufficient length for the flow to be fully developed when it entered the test section. A piston was used to generate the sinusoidal motion of the fluid through the tube. It was driven by an electric motor and a scotch yoke system. The working fluid chosen for the LDV measurements was an aqueous solution of potassium thiocyanate (KSCN), with the salt concentration adjusted to allow index of refraction matching between the plexiglas tube and the fluid to within 0.05%. The working fluid was Newtonian with a kinematic viscosity of 2.29 mm^2/s. The axial velocity was measured at radial positions across the diameter of the tube for a range of amplitude, A (defined as the ratio of the stroke distance over the tube radius), between 2.4 and 21.6 and for a range of α between 9 and 33. It was observed that for large α the boundary layer became thinner. For $R_\delta = 854$, it was evident that the flow near the wall region showed some instability, which arose during the deceleration phase and did not persist during the acceleration phase. In other words, the flow appeared to relaminarize during the accelerating part of the cycle, as found previously by Hino et al. (1976). However, this instability (turbulence) during the decelerative phase did not penetrate into the core region of the flow, which remained laminar. Turbulence was confined to an annular region, which had a thickness that was a few times larger than the Stokes layer thickness. This finding was in contradiction with the previous studies and was observed for all $R_\delta > 500$. Transition to turbulent

boundary-layer flow occurred during the decelerating phase of fluid motion for R_δ between 500 and 854. The critical value of $R_{\delta c} = 500$ was in accord with the value found by Sergeev (1966).

2.3 Periodic Flows in Tubes with Variable Cross Section

When a purely oscillatory viscous flow is set up over a curved surface or in a channel or tube of varying cross section, the Reynolds stresses associated with the oscillatory motion of the fluid in the Stokes layer at the surface generate a steady component of velocity which persists away from the layer because of the action of viscosity. This generated (rectified) flow pattern is called steady streaming. Rayleigh (1884), in his study of the circulation of air observed in Kundt's tubes and on some allied acoustical problems, was the first researcher who referred to the streaming phenomenon as acoustic streaming. Schlichting (1932) did an analysis of an oscillatory circular cylinder in a viscous fluid at rest and observed the streaming phenomenon in the exterior flow.

The first researcher to do analysis on streaming in a pulsatile flow was Hall (1974). His analysis was limited to unsteady viscous flow in a pipe of slowly varying cross section (wavy wall). He used the so-called "Lubrication Theory" to obtain the first order steady streaming generated by a purely oscillatory pressure difference maintained between the ends of a pipe of slowly varying cross section.

It was assumed that the pipe radius variations were small compared with the characteristic thickness of the Stokes layer associated with the flow. For that, a parameter Δ, representing the order of magnitude of the rate of change of the pipe radius was defined by

$$\Delta = \frac{D_o^2}{L^2} \tag{2.6}$$

where D_o and L are characteristic lengths in the r and z directions, respectively, in a cylindrical co-ordinate system (r,θ,z). Thus, Δ was assumed to be smaller than unity to satisfy the condition of small variations of the tube cross section. This method required that the modified Reynolds number, R_M, defined as

$$R_M = \frac{U D_o^2}{L\nu} \tag{2.7}$$

associated with the flow, must be small (U is a typical axial velocity). Hall (1974) formulated the non-dimensional equations governing the flow and solved the limiting case of "Stokes Flow", which is the case when $R \ll 1$, i.e. when the viscous effects are dominating and inertia is negligible (R_M=0, Δ=0). Then, using a corrected Stokes flow form, he found the steady streaming and evaluated it for the high and low frequency limits. For large α, the Stokes layer thickness associated with the oscillatory motion of the fluid was found very small compared with a typical value of the pipe radius. Thus, the flow field was split into separate regions: the Stokes layer and the outer layer. However, for small α the Stokes layer was found to completely fill the pipe and there was no need to split the flow field. It was noticed that in both the low and high α limits the geometry of the pipe was crucial in determining the nature of the induced steady streaming. He concluded that because of the difference in the mean radii of the pipe ends, a velocity compo-

nent representing a steady flow towards the wider end of the pipe was generated. However, when this difference was zero, then the steady streaming consisted only of the regions of recirculation, confined between the nodes of the wavy wall of the tube in the Stokes layer region. In the high α limit, solutions were obtained in the Stokes and outer layers separately and then were matched where the layers met. The above generated velocity component dominated the steady streaming compared to the streaming caused by the Stokes layer associated with the oscillatory motion of the fluid on the wavy tube wall. In the low α limit, the two types of steady streaming were of the same order of magnitude.

Transition to turbulence in a model of the human superficial femoral artery was experimentally studied by Buss (1983) . The artery was approximated by a linearly converging tapered tube with a taper of 0.024 rad. The oscillatory component of the flow was provided by a scotch yoke and flywheel arrangement, which transmitted a simple harmonic motion to a piston. A neutrally buoyant dye (thymol blue) was used in the water for flow visualization. Observations were made of a mean plus oscillatory flow, which approximated the mean and fundamental of the flow wave in the superficial femoral artery. The inlet and outlet pipes were made sufficiently long for the flow to be fully developed at the working section (tapered tube). The mean velocity was calculated from the measured rate of the volume flow collected in a measuring device and the oscillatory flow velocity was calculated from the piston amplitude and the angular frequency of the flywheel. Axisymmetric vortex formation, separation and transition to turbulence were observed during the cycle. It was found that, due to the taper, the flow

changed from a dominant frequency parameter (α) dependence at the proximal end of the conical section to a Reynolds number (R) dominance at the distal end of the tube. The flow was found to depend on three parameters: the peak Reynolds number times the taper angle, $R_p\ \theta$, the frequency parameter, α, and the amplitude parameter, defined as the ratio of the peak to the mean velocities. The flow cycle was divided into four phases called respectively the distal, proximal acceleration, vortex formation and transitional phases. In the distal phase the entire flow was found to be unidirectional. Vorticity was diffused across a greater portion of the radius along the tube and the flow was in one direction until, at nearly the end of the tube (exit of the tube, smaller cross section), vorticity was diffused to the axis of the tube and the flow was quasi-steady. In this phase the effect of taper was to increase the wall shear stress. In the second phase, the proximal acceleration phase, the flux was reversed in the entrance tube direction (wider section). The flow was laminar and attached, whereas for the same steady flow over the same range of Reynolds number occurring in this phase the flow was not attached. So it was concluded that some separation and reattachment occurred in the flow. The vortex formation phase followed, characterized by the occurrence of the streaming phenomenon. It was observed that, as the flow was moving backwards to the tube entrance direction, there was some tendency for the streamlines to congregate about the axis of the tube as the boundary layer thickened. Streaming was found to depend on the Reynolds number and the taper angle. The formation of vortex was always accompanied by a region of the flow reversal for a wide range of Reynolds number and α. Due to this flow reversal, some

separated region existed at certain distances from the entrance of the tapered tube. The last (transitional) phase was characterized by the instability of the vortex for which the flow became transitional resulting in a brief period of turbulence due to subsequent decay of eddying as the flux decelerated to zero. These eddies died away because the quiescent free stream could not feed them. The free stream continued to decelerate and the flow was relaminarized soon after the start of reacceleration.

Budwig (1985) conducted an experimental investigation on unsteady heat transfer in laminar oscillatory flow in straight and conical tubes. The flow was driven by a 51 mm diameter piston in a cylinder. The piston was driven in sinusoidal motion by a scotch yoke. Three differently shaped test sections were used in the experiment: a uniform cross section tube, a 4 degree included angle conical tube, 610 mm long and a 12 degree angle conical tube, 500 mm long. To minimize end effects, the tubes were placed far away from the entrance. The fluid point displacements were obtained by hydrogen bubble visualization in water and the velocity field by hot wire anemometry in air. It was found that the radial profiles of axial displacement over one cycle, measured for an α range of 14 to 97, drifted in some regions in both tapered tubes as compared to measured profiles taken in straight tubes. This result was observed by the time lines generated by hydrogen bubble wire across the tube. Therefore streaming was very clear and evident.

Chapter 3

Experimental Apparatus and Instrumentation

3.1 Mock Circulatory System

The flow through the present model of a cannula was generated by a mock circulation loop, driven by an artificial heart pump. This loop consists of an atrial tank, a compliance tank, a systemic resistance and connectors, as shown in figure 3.1.

3.1.1 Atrial Tank

This tank consists of a plexiglas rectangular reservoir, with a 150 mm inside width, a 300 mm height and a 14 mm thickness, whose top is at atmospheric pressure. The atrial tank plays the role of the diseased heart and it provides a supply of fluid with nearly constant pressure, which simulates the arterial pressure.

The proper pressure is accomplished by leveling the fluid free surface. This tank is connected to the artificial heart inlet port through an inflow cannula. The inflow pressure was found to vary between 346.6 and 2666 Pa (2.6 - 20 mmHg).

3.1.2 Compliance Tank

This tank is sealed (closed) and it was tested for air and water leakage. It has the same size as the atrial tank, but it is pressurized, in order to simulate the capacitance of the blood vessels, thus serving as a systemic compliance. An air bleeding valve was installed at the top of the tank for controlling the height of the liquid and consequently the desired air volume. A pressure gauge was also installed at the top of the tank for measuring the air pressure. This tank is connected to the outlet port of the artificial heart through an outflow cannula and to the systemic resistance through another port.

3.1.3 Systemic Resistance

This system was constructed from flexible tubes of different sizes connected in parallel. It is used to control the flow rate and to maintain the afterload pressure at a certain level by changing its resistance to the flow. This systemic resistance system is connected to the atrial tank through a rotameter, which gives a direct reading of the flow rate.

3.2 Blood Pump and its Driving System

A duplicate of the pneumatic pusher plate blood pump of the Cleveland Clinic Foundation was used as the artificial heart. As shown in figure 3.2, the pump was connected to the mock circulatory system such that its inlet port was connected to the atrial reservoir through the inflow cannula and its outlet port to the compliance tank through an outflow cannula.

The pump consists of a housing (chamber), a diaphragm and a pusher plate. It is driven by a system consisting of solenoid controlled valves for pulsation of the drive pressure. These two-way solenoid valves are activated by a signal with a voltage between 0 and 6 volts, which regulates the valve opening and closing duration. The air passes through the solenoid valve and enters the pusher plate cylinder, pushing the piston and diaphragm upwards, which, in turn, push the working fluid to the compliance tank (systolic phase). As the pusher plate moves downwards (diastolic phase), the working fluid from the atrial reservoir pushes the inlet valve and refills the pump chamber.

A driver control circuit unit (Mussivand, 1988) provides an electronic regulation to control the pulse rate (4.2-16.7 rad/sec), drive pressure (34474 to 344740 Pa) and systolic time period ratio (10-60 %), the values of which are given by a digital meter.

A Hall effect sensor (American Aerospace Controls Model HI-5), mounted in the pump housing, and a magnet, bound to the pusher plate, measured the pusher plate/diaphragm displacement as shown in figure 3.3.

3.3 Artificial Heart Valves

A bileaflet valve (figure 1.7) was used in this experiment. It was mounted between the wider end of the test section and the inlet port of the pump. The leaflet mechanism consists of two lateral protrusions contained in butterfly shaped pivot recesses in the orifice ring. In the closed position, the leaflets meet the housing at a $30 - 35^{\circ}$ angle (figure 1.7c). The leaflets pivot within grooves made in the valve orifice housing and are designed to be fully open at an angle of 85°, providing three orifices through which the working fluid flows. At the outlet port of the pump a different type of valve was used. It was a rubber disc valve.

3.4 Test Section

Even though a variety of cannulae have been used in vivo, no specific and detailed research has been done to optimize their sizes and shapes. Typical commercial cannulae range in length from 50 to 350 mm, inner diameter from 6 to 35 mm and bending angle from 0 to 90 deg. The choice of geometry depends on the patient's heart condition, size and position. The outer diameter at one end has to be as small as possible, in order to minimize damage to the natural heart. The diameter at the other end has to be equal to the diameter of the outlet port of the artificial heart, which is larger by comparison. Gradual tapering of the cannula from the larger to the smaller end is preferable to sudden reduction, as the former

results in smoother blood flow.

Laser Doppler Anemometry (LDA) requires optical access to a flow . For this reason, the models of the inflow cannulae (test section) were constructed from transparent materials. Both glass and clear perspex were tried as materials for the test section. Using a glass blower machine, four Pyrex tubes were shaped to the desired tapered shape with different bends but with the same diameters and lengths (see figure 3.4 for dimensions). Another tapered tube was cast from transparent acrylic resins (RTV 60). To minimize the refraction of light, the external surfaces of the tube were made flat. In addition, a tube was machined from plexiglas with flat external surfaces, as shown in figure 3.5, which also shows the shape and dimensions of the tubes connecting the inflow tank and the test section. While using the LDA system for measuring the velocity through the pyrex tubes, some problems were encountered, mainly the refraction of the light due to waviness of the tube surface, caused by the glass blower. Furthermore, the point of intersection of the laser beams was displaced due to the curvature of the tube and the differences in the indices of refraction of air, glass and liquid. To avoid these problems it was decided to use test sections with plane outer surfaces and, if possible, to match the index of refraction of the liquid with that of the wall.

3.5 Flow Visualization Equipment

A Minolta X-700 camera was used for close-up photography of the flow con-

trolled and driven by a Minolta motor drive 1, which provided the ability of taking 3 photos per second in one shot. A cylindrical lens mounted in front of a 10 mW Helium-Neon laser provided a laser sheet for illumination. A Panasonic video camera was used for recording the flow. It was equipped with a macro-zoom lens permitting close-up photography of the desired region of the test section. A film with high sensitivity (35 mm ASA 1600) was used.

3.6 Pressure Instrumentation

Two piezoresistive full bridge pressure transducers (ENDEVCO model 8500) were used for measuring pressure variation in the cannula during the pumping cycle. One transducer was installed at the entrance of the test section, whereas the second one was installed at the outlet of the test section, as shown in figure 3.6. The two taps shown in the figure were machined directly on the test section and no intermediate tubes were used. Rough estimates of the pressure tap/transducer system and of the time delay for the transmission of pressure fluctuations to the transducer (Doebelin, 1990) gave values that were several orders of magnitude lower than the discretization time and, thus, negligible. Therefore, the response of the pressure transducers was not affected. Air was removed from the tap chamber as the water escaped from it before introducing the pressure transducer. The pressure transducers had a range of 13.8 kPa (2 psi) and a sensitivity of around 1.09×10^{-5} V/Pa (150 mV/psi). Two pressure indicators (model 4428) were used.

They were calibrated to operate with a matched transducer each, according to the manufacturer's instruction manual. Each indicator provided an analog voltage output of 5 V full scale, which was digitized and processed using a micro-computer, and a frequency response of 30 kHz. After calibration, each indicator was set to the specifications of the corresponding pressure transducer. An independent calibration was performed using a known hydrostatic head, measured by a height gauge. A typical calibration curve for the transducers is shown in figure 3.7.

3.7 Laser Doppler Anemometry

The Laser Doppler Anemometry (LDA) system was supplied by DANTEC ELECTRONICS Inc. As shown in figure 3.8, it consisted of a solid state, switching power supply (Model 5400), a laser head (ILT 5000), LDA optics, fiber flow optics, and a particle dynamics analyzer (PDA) system. Both the laser head and the power supply were manufactured by Ion Laser Technology company (ITL). The laser head is capable of generating laser radiation in the 457nm to 514.5 nm range. Its power ranges from 10 mW to 100 mW. The laser beam generated by the laser head is passed through the LDA optics (DISA 55 × MODULAR LDA OPTICS), which consists of:

- one DANTEC 55 × 25 Beam Splitter
- one DANTEC 55 × 29 BRAGG CELL
- one DANTEC 55 × 27 Beam Splitter (color)

- one DANTEC 55 × 35 Color Separator
- one DANTEC 55 × 34 Photomultiplier Optics System
- two DANTEC 55 × 08 Photomultiplier Sections

The 55 × 25 Beam Splitter consists of a neutral beam splitter and a reflection prism for a 50:50 % splitting of the common beam. It creates two beams, separated by 30 mm. The separated beams were passed through the two holes of the Bragg Cell, used to shift the frequency of light waves in one of the beams. The Bragg Cell is an opto-acoustic device, in which ultrasonic energy is propagated transversely to a laser beam to divide it into several beams with different frequencies and directions. The diffracted beams coming out of the Bragg Cell have the same optical properties as the incoming beams and cause no deterioration of the performance of the laser Doppler system. To start the Bragg Cell, an input power was provided from the PDA system (Bragg Cell Drive is 40 MHz). The two beams coming out of the Bragg Cell pass through the 55 × 27 Beam Splitter, which is a color separating type. One of the two beams passes through without any changes, whereas the second beam (cyan) is separated into a green (514.5 nm) and a blue (488 nm) beam, both parallel to the optical axis. This beam splitter consists of one color beam splitter prism and three reflection prisms. At this point, there are three parallel beams, a green one, a blue one and a reference cyan beam.

All three beams are passed through the Fiber Flow Optics Section (DANTEC 60 × Fiber Flow probes), which consist of:

- one 60 × 32 X-optics Adaptor

- three 60 × 24 Manipulators
- one 60 × 31 Probe Distribution Box
- one 60 × 11 Probe Head (60 mm probe)
- one 60 × 20 Front Lens with a focal length of 159.9 mm.

Each beam passing through a 60 × 24 Manipulator is adjusted to the optimum angle and position, so that it is focussed on the optical fibre with maximum intensity. The 60 × 24 Manipulators are mounted at the ×-optics with the 60 × 32 ×-optics Adaptor. After passing through the transmitting fibres, the three laser beams are fed to the 60 × 31 Probe Distribution Box, which serves as an interface between the transducer head (probe head), the transmitting fibres and the receiving fibre. From this Box the laser beams are passed to the 60 × 11 Probe Head through a fibre optical cable. The probe head is a 2-D probe based on color separation and it is designed for LDA flow measurements in the backscatter mode (in the experiment it is used in the forward scatter mode). In this transducer head the beams are recollimated to be parallel to each other. The 60 × 20 Front Lens focuses the beams and establishes a well specified measuring volume. After focusing the beams in the measuring point, the 55 × 34 PM OPTICS were used in the forward scatter mode to focus the measuring volume in the correct image size on the pinhole disk. Therefore, the light scattered by the flow particles is recollimated and fed to the 55 × 35 Color Separator. The latter consists of a color beam splitter and a reflection prism. It is mounted together with × 36 Interface Filter (blue-488nm), × 37 Interface Filter (green-514.5nm), and an × 08

PM section after each filter. Each of the two collected light colors corresponds to the velocity of the flow in some direction; in this case, green light corresponds to the transverse direction and blue light to the streamwise direction. The × 08 PM section provides an alternating current whose frequency is proportional to a component of the flow velocity at the measuring point.

To process the signals coming out of the × 08 PM section and to determine the corresponding flow velocities, the Particle Dynamics Analyzer (PDA) system was used for most measurements. This system provides the flow velocity from the frequency of the Doppler Burst. Mainly, the PDA system consists of a PDA Signal Processor, Velocity Channels extensions kits, an Interface and an ADC (Analog to Digital Converter) system. The 58G110 Interface is used to connect the 58N10 PDA Signal Processor to a computer. All instrument settings such as bandwidth, gain and high voltage are controlled from the computer. Appropriate software was supplied with the PDA system. It controls setup, data acquisition and processing functions (there is no front panel control or display on the PDA Signal Processor). This software has been designed for use with a PC-AT type computer running with the DOS operating system. It is written in FORTRAN 77 and Assembler programming languages. The ADC system allows the computer to read the anode current of the photomultipliers. Preceding data acquisition, this ADC is also used to check that the high voltage outputs are at selected levels and that the internal supply voltages are correct. The PDA processor has individual voltage power supplies for each photomultiplier tube (PMT) used in the system. The high voltage can be set from 0 to 2000 volts in 8 volts increments. The processor is used

with the Bragg Cell as mentioned earlier which produces an optical frequency shift of 40 MHz and extends the use of the system to the measurements of reversing flow.

To describe accurately the flow field within the test section, simultaneous measurements of the velocity field, pressure variation and pusher plate/diaphragm displacement were necessary. However, the PDA signal processor output cannot be synchronized with analog signals. Therefore, a different method was used for processing the Doppler signals. The outputs of the × 08 Photomultiplier Sections were processed by two Doppler frequency trackers (DANTEC 55 N 20). These devices have a frequency range of 1 kHz to 10 MHz, covered by seven range segments. They contain the following modules:

- one 55 N 21 Tracker Main Unit comprising:
  - one Main Frame
  - one Power Supply
  - one Tracker
  - one IEEE-488 Interface
- one 55 L 97 High Voltage Supply; this module is used for measurements made with the connected photomultiplier
- one 55 N 24 Display Module; this module is used for displaying mean velocity during a time interval determined by the front-panel control setting.

The analog outputs of the frequency trackers were displayed on an oscilloscope and digitized by an analog to digital converter connected to a personal computer

system. This system permitted simultaneous measurements of several signals, corresponding to velocity, pressure and diaphragm displacement. Electronic and optical frequency shifts were applied to the Doppler signals. The optical shift was generated by the Bragg Cell, which was activated by the 55 N 10 frequency shifter. The electronic shift was the input signal to the tracker, supplied directly from the DANTEC 55 N 10 frequency shifter. The above frequency shifts extend the use of the system to permit the measurements of reversing and low velocity flows. The frequency shifter consists of the following main block units:

- one Frequency Shift Generator Unit
- one Fixed Divider Board
- one LM Exciter
- one Mixer Unit
- one Power Supply

The used output signals generated from this system were:

- one 40-MHz signal from the Bragg Cell
- one DC power from the Bragg Cell power amplifier

The input signals from the system were:

- two Photomultiplier output signals
- two DC anode currents

- one Power Supply

The laser head, the LDA optics and the Fiber Flow optics were mounted on an optical DANTEC Bench to insure alignment. The Probe Head was mounted on a 3-D traversing system to enable positioning of the measuring volume within the test section. The photomultiplier (DANTEC 55 × 34 PM OPTICS and 55 × 08 PM SECTION) was mounted in a forward position on a separate support for appropriate application. The flow apparatus, including the test section, was fixed on a rigid table to minimize vibrations.

3.8 Traversing System

A 3-D traversing system was assembled to be used for the precise displacement of the Probe Head to ensure accurate positioning of the measuring volume within the test section (see figure 3.9 for details). It consists of a trapezoidal lead screw, an optical jack and a transverse traversing system. The optical jack (OPTIKON) is mounted on a table fixed on the trapezoidal lead screw. The latter translates the Probe Head measuring volume longitudinally in the test section tube with a 0.025 mm precision. The jack provides a 100 mm vertical displacement of the Probe Head with a 0.05 mm precision. The transverse traversing system (MITUTOYO) is mounted on the jack and provides a 300 mm maximum displacement with a 0.01 mm precision.

Chapter 4

Background Information and Experimental Procedures

4.1 Blood Properties

Blood is involved in many physiological functions, the most important being the transport of oxygen and carbon dioxide between the lungs and the cells of tissues. Historically, investigations into the mechanical properties of blood have continued in parallel with investigations towards mathematical modeling of arterial blood flow. A summary of the blood composition and its hemodynamic properties is presented below. This material was chosen mainly from the texts by Dinnar (1981) and Fung (1981 and 1984).

1. Composition : Blood consists of a suspension of a variety of cells in an aqueous solution (plasma) of organic and inorganic substances (electrolytes and nonelectrolytes). The plasma occupies approximately 45% . The volume ratio of the cells over the whole blood is normally around 55%. The latter fraction is referred to as the hematocrit. The plasma contains about 91%

water and 9% solids. The red cells occupy an overwhelmingly large proportion of the total volume of cells (91%). White cells of various categories and platelets comprise the remaining cellular fraction. The numbers of white cells and platelets are normally not large enough to affect the fluid dynamic behavior of blood, but platelets may seriously interfere with flow as they play an important role in the formation of blood clots.

2. Viscosity : Although plasma is a Newtonian fluid, the whole blood is non-Newtonian, because of the suspended cells (Fung, 1981). It can be characterized as a pseudo-plastic liquid, because its viscosity decreases as the velocity of flow increases. A comparison of Newtonian and non-Newtonian behavior is illustrated in the rheogram for different types of flow behavior, shown in figure 4.1. An estimate of the absolute viscosity of the blood is 3.5 Cp (centipoise, $1Cp = 10^{-3}$ kg/m.s) and that of the plasma is between 1.8 and 2.5 Cp (see table 4.1).

   Discussions on the effect of suspensions on the viscosity of blood are given by Caro (1978) and Goldsmith and Skalak (1975). The effective viscosity of the suspension always exceeded that of the suspending fluid, as a result of deformation of suspended particles and friction which produces higher local shear rates and corresponding increases in rate of energy dissipation. The increase in viscosity due to the presence of suspended cells is illustrated in figures 4.2 and 4.3. Figure 4.2 shows the variation of apparent viscosity as a function of hematocrit and shear rate in a small diameter tube. It is seen that the apparent viscosity decreased as the velocity of the flow increased and that

for shear rates lower than a threshold value, depending on the hematocrit, the effective viscosity decreased significantly with increasing shear. This decrease in viscosity can be attributed to the axial accumulation of cells (Rudinger, 1966). As the velocity of the flow increases; there is a tendency for the cells to move towards the axis of the tube, increasing the hematocrit there, while lowering it near the wall. Figure 4.3 illustrates the variation of apparent blood viscosity as a function of hematocrit and capillary diameter at high shear rates. It indicates an increase of viscosity with the concentration of cells and the effect of the tube diameter. The blood viscosity was seen to increase with the diameter of the tube. This effect is also shown in figure 4.4. It is known as the Fahreus-Linquist effect.

From the above discussion, it can be seen that the blood viscosity depends on the shear rate, hematocrit and tube diameter. Fung (1981) has proposed a constitutive relation for blood which describes a strain rate dependent viscosity for the whole blood. He noticed that, at high shear rates, the whole blood behaves like a Newtonian fluid with a constant coefficient of viscosity, while at low shear rates, non-Newtonian behavior of blood can be described by the proposed constitutive relation. Therefore, he concluded that for large diameters of vessels, exceeding 100 μm, the wall shear strain rate of blood is high enough to assume an effectively homogeneous blood with constant viscosity. This assumption appears to apply to blood flow in an artificial heart inflow cannula, because the diameter of the tube used is large enough (minimum diameter of 13 mm) and the shear rate in such conditions is not

low.

4.2 Flow in the Entrance Region

All the work done previously by many researchers is conducted for fully developed flows far from the entrance region. However, in the present work, the flow measurements are taken at the entrance region, which has a behavior more complicated because, in addition to the flow being time-dependent, it is also developing axially. For a steady flow in a straight tube, the entrance length is defined as the distance from the entrance of the tube to the location where the boundary layers occupy the entire tube. In periodic flow, the velocity distribution is a function of time as well as a function of location, so the shape of the velocity profiles in the developing region varies widely and at any given instant of the cycle it may be blunt, parabolic and even partly or fully reversing direction. In this case, the entrance length for the oscillatory component of the flow is defined as the distance from the entry of the tube to where the boundary layer thickness becomes equal to the thickness of the fully developed oscillatory flow boundary layer (Fung, 1984). When these two boundary layers merge into one, the unsteady entry length, L_u, is found as

$$L_u = 2.64\frac{u_x}{\omega} \tag{4.1}$$

where u_x is the velocity in the free stream immediately outside the boundary layer. In the straight section of the tube used in the present work, the heart rate was

about 1 Hz and the amplitude of the largest unsteady velocity component was about 2.5 m/s, so that the largest possible instantaneous value of L_u is about 1 m, which is larger than the total length of the test section and its connecting tube to the inflow tank (240 mm). See figure 5.4 for exact entrance conditions. However, for most of the cycle, because the instantaneous value of u_x is small, the unsteady entrance length will be much smaller. The latter will be zero during flow reversal. The entrance length is found by Fung (1984) to be shorter for periodic flow than that for steady flow. This is expected if one thinks of periodic flow as if it were a steady flow which had not had sufficient time to become established. The mean flow will continue to develop beyond the entrance length but its development would not be affected by the oscillatory components, because far from the entrance the oscillatory boundary layer would be much thinner than the developing boundary layer.

4.3 Advantages and Requirements of LDA

Compared to hot-wire/hot-film anemometry; Laser Doppler Anemometry (LDA) has the following advantages:

- It provides direct measurement of velocity, through its relationship to a measurable frequency and thus it does not require calibration.
- No probe needs to be inserted in the flow, thus LDA does not obstruct the flow in any way, except for the need for insertion of flow tracing particles.

However, the use of LDA requires a transparent test section and a transparent working fluid with an index of refraction, matched, if possible, to that of the test section. It also requires "seeding" of the flow with fine particles.

4.4 Liquids Tested for Refractive Index Matching

From appendix B one can conclude that, for a convenient and accurate optical measurement, it is necessary to match the indices of refraction of the test section material and the liquid. Several available liquids that have a suitable index of refraction have been considered and tested, but they were rejected as having an extremely high viscosity, being highly corrosive to some of the materials of the system or being very toxic and hazardous. Some of these liquids are presented in table 4.2. Therefore, the results presented in this work were taken using water as a medium.

4.5 Particle Selection

The source of the signal in LDA is the scattering particle. Geometric and physical parameters of the particles influence the quality of electric signals obtained from the photomultiplier of the LDA system.

In the case of water flow in the forward scatter mode, the natural particles occurring in the fluid were adequate as seeds. However, the present experimental conditions required that the flow should be further seeded to provide adequate data rates and good signal quality, especially in the case of the backward scatter mode.

The requirements of seed particles for successful LDA measurements can be summarized as follows. They have to be small enough to follow the flow, but large enough to generate sufficient scattered light. In addition, the number concentration, ability to survive the environment, and toxicity are important aspects that can influence the choice of the seed material. The single parameter that determines whether the particle is following the flow is the particle's aerodynamic size, d_a, is given by

$$d_a = d_g \rho^{1/2} \tag{4.2}$$

where ρ is the particle density and d_g is its size, e.g. the diameter of spherical particles. Seed particles with a small aerodynamic diameter are desirable because they follow the flow readily. The desired particle concentration in the flow depends on the type of signal analysis. Often, the desirable situation is to find one and only one particle in the measuring volume, while still maintaining a high data rate. The probability of finding one and only one particle in the measuring volume is greatest when $N_p V = 1$ where N_p is the number density of particles in the flow and V is the measuring volume. If several particles in the measuring volume are required, as in the present case, then $N_p V \gg 1$.

Different seeding particles have been used in previous applications, some of

which are listed in table 4.3. For flow visualization, aluminium flakes were used as tracers as they were available and produced strong light reflection. However, for velocity measurements, the flow was seeded with silicon carbide particles, approximately 1.5 μm in diameter. These are suitable for measurements in both liquids and gases. Their high refractive index (n = 2.65) is useful in obtaining good signals in water (n = 1.33) even in back scatter operation. They were supplied as a dry powder but they were mixed with water in a small container to form a suspension before being dispersed into the flow. Their aerodynamic size, d_a, was very small and the condition $N_p V \gg 1$ was verified to assure that more than one particle were at all times present in the measuring volume.

4.6 System Parameter Calculations

From equation A.1, it can be seen that the velocity V normal to the fringes is proportional to the Doppler frequency shift, f_D, by a constant or calibration factor, C, given by

$$C = \frac{\lambda}{2 \sin \frac{\theta}{2}} \tag{4.3}$$

The calibration factor must be provided as input to the frequency tracker and the data acquisition program, so that a direct reading of the instantaneous value of the velocity is provided as output. The focal length of the lens influences the intersection angle θ, and thus the calibration factor, C. If d is the aperture, f is the focal length and λ is the wavelength, then from geometry the calibration factor is

given by

$$C = \frac{\lambda}{2}\sqrt{1 + \frac{2f^2}{d}} \tag{4.4}$$

In the present system, f = 159.9 mm, d = 26.87 mm and λ = 488nm (blue beam) or 514.5 nm (green beam); therefore, C_{blue} = 2.9143 m/s per MHz and C_{green} = 3.072 m/s per MHz.

4.6.1 Probe Volume

The probe volume is defined as the volume within the $\frac{1}{e^2}$ boundary of the optical fringe modulation. For laser beams whose intensity profile in the transverse direction has a Gaussian shape, the probe volume is an ellipsoid, as shown in figure 4.5. The probe volume parameters are

- The diameter of the focussed laser beam,

$$d_m = \frac{4f\lambda}{\pi D} \tag{4.5}$$

  where f is the focal length of the lens and D is the diameter of the beam, before passing through the transmitting lens, usually defined as the distance between points with intensity $\frac{1}{e^2}$ of the maximum intensity.

- The length of the measuring volume,

$$l_m = \frac{d_m}{\sin\frac{\theta}{2}} \tag{4.6}$$

- The height of the measuring volume,

$$h_m = \frac{d_m}{\cos\frac{\theta}{2}} \tag{4.7}$$

- The spacing between the fringes,

$$d_f = \frac{\lambda}{2\sin\frac{\theta}{2}} \tag{4.8}$$

d_f is equal to the calibration factor, C, because the velocity of a particle crossing the control volume is equal to the distance between two fringes divided by the time period or multiplied by the frequency. By dividing the height of the control volume, h_m, by the fringe spacing, d_f, the number of the fringes along the measuring volume can be estimated as

$$N = \frac{h_m}{d_f} = \frac{4}{\pi}\frac{d}{D} \tag{4.9}$$

Therefore, the number of fringes depends only on the aperture, d (beam separation), and the beam diameter, D. In the present work the focal length was f = 159.9 mm and the aperture was d = 26.87 mm. For the green laser beam (λ = 514.4 nm), d_m = 0.0776 mm, l_m = 0.927 mm, h_m = 0.0776 mm and d_f = 3.072 μm. For the blue laser beam (λ = 488 nm), d_m = 0.0736 mm, l_m = 0.879 mm, h_m = 0.0736 mm and d_f = 2.9143 μm. The number of fringes obtained is N = 25.

4.7 Flow Visualization Methodology

The frame camera and the video camera were placed on a tripod above the test section and the laser was placed in front of the test section to provide a thin

horizontal light sheet for illumination of the flow in the conical tube. All the other light sources were turned off. Black paper was used on the sides and the bottom of the test section to eliminate all unwanted light reflections. A sufficient quantity of aluminium powder was mixed with the water to provide enough light for visualization.

Chapter 5

Measurements

5.1 Experimental Conditions

A typical range of operating conditions of an inflow cannula connected to an artificial heart in clinical use (during surgery) is as follows (see Mussivand, 1988). The pump should beat at between 70 to 80 beats per minute, with a 30% systolic time period ratio. The pressure (afterload, corresponding to the pressure in the compliance tank) resulting from ventricle contraction is normally 16 kPa (120 mm Hg) and approximately 10.7 kPa (80 mm Hg) during ventricle relaxation. The artificial heart should deliver more than 4 liters of blood per minute. A diseased heart operates at an average pressure as low as 1000 Pa (7.5 mm Hg) to pump the blood to the pump. This pressure corresponds to an inflow tank head, H, of 102 mm.

For each set of measurements, the entire loop was filled with water through the atrial tank. After all connections were checked for leaking, the residual air was bled from the tubes, test section, pump and the connections to the pressure transducers

to ensure normal operation and consistent experimental conditions. The water temperature inside the loop at the start and near the end of the measurements was typically $23°C$ and $25°C$, respectively. In order to reduce the disturbances that might be caused by the impurities and bacteria formation after long use, the water was distilled and deionized. Its kinematic viscosity was determined to be 8.97 x10^{-7} m^2/s. The only foreign matter present in the water was the seeding particles.

Under the operating conditions of the experiment, the pulse rate of the solenoid controlled valve driver was adjusted to 60 bpm (beats per minute, 1000 ms per cycle) with a systolic duration of 400 ms, that is a systolic time period ratio of 40 %. The driving pneumatic pressure was set to a maximum of 206.85 kPa (30 psi). For higher pressures and lower systolic time period ratios, the pump failed to perform. Due to these limitations, the mean flow rate through the mock-circulatory system was limited to a maximum of 3.4 l/min (liters per minute) and it dropped as low as 1.6 l/min. Meanwhile, the pressure in the compliance tank was maintained between 10.7 kPa (80 mm Hg, diastolic pressure) and 16 kPa (120 mm Hg, systolic pressure), that is an average of 13.33 kPa, in order to meet the physiological blood pressure requirements. The inflow pressure, simulating the atrial pressure, was set to 1471 Pa, corresponding to a water level (head, H) of 150 mm. At normal physiological blood flow conditions, the pump should deliver around 5 l/min. The pump used in this study failed to perform at such a flow rate. Therefore, the physiological requirements were not completely met. However, this should not affect much the general flow pattern within the conical tube.

The pressure transducers were calibrated and placed at the desired positions of measurements. The laser system and all its controls were checked and connected to the data acquisition system.

5.2 Diaphragm Position

Synchronization of pressure and velocity measurements was achieved by using the signal from the Hall effect sensor, representing the pusher plate/diaphragm displacement (figure 5.1). The pulsating cycle was divided into two parts, systole (40%) and diastole (60%). The latter starts with the plate at its top position moving downwards, as the heart chamber is getting filled, and ends when the plate reaches its lowest position. The systolic phase starts with the plate at its lowest position, moving upwards, as the pump discharges the fluid, and ends when the plate reaches its top position.

During a pulsatile flow cycle, 20 discrete values of each signal evenly spaced in time (50 ms) from the begining of diastole to the end of systole, as shown in figure 5.2, were used to analyse the flow during the cycle.

5.3 Flow Visualization

Photographs of the flow inside the test tube were taken with the stills camera viewing the flow at a right angle to the plane of the laser sheet. Aluminium powder mixed with water was added occasionally into the circulation loop in order to get clear photos. Photographs were taken at shutter speeds of 1/15, 1/30, 1/60, 1/125, 1/250, 1/500 and 1/1000 sec using 35 mm ASA 400, 1000 and 1600 films. The camera shutter was synchronized, as much as possible, with the pumping cycle of the heart. A total of 8 films were used.

The flow patterns were captured as pathlines on still photography representing sections of the trajectories of individual particles. These were images of the flow patterns within the test section during systolic and diastolic phases. Plate 1 shows the flow field in a large part of the conical section of the tube at different times within the same cycle. These photos were taken at a shutter speed of 1/60 sec with the ASA 1600 film. Plates 1a show the flow field during early diastole, while Plate 1b and 1c during late diastole and Plate 1d during systole. Synchronization of the first photo (Plate 1c) was achieved by using a stop watch. It was taken between t10 and t11 (0.53 sec). Plates 1d, 1a and 1b were taken at equal intervals of time of 1/3 sec fixed by the camera drive. That is, Plate 1d was between t17 and t18 (0.86 sec), while Plates 1a and 1b were in the following cycle, with Plate 1a taken at around t4 (0.2 sec) and Plate 1b at around t10 (0.5 sec).

The patterns during several cardiac cycles were recorded using a videotape camera for several minutes. The flow patterns in the videotape showed a good

agreement with those in the photographs.

5.4 Pressure Measurements

Pressure measurements were recorded simultaneously with the pusher plate/diaphragm displacement at four locations P1, P2, P3 and P4 as shown in figure 5.3. Positions P1 and P2 represent the entrance and the exit of the conical tube respectively. P3 was in the heart chamber and P4 at the outflow tube.

The signal from the Hall effect sensor, representing the pusher plate/diaphragm displacement, was synchronized with the pressure measurements in order to show the pressure pattern at specific instants within the cardiac cycle.

Fluctuating pressure measurements at P1 and P2 were carried out for inflow heads, H, of 100, 150 and 250 mm of water and pulse rates, f, of 60, 80, 100 and 120 bpm (beats per minute). Table 5.1 provides the coordinates of the points of pressure measurements at P1 and P2. Figure 5.4 shows some sample pressure measurements at P1 and P2. Simultaneous measurements of pressure at P2 and pusher plate/diaphragm displacement are shown in figure 5.5. Pressure measurements in the heart chamber (at P3) are also shown in figure 5.6a, while pressure measurements at the outflow conduit (P4) are shown in figure 5.6b.

The pressure measurements will be discussed in the next chapter.

5.5 Velocity Measurements

Streamwise velocities across the test tube were measured. The velocity synchronization with the pusher plate is shown in figure 5.7. Table 5.2 and figure 5.8 provide the coordinates and the numbers of both the points and the radial profiles of the axial velocity measurements. A total of 17 profiles were determined, from which the first two were in the tube's straight section, whereas the rest were in its conical section. Due to the conical shape of the tube, the Womersley number, α, defined by equation 2.1, varies from one profile to the other. The radius, r, varied from 6.5 mm to 12.25 mm from the first to the last profile. This created a relatively wide Womersley number range, between 17.2 and 32.4, based on the pulsation rate, ω = 6.28 rad/sec (f = 60 bpm).

Sample measurements of the axial velocity for profiles 2 (in the straight section) and 11 (in the conical section) are shown in figure 5.9 and 5.10 respectively. It is noticed that the flow rate varied from one profile to the other due to failure and replacement of certain parts of the artificial heart. For instance, profiles 1 to 10 were measured for a flow rate of 1.6 l/min (measured by a flowmeter), whereas profiles 11 for 2.8 l/min, 12 for 3.0 l/min, 14 for 1.8 l/min and 13, 15, 16 and 17 for 3.4 l/min. Table 5.3 provides the flow rates and their corresponding bulk velocities, Ub, of all profiles. In addition to the flow rate variation from profile to profile, there was much cycle to cycle variation within the same point of measurement of a single profile. Some examples are shown in figures 5.11 and 5.12. It can be noticed that this variation is more apparent in the cycles measured at points situated in

the conical section of the tube.

Azimuthal velocity measurements were also performed for profiles 2 and 17. Some representative cycles are shown in figure 5.13.

All the velocity measurements will be discussed in the next chapter.

Chapter 6

Analysis of the Results and Discussion

6.1 Estimates of Dimensionless Parameters

Due to the conical shape of the test section, its diameter increased from 13 mm at its entrance to 25 mm at its exit, with 19.5 mm being the mid-section diameter. As a consequence, a single value of the Womersley number cannot be defined, as in the case of cylindrical tubes. As a reference, one could use the corresponding local values, which were 17.1 (entrance), 32.9 (exit) and 25.0 (mid-section). Likewise, it is impossible to characterize the entire set of measurements by a single Reynolds number. First of all, because of the erratic operation of the pump, the flow rate varied among different measurements. Even if the flow rate were constant, the Reynolds number would change as a result of changes in cross-sectional area. Table 6.1 summarizes the definitions and values of various Reynolds numbers, based on local values of velocity and diameter at the positions of measured profiles.

6.2 General Flow Pattern

The first information about the flow pattern was obtained by means of flow visualization. Both close-up photography (plate 1) and video recording showed clearly the pulsatile nature of the flow.

Plate 1a, taken during early diastole (t=0.2 sec), shows clearly the relatively high speeds occurring during acceleration of the flow. The pathlines are relatively long and essentially straight all over the conical part of the tube, indicating near uniformity of the flow and laminarization during the acceleration phase. An estimate of the speed from these pathlines gave a typical velocity of 0.5 m/sec. Plate 1b, taken during late diastole (t=0.5 sec), shows clearly that the flow was decelerating. Curvature of the pathlines indicates the formation of vortical structures and possibly turbulence. Radial velocities appear to be substantial, especially near the walls. An estimate of the speed in the core gave typical values of around 0.35 m/sec. Plate 1c, also taken during late diastole just before the inlet valve closing (t=0.53 sec), shows a complex variation in the direction of the particle pathlines. A circulating region is very clear near the upper wall of the conical section and the pathlines are not uniform and have different lengths. All this is a clear indication of separated and recirculating regions near the inclined walls and higher level of turbulence. An estimate of an average absolute velocity in the centerline of the tube gave a value of 0.12 m/sec. The formation of backflow ("regurgitation") and the appearance of a recirculating region at the centerline and near the walls were observed during systole (t=0.86 sec) as shown in plate 1d. The pathlines are rel-

atively short and have different directions. An estimate of the velocity from these pathlines gave a typical value of 0.09 m/sec. These results show exactly the pulsatile nature of the flow in a conical tube. It is clear that, during the acceleration phase, the flow is laminarized but during the deceleration phase, the flow becomes unstable (possibly turbulent) near the wall.

6.3 Pressure Variation

The pressure variation at P1 and P2 is quite complex, as can be seen in figure 5.4. However, figure 5.5, showing simultaneous measurements of pressure at P2 and pusher plate/diaphragm displacement, may be used to clarify this complexity in the pressure variation. A likely explanation is as follows. At the beginning of the diastolic phase, the valve between the tube and the pump opens. The flow accelerates and the pressure drops as a result. Then, the flow decelerates and the pressure increases. Therefore, during diastolic phase, there is a systematic variation of pressure, corresponding to the hydrostatic pressure due to the water head, H, in the inflow reservoir. The main complexity in pressure variation occurs during the systolic phase, as shown in figure 5.5. There are two large peaks in each cycle, with a large negative peak between them. These peaks are attributed to pressure waves (water hammer) caused by the motion of the pusher plate and the associated opening and closing of the inlet valve. It is well known that, whenever a valve is closed in a pipe, a positive pressure wave is created upstream of the valve

and travels up the pipe at the speed of sound, c. For instance, taking the simplest case of water hammer, consider a similar flow in the pipe of figure 6.1 (Roberson and Crowe, 1985). Initially the valve at the end of the pipe is open (fig. 6.1a); consequently, an initial velocity, V, and initial pressure, P_o (H), exist in the pipe. At time t=0 the valve is instantaneously closed, thus creating a pressure wave that travels towards the inflow tank with the speed of sound, c. The water between the pressure wave and the upper end of the pipe will have the initial velocity, V, but the water between the wave and the valve will be at rest, as shown in figure 6.1b. After a time t=L/c, the pressure wave reaches the upper end of the pipe; thus, all the water in the pipe will be under a pressure $P_o + \Delta P$, while the pressure in the inflow tank at the entrance of the pipe is still only P_o. As a result of this pressure imbalance, the water in the pipe will flow back into the inflow tank with a velocity V. Therefore, a new pressure wave is formed that travels towards the valve; as shown in figure 6.1c. When the wave reaches the valve, all the water in the pipe flows towards the tank with a velocity V. However, such condition is only momentary, because the closed valve prevents any sustained flow. As shown in figure 6.1d, during the time $2L/c < t < 3L/c$, a rarefied pressure wave travels up to the tank. Then, when it reaches it, all the water in the pipe will have a pressure lower than that in the tank. Thus, the flow is established again in the entire pipe due to the pressure imbalance, as shown in figure 6.1f. This condition is exactly the same as the initial one (fig. 6.1a), and the process repeats itself within the systolic phase. The speed of sound, c, is equal to 1450 m/s for water at standard conditions. Estimates of the actual speed of the pressure waves in the present

section were not much lower than this value. The length, L, in the experiment is equal to around 320 mm. Therefore, the ratio, t = L/c, is equal to 0.000221 sec which is very small compared to the systolic time, t_s, which is 0.4 sec and lower than the temporal resolution of the pressure measurement system. Therefore, it may be concluded that reflected waves cannot be seen in the pressure plots.

The pressure measurements in the heart chamber at P3, shown in figure 5.6a, have a fairly complex pattern. There are two large maxima in each cycle. When the inlet valve closes (systole), the piston goes up to push the water out of the heart chamber to the compliance tank. Therefore, it exercises a force on the water, so the pressure increases to the first maximum and remains constant till most of the water is pumped. Then the pressure drops till the end of systole. Afterwards, the outlet valve closes, preventing the water from coming back to the heart chamber and the inflow valve opens at the beginning of diastole. The inflow head, H, forces the water inside the tube to fill the heart chamber as the piston goes down till it reaches the bottom position. At this moment, the pressure starts to built up due to the water accumulation in the heart chamber (figure 5.6a). When the heart becomes full of water the pressure reaches the second maximum. Then, it drops just before the closing of the inflow valve and a new cycle is started.

Pressure variations in the outflow tube at P4 (figure 5.6b) are also fairly complex. For most of the cycle the pressure is mainly hydrostatic due to the pressurized water head in the compliance tank. Similar to the case of the pressure variations at P1 and P2 in the inflow tube, there are major pressure fluctuations (two large peaks with a minimum peak between them) attributed to pressure waves caused

by closing the outflow valve. The only difference in these large fluctuations from those at the inflow tube is that the minimum peak between the large two peaks is not negative, because the water in the outflow tube is under higher pressure (pressurized closed tank) than that in the inflow tube.

6.4 Velocity Profiles

Different cycles of the instantaneous velocity measurements at one point situated at the centerline of the tube's straight section are shown in figure 6.3. Their averaged cycle, shown in figure 6.4, is produced by an averaging Fortran program written for the purpose. The program assumed a symmetric shape for the active part of the cycle (peak) and an equal timing of the peak occurrence from the beginning of diastole (to). The different cycles were superimposed by matching their lines of symmetry, i.e. the time of occurrence of the peak, and then averaged. It is clear that the resultan average cycle of the 8 cycles (figure 6.4) does not faithfully describe the individual cycles. In cases where there is much cycle to cycle variation at the same point of measurement, the peak velocity does not occur at the same timing from the beginning of diastole and the shape of the active part of the cycle (peak) is not symmetric, or that the above problem becomes more apparent. Due to all these observations, the averaging program was abandoned. Attempts to use other averaging techniques failed because the data were not acquired at equal intervals of time and presented some cuts in the cycles (missing

data, not validated by the PDA system). Other obstacles are due to the laser software limitations and to the lack of hard disk space and averaging software for pulsatile flows. It was therefore decided to choose among several cycles, for each point of measurement, a representative cycle which would be used for the analysis. This was achieved by overlaying several cycles, for each set of measurements, and selecting as the representative cycle one that best approximated the phase and amplitude characteristics of most other cycles. The choice of cycle might affect somewhat the magnitude of the velocity but not much the shape of its profile.

During a pulsatile flow cycle, 20 values, evenly spaced in time from the beginning of diastole to the end of systole, as shown in figure 5.2, were used to find the velocity profiles during the cycle.

17 radial profiles of the axial velocity were measured. Figures 6.5, 6.6, 6.7, 6.8, 6.9, 6.10 and 6.11 show the radial profiles 2, 11, 12, 13, 15, 16, and 17 respectively during different times of the cycle. U_b, in all figures, is the bulk velocity based on an average area, A_{ave}, equals 3.118 $\times 10^{-4}$ m^2. As examples, profile 2 (straight section) and profile 11 (conical section) will be considered in the analysis. For profile 2, it is noticed that the axial velocity profile is relatively flat and uniform during early diastole, t1, t2, t3, t4, t5 and t6. With the progression of diastole, t7 and t8, the flow along the region near the wall is seen to be reversed. Then, at t9 the reversed flow region is moved towards the center of the tube. This reversed flow is seen also at late diastole, t11 and t12, along almost all the tube radius, which indicates clearly the existence of separation and recirculation in the tube during the decelerating phase of the flow. During systole, t13, t15, t16, t17, t18

and t19, the flow is seen to be reversed, which indicates the formation of backflow ("regurgitation"). Profile 11 shows the same behavior. However, the reversed flow near the wall region was also observed at earlier times, t3 and t5, which is a clear indication of the effect of the inclined walls. Furthermore, during systole, the flow at t13 is reversed for all points along the profile, but, at t14, the flow near the centerline region is reversed back to positive direction, which is also an indication of a developing recirculation.

Sample measurements of the axial velocity along the centerline of the test section are shown in figure 6.12. The emerging downstream asymmetry of the "active" part of the velocity cycle during early diastole is a clear indication of separation in the conical tube.

Figure 6.13, representing the axial velocity near the wall region for profiles 2, 11, 12, 13, 15, 16 and 17, shows the occurrence of reverse flow during early diastole for most of the profiles conducted in the conical tube section, which is a clear indication of separation caused by the conical form.

As was mentioned earlier in section 5.5, it was noticed that there was much cycle to cycle variation at the same point of measurement of a single profile (figures 5.11 and 5.12). This variation is more apparent in the cycles measured at points situated on profiles in the conical section of the tube. It indicates that the core of the flow is shifting positions with time. This is associated with unstable recirculation and separation, a common occurrence in diffuser flows. A rough estimate of the cycle to cycle variation was conducted for one point of measurement situated near the wall region within the conical part of the tube (profile 11, Y =

8.75), where it is expected to be more severe. Several cycles at the same point of measurement were compared with the "typical" cycle used in the analysis and an average cycle. Relatively large variation of corresponding values at each of the chosen times was found, especially during deceleration, namely between t5 and t12. Another comparison was made by considering the maxima and the minima of each cycle, irrespective of the time at which they occurred. The rough estimate of this variation was found to be less than 15 % for both the maximum and the minimum values.

Figure 6.14 shows the radial profiles 2, 11, 12, 15 and 17 of the axial velocity at different times, t3, t5, t10,t13 and t18. It is clear that separation regions near the wall appeared at early diastole (t3 and t5) for profiles in the conical section. All the profiles seem to have the same shape away from the wall region. With the progression of diastole, at t10, the velocity profiles become disturbed and non-uniform, due to the deceleration of the flow and the higher viscous effects near the wall. At t13, early systole, all the profiles show the formation of backflow ("regurgitation") and seem to have similar patterns.

6.5 Estimates of Turbulence

The presence of turbulence was first detected by inspection of the visualized flow. Then, it was confirmed by inspection of the velocity time histories. For example, typical cycles of the axial velocity at different radial positions 2, in the

cylindrical tube just upstream of the conical section, show clearly the presence of relatively high frequency fluctuations. Such fluctuations were visible during most of the diastole, especially during deceleration, and can be interpreted as small-scale turbulence. In contrast, during systole, velocity fluctuations were, in general, relatively slow and qualitatively repeatable from one cycle to another, thus not qualifying as turbulence. For these data, $\alpha = 17.2$ and $R_\delta = 1,155$ (Table 6.1). It may be relevant that fully developed, oscillatory flow having comparable values of α and R_δ was also found to be turbulent during the entire cycle (Ohmi et al., 1982). The intensity of turbulence appears to increase from the tube's centre towards the wall, with some excursions to zero speed appearing in the measurements closest to the wall. A typical set of velocity measurements at the mid-section of the conical tube is shown in figure 5.10, corresponding to the local values $\alpha = 25.8$ and $R_\delta = 613$. As in the case of the cylindrical section, high frequency fluctuations, which we interpret as turbulence, were present in most of the diastole, but they appear to be lesser in amplitude, compared to the former case. As previously, the amplitude of fluctuations increases from the centre towards the wall.

Ideally, the velocity fluctuations at a certain time in the cycle could be calculated by subtracting the ensemble averaged velocity at that time from the corresponding instantaneous velocity. However, as mentioned earlier, the ensemble averages were contaminated by the cycle-to-cycle variations. As a result, the following method was used to roughly estimate the velocity fluctuations. For each point of measurement, a representative cycle was selected and an envelope that encloses the fluctuating velocity signal was hand-drawn (figure 6.15). The running

height of the envelope which represents the velocity fluctuation from peak to peak, u_{pp}, was measured at different times during the cycle. The obtained u_{pp} may be assumed to correspond roughly to 2.5 u', where u' is the root-mean-square of the velocity fluctuations. However, the values presented in figure 6.16 are those of $u_{pp}/2$. It is to be noted that the above method implicitly assumes that at each time in the cycle the average velocity is at the center of the envelope at that specific time. Figure 6.15 shows the envelope for profile 11, near the wall (a) and at the centerline (b).

The fluctuating velocity in the streamwise direction was estimated from u_{pp} for profiles 2, 11 and 17, as shown in figure 6.16. The peak of the turbulence for profile 2 seems to occur at an earlier time than that for profiles 11 and 17. It occurred (for profile 2) between 0.1 and 0.3 sec, which correspond to t2 and t6 respectively, while it occurred between 0.2 sec (t4) and 0.4 sec (t8) for profiles 11 and 17. In conclusion, the flow in the conical section is more turbulent during the decelerating phase. It is also evident that the turbulence near the wall region is stronger than the core. Turbulence was visible mainly during diastole, and the flow appeared to relaminarize during the rest of the cycle. Some turbulence is also noticed during the systole between 0.6 (t12) and 0.7 sec (t14), which is caused by the backflow. The present results can be compared to measurements on transition to turbulence in oscillatory pipe flow, conducted by Eckmann and Grotberg (1991) for wide ranges of α and R_δ ($9 < \alpha < 33$ and $500 < R_\delta < 1310$). They found that the core flows remained laminar while the Stokes layer became unstable during the deceleration phase. This turbulence was most intense near the wall, defined

as an annular region of variable thickness. Our results differ from theirs since we find the turbulence generated near the wall gets dispersed across the cross-section. In other words, turbulence was observed also near the core region, however, it was weaker than that near the wall.

6.6 Azimuthal Velocity Measurements

The azimuthal velocity measurements revealed also a wider range of velocity and velocity fluctuations in the active part of the cycle, near the wall region for both the straight (a) and the conical (b) section of the tube, as shown in figure 5.13. An estimate of the cross-sectional average of the peak azimuthal velocity amplitude during diastole for profile 2 was found to be about 0.012 m/sec, which is 6.2% of the cross-sectional average of the peak velocity amplitude, $\hat{U}$. Therefore, it is very small and should not affect very much the main stream. The origin of swirl is not clear and could be attributed to some asymmetry in the entrance geometry.

Chapter 7

Conclusions and Recommendations for Future Work

In summary, the main conclusions of the present thesis are as follows:

- The first objective was attained by the creation of a reliable facility for experimental research on pulsatile flow.
- Flow visualization in the conical tube provided qualitative information for such types of flow.
- The pressure variation in the tube is fairly complex. The large variation in the pressure cycle is mainly attributed to pressure waves caused by the closing of the valve.
- Due to the index of refraction mismatch and the inconsistent pump performance, velocity measurements were restricted mainly to the axial velocity component.

- Reverse flow was very clear in both the conical and the straight sections of the tube. However, in the conical section, the flow shows more unsteady and complex variation during the cycle. It was found that the reverse flow near the wall region occurs earlier in the diastolic phase as compared to that for the straight section.

- The emerging downstream asymmetry in the velocity cycle during diastole is a clear indication of separation and recirculation in the conical part of the tube.

- Cycle to cycle variations at the same point of measurement were observed for both conical and straight section of the tube. However, they were larger in the conical part of the tube.

- In the conical section, turbulence occurred mostly during the decelerating phase of the cycle and was followed by near laminarization for the remainder of the cycle. Instability did not penetrate the core of the flow, but it was more significant near the wall region.

- Azimuthal velocity measurements also revealed that the above instability occurred in both the straight and the conical sections of the tube. However, stronger instability was observed in the conical section of the tube, especially near the wall region.

In addition to the work presented here, the present research has direct extensions, which can be summarized in the following points. First, for complete information about the flow through the tube, two more profiles between profile 2

and profile 11 must be analyzed, e.g. profiles 5 and 8. Measurements for both profiles have been collected and stored on magnetic tapes. The second step is to analyse the measurements of profiles 1 and 17 for different values of the Womersley number, α, to fully understand the influence of this parameter on the flow pattern. In addition, profile 1 was conducted for different inflow heads, which, if analyzed, would reveal the effect of the inflow pressure on the flow. Finally, more constructive comparison of the present results with other people's work will be done in the near future.

References

AKUTSU, T. 1988 Artificial Heart 2: Part II, ventricular assist device, research and development. *Proceedings of the 2nd International Symposium on Artificial Heart and Assist Device, Springer-Verlag*, Tokyo, Japan.

BUDWIG, R.S. 1985 Unsteady Heat Transfer Experiments in Laminar Oscillatory Flow in Straight and Conical Tubes, Ph.D. Thesis, *The Johns Hopkins University*, Baltimore, Maryland.

BUSS, G.Y. 1983 Transition to turbulence in a model of the human superficial femoral artery, in *Blood Flow, Theory and Practice*, (D.E.M. Taylor et al., editors), *Academic Press*, London, 7-37.

CARO, C.G., PEDLEY, T.J., SCHROTER, S.C. AND SEED, W.A. 1978 The Mechanics of the Circulation, *Oxford Univ. Press*, Oxford, 527.

DANTEC, Instruction Manuals.

DINNAR, U. 1981 Cardiovascular Fluid Dynamics, *CRC Press Inc.*

DOEBELIN, E.O. 1990 Measurement Systems, Application and Design *Fourth edition, McGraw-Hill, Inc.*, New York.

DRAIN, L.E. 1980 The Laser-Doppler Technique. *John Wiley and Sons*, New York.

DURRANI, T.S. AND GREATED, C.A. 1977 Laser Systems in Flow Measurements. *Plenum Press*, New York.

DURST, F., MELLING, A. AND WHITELAW, J.H. 1981 Principles and Practice of Laser-Doppler Anemometry. *Second edition, Academic Press*, London.

DYBBS, A. AND EDWARDS, R.V. 1984 An index matched flow system for measurements of flow in complex geometries. *Proceeding of Second International Symposium on Applications of Laser Anemometry to Fluid Mechanics, ed. D.F.G. Durao.*, 171-184.

EDWARDS, R.V. AND DYBBS, A. 1984 Refractive index matching for velocity measurement in complex geometries. *TSI Quarterly.* **10(4)**, 3-11.

FISHLER, L.S. AND BRODKEY, R.S. 1990 Transition, turbulence and oscillating flow in a pipe a visual study. *The Twelfth Symposium on Turbulence: University of Missouri-Rolla, Columbus*, A2.1-A2.13.

FUNG, Y.C. 1981 Biomechanics: Mechanical Properties of Living Tissues. *Springer-Verlag*, New York.

FUNG, Y.C. 1984 Biodynamics: Hemodynamics, Blood Circulation. *Springer-Verlag*, New York.

GERRARD, J.H. 1971 An experimental investigation of pulsating turbulent water flow in a tube. *J. Fluid Mech.* **46**, 43-64.

GOLDSMITH, H.L. AND SKALAK, R. 1975 Hemodynamics, in *The Annual Review of Fluid Mechanics*, (M.V. Dyke et al., editors). **7**, 213-247.

GRACE, S.F. 1928 Oscillatory motion of a viscous liquid in along straight tube. *Phil.Mag.* **5**, 933-939.

GRASSMANN, P. AND TUMA, M. 1979 Critical Reynolds numbers for oscillating and pulsating tube flow. *Würme-und Stoffübertragung.* **12**, 203-209.

GROTBERG, J.B. AND ECKMANN, D.M. 1991 Experiments on transition to turbulence in oscillatory pipe flow. *J. Fluid Mech.* **222**, 329-350.

GUYTON, A.C. 1974 Function of the Human Body. *Fourth edition, W.B. Saunders Company*, London.

HALL, P. 1974 Unsteady viscous flow in a pipe of slowly varying cross-section. *J. Fluid Mech.* **64**, 209-226.

HINO, M., SAWANOTO, M. AND TAKASU, S. 1976 Experiments on transition to turbulence in an oscillatory pipe flow. *J. Fluid Mech.* **75**, 193-207.

LINFORD, R.G. AND RYAN, N.W. 1965 Pulsatile flow in rigid tubes. *J. Appl. Physiol.* **20**, 1078-1082.

MCDONALD, D. 1974 Blood Flow in Arteries. *Williams and Wilkins*, Baltimore, Maryland.

MERKLI, P. AND THOMANN, H. 1975 Transition to turbulence in oscillating pipe flow. *J. Fluid Mech.* **68**, 567-575.

MUSSIVAND, T.V. 1988 Artificial Heart Fluid Dynamics. Ph.D. Thesis, Akron University, Akron.

MUSSIVAND, T.V., ET AL. 1988 Artificial heart instrumentation for fluid dynamic analysis. *Proceedings of the International Conference and Exhibit, Houston, Texas*, **88-14423**, 267-276.

NOURI, J.M., WHITELAW, J.H. AND YIANNESKIS, M. 1986 A refractive-index matching for solid/liquid flows in *Laser Anemometry in Fluid Mechanics-III*, Se-

lected Papers from the Third International Symposium on Applications of Laser Anemometry to Fluid Mechanics, (R.J. Adrian et al., editors). Lisbon, Portugal, 335-346.

OHMI, M., IGUCHI, M. AND URAHATA, I. 1982 Flow patterns and frictional losses in an oscillating pipe flow. *Bull. Japan. Soc. Mech. Eng.* **25**, 536-543.

PARATO, G., LEUTHEUSSER, H.J. AND LETELIER, M.F. 1986 Characteristics of oscillatory laminar flow in short pipes. *Third Forum on Unsteady Flow. Amer. Soc. Mech. Eng. (ASME).* **39**, 7-9.

RAYLEIGH, L. 1884 On the circulation of air observed in Kundt's tubes, and on some allied acoustical problems. *Phil. Trans. Roy. Soc. Lond.* **175**, 1-21.

RICHARDSON, E.G. AND TYLER, E. 1929 The transverse velocity gradient near the mouths of pipes in which an alternating or continuous flow of air is established. *Proc. Phys. soc.* **42**, 1-15.

ROBERSON, J.A. AND CROWE, C.T. 1985 Engineering Fluid Mechanics. *Third edition, Houghton Mifflin Company.* Boston.

RUDINGER, G. 1966 Review of current mathematical methods for the analysis of blood flow. *Biomedical Fluid Mechanics Symposium, Amer. Soc. Mech. Eng., Fluids Engineering Division*, 1-33.

SCHLICHTING, H. 1932 Berechnung ebener periodischer Grenzchichtstromungen. *Phys. Z.* **33**, 327.

SERGEEV, S.J. 1966 Fluid oscillations in pipes at moderate Reynolds numbers. *Fluid Dyn.* **1**, 121-122.

SZYMANSKI, P.V. 1930 Sur l'écoulement non-permanent du fluide visqueux dans

le tuyau. *Proc. 3rd Int. Congr. Appl. Mech.* 1, 249-254.

WOMERSLEY, J.R. 1955 Method for the calculation of velocity, rate of flow and viscous drag in arteries when the pressure gradient is known. *J. Physiol.* **127**, 553-563.

YOGANATHAN, A.P., WOO, Y.R. AND WILLIAMS F.P. 1983 In-vitro fluid dynamic characteristics of the abiomed trileaflet heart prosthesis. *J. Biomech. Eng.* **105**, 338-345.

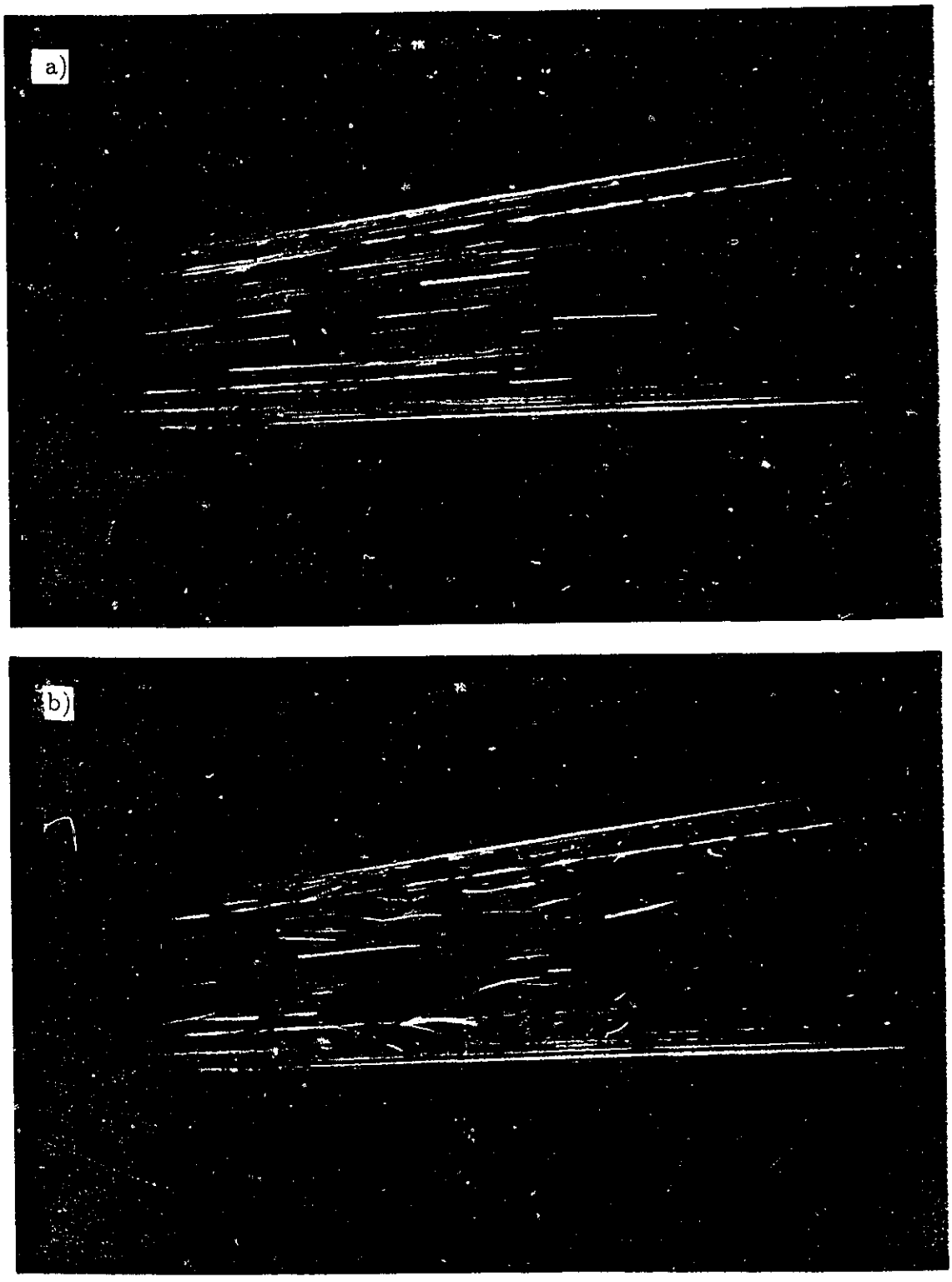

Plate 1: Photographs of the Flow Inside the Tube during one Cycle.

a) Early Diastole, b) and c) Late Diastole, d) Systole.

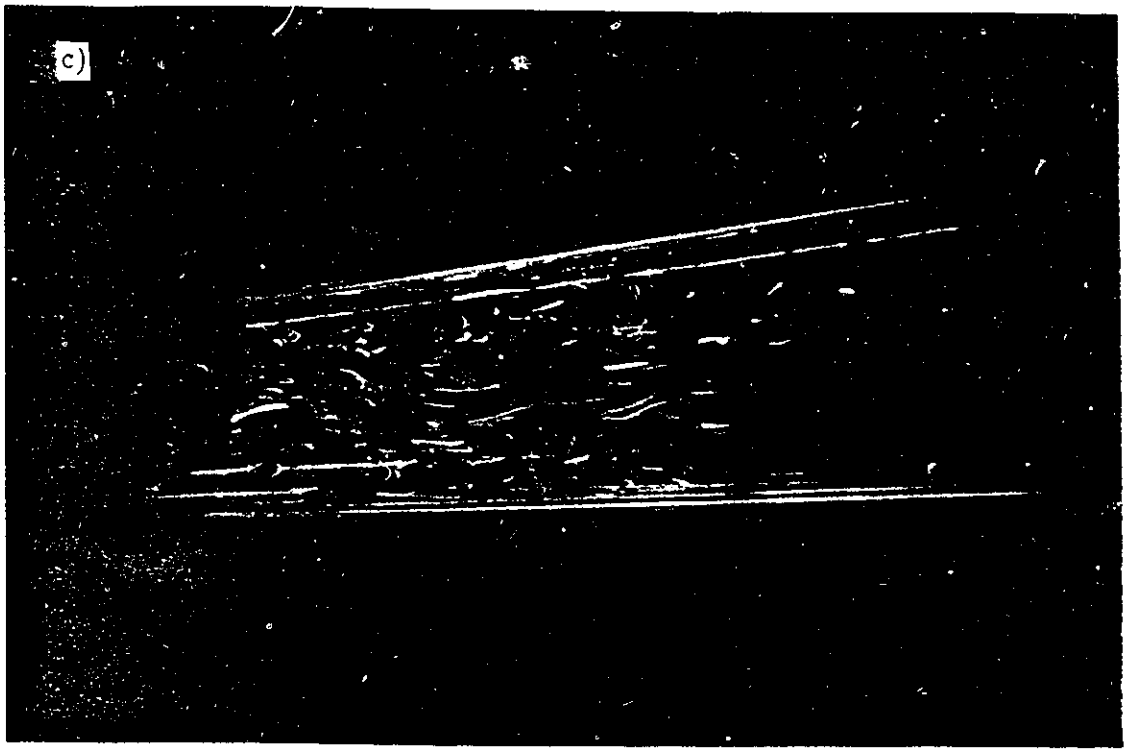

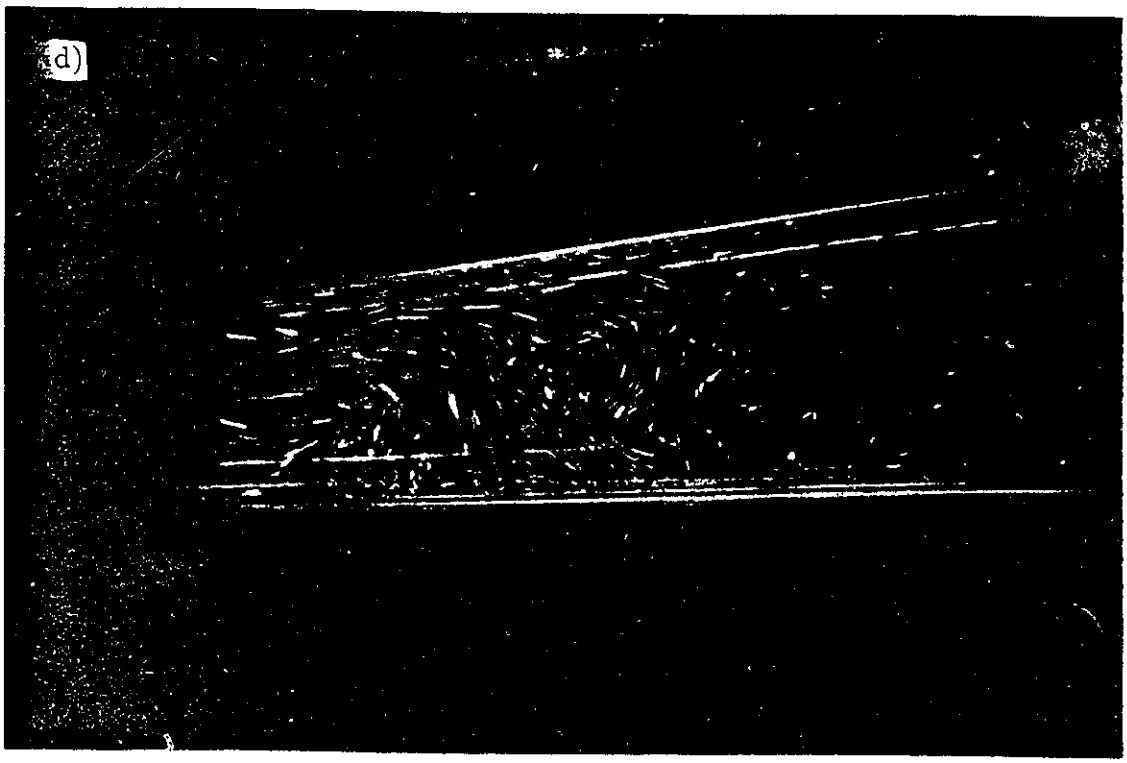

Plate1...Cont'd.

Property	Normal Condition	
Blood volume		4000—5000 cc
Viscosity	Whole blood:	3.5 centipoise
	Plasma:	1.8—2.5 cp
Blood specific gravity	Male:	1.057
	Female:	1.052
Blood hematocrit	Male:	0.47
	Female:	0.42
Blood PH		7.35—7.40
Blood pressure	Systolic:	120 mmHg
	Diastolic:	80 mmHg
Oxygen content (arterial)		23 cc O_2/100 cc blood
Cardiac output		4500—5000 cc/min
Heart rate		70—75 beats/min

Table 4.1: Physical Properties of Human Blood

Fluid	Physical Data n_d	Physical Data Viscosity	Test Section Material	Remarks
Mixture of: Dow Corning 550 73% by weight Union Carbide 27% by weight	1.4905	1.88×10^{-4} m^2/s	Plexiglas	High Kinematic Viscosity, ν
Mixture of: Dow Corning 556 48% by weight Dow Corning 550 51.5% by weight	1.474	4.33×10^{-5} m^2/s	Pyrex Glass	High ν
Mixture of: Sohio's Mineral Seal Oil 58% by volume Sohio's MDI-57 42% by volume	1.464	6.76×10^{-6} m^2/s	Optical Glass	High ν $nd \ll n_{Plexiglas}$
Di-butylphthalate	1.492		Plexiglas	Very Toxic Harmful Vapor
Mixture of: Tetraline (Tetrahydronaphthalene) + Turpentine 40% by weight	1.49	2×10^{-3} kg/m.s	Plexiglas	Very Toxic Harmful Vapor
Mixture of: O-Xylene Varsol 44% by weight	1.474		Pyrex	Very Toxic Harmful Vapor
Silocone High Temperature Oil	1.495	0.18	Plexiglas kg/m.s	High ν
Mixture of: Potassium Thiocyanate 64% by weight (in water)	1.475	1.761×10^{-6} m^2/s		Very Toxic

Table 4.2: Matched Index Materials

Material	Specifications		
	d (μm)	n	ρ (Kg/m^3)
Polystyrene Latex Particles Model 10085A	1 nominal	0.59	10.5
Silocon Carbide Model 10081	1.5	2.65 nominal	32
Metallic-Coated Particles Model 10087	9		26
Plastic Paint	$\leq$10		
Aluminium Powder	$\leq$10		
Fluorescent Polystyrene Latex	0.5 - 50		

Note: n is the index of refraction.

Table 4.3: Seeding Particles for Water

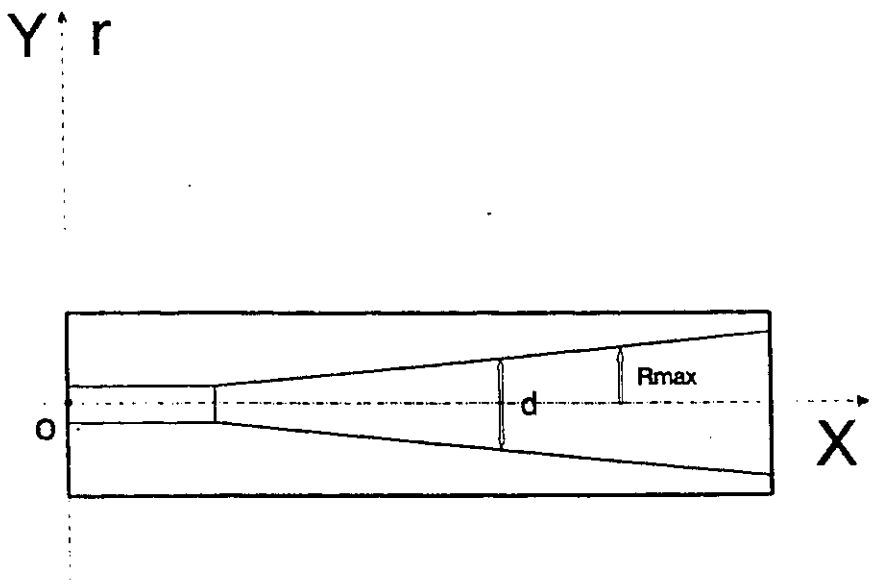

Pressure measurements		
X (mm)	5	111
d (mm)	13	24.5
Y (mm)	-6.5	-12.75

Table 5.1: Positions of Pressure Measurements in the Tube.

Velocity measurements																	
Radial profile No	1	2	3	4	5	6	7	8	9	10	11	12	13	14	15	16	17
X (mm)	5	21	31	42	45	48	51	54	57	60	71	85	88	91	94	97	101
d (mm)	13	13	14	15.5	16	16.5	17	17.5	18	18.5	19.5	22	22.5	23	23.5	24	24.5
Y (mm)															11.5	11.5	11.5
												10.5	10.75		11	11	11
											9.5	10	10	10	10	10	10
							8.5		8.5	9	8.75	9	9	9	9	9	9
					7.5	8	8	8	8	8	8	8	8	8	8	8	8
			6.5	7	7	7	7	7	7	7	7	7	7	7	7	7	7
	6	6	6	6	6	6	6	6	6	6	6	6	6	6	6	6	6
	5	5	5	5	5	5	5	5	5	5	5	5	5	5	5	5	5
	4	4	4	4	4	4	4	4	4	4	4	4	4	4	4	4	4
	3	3	3	3	3	3	3	3	3	3	3	3	3	3	3	3	3
	2	2	2	2	2	2	2	2	2	2	2	2	2	2	2	2	2
	1	1	1	1	1	1	1	1	1	1	1	1	1	1	1	1	1
	0	0	0	0	0	0	0	0	0	0	0	0	0	0	0	0	0
	-1	-3	-1	-2	-2	-2	-1	-2	-2	-2	-1	-1	-1	-1	-1	-1	-1
	-2	-4	-3	-4			-3				-3	-3	-3	-3	-3	-3	-3
	-3	-5	-5	-6.5			-5							-5			
	-4	-6	-6	-7.5			-7							-7			
	-5						-8.5							-9			
	-6													-10			

Table 5.2: Positions of Velocity Measurements in the Tube.

Profile #	Flow rate (lit/min)	Bulk Velocity (m/sec)
1	1.6	0.086
2	1.6	0.086
3	1.6	0.086
4	1.6	0.086
5	1.6	0.086
6	1.6	0.086
7	1.6	0.086
8	1.6	0.086
9	1.6	0.086
10	1.6	0.086
11	2.8	0.15
12	3.0	0.16
13	3.4	0.182
14	1.8	0.096
15	3.4	0.182
16	3.4	0.182
17	3.4	0.182

Note: The bulk velocity is based on an average area, A_{ave}, equals $3.118 \times 10^{-4}\ m^2$.

Table 5.3: Profiles Flow Rates and Bulk Velocities.

Profile #	d (mm)	U_b (m/sec)	$\hat{U}$ (m/sec)	R_{ave}	R ($\times 10^4$)	R_δ	α
2	13	0.086	1.94	1246	2.8	1155	17.2
11	19.5	0.150	1.03	3260	2.2	613	25.8
12	22	0.160	0.97	3924	2.4	577	29.1
15	23.5	0.182	0.92	4768	2.4	548	31.1
17	24.5	0.182	0.86	4971	2.3	512	32.4

$\hat{U}$ = **Cross-sectional average of the peak velocity amplitude.**
$R_{ave} = \frac{U_b d}{\nu}$
$R = \frac{\hat{U} d}{\nu}$
$R_\delta = \frac{\hat{U} \delta}{\nu}$
$\alpha = r(\frac{\omega}{\nu})^{\frac{1}{2}}$
$\delta = (\frac{2\nu}{\omega})^{\frac{1}{2}} = 5.34 \times 10^{-4} m$
$\nu = 9.0 \times 10^{-7} m^2/sec$
$\omega = 60 cpm = 2\pi rad/sec$

Table 6.1: Estimates of Dimensionless Parameters.

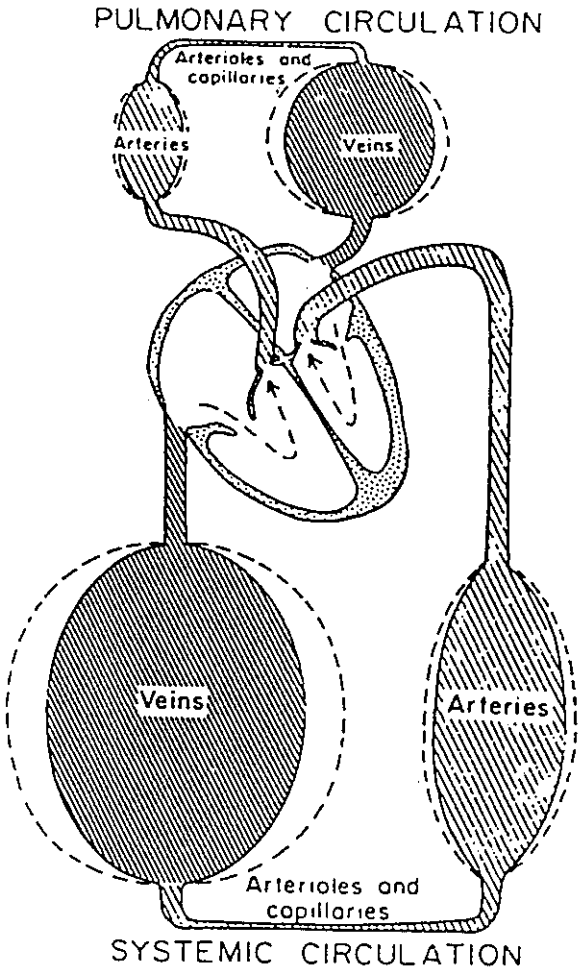

Figure 1.1: Schematic Representation of the Circulation, Showing the Two Sides of the Heart and the Pulmonary and Systemic Circulations (Arthur, 1974).

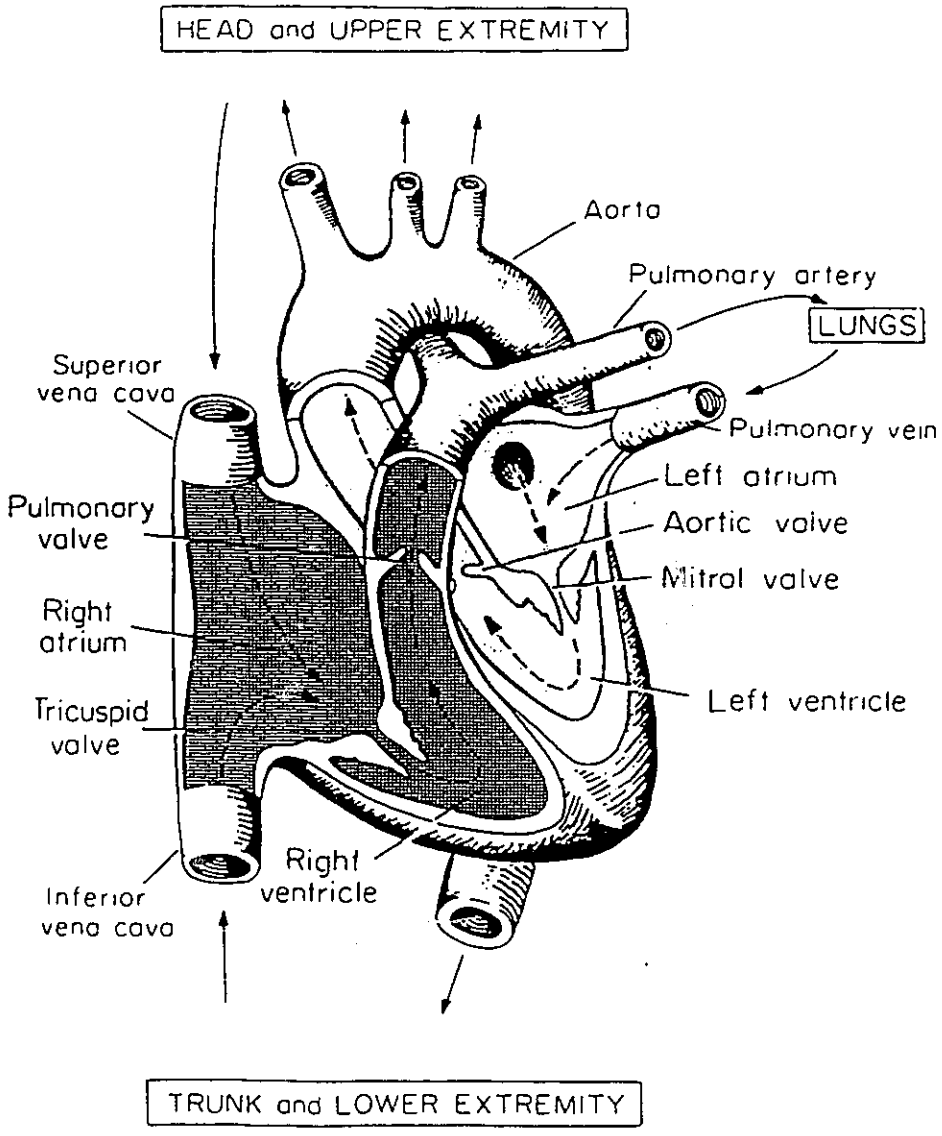

Figure 1.2: The Functional Parts of the Heart (Arthur, 1974).

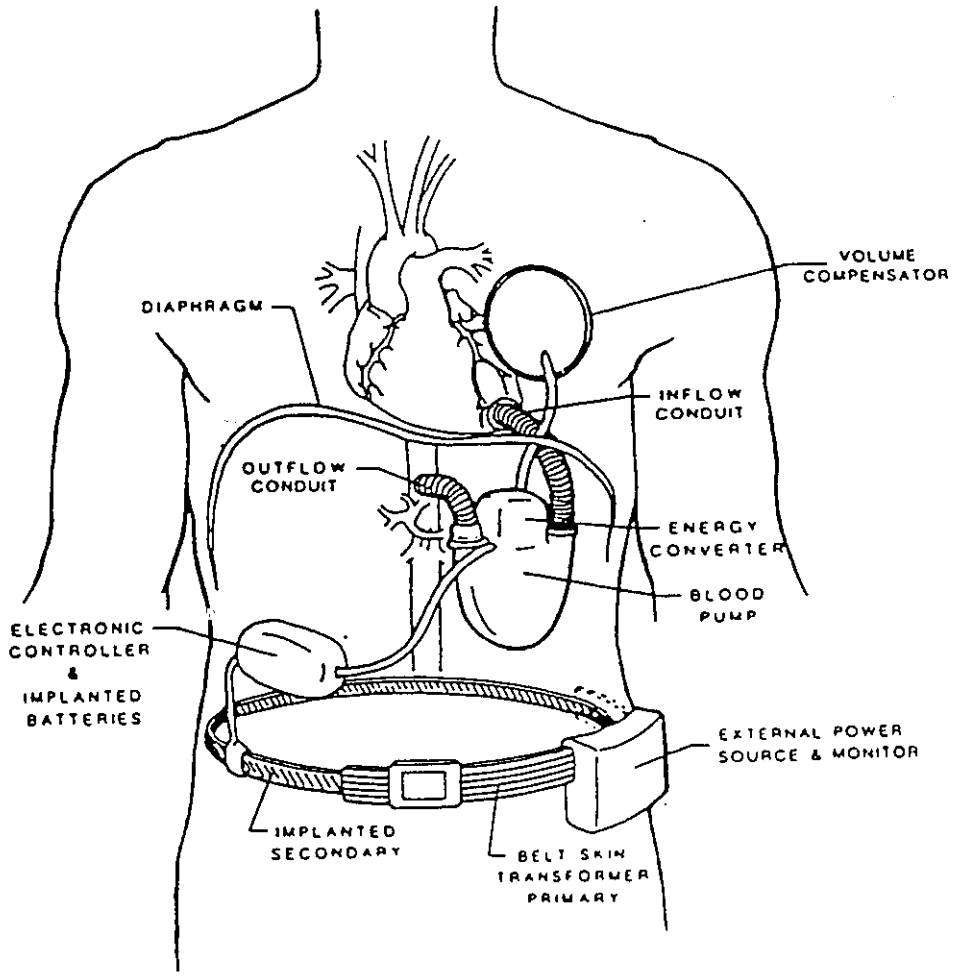

Figure 1.3: Schematic Representation of the Use of Inflow and Outflow Conduits (Cannulae) with an Artificial Heart Pump (Akutsu, 1988).

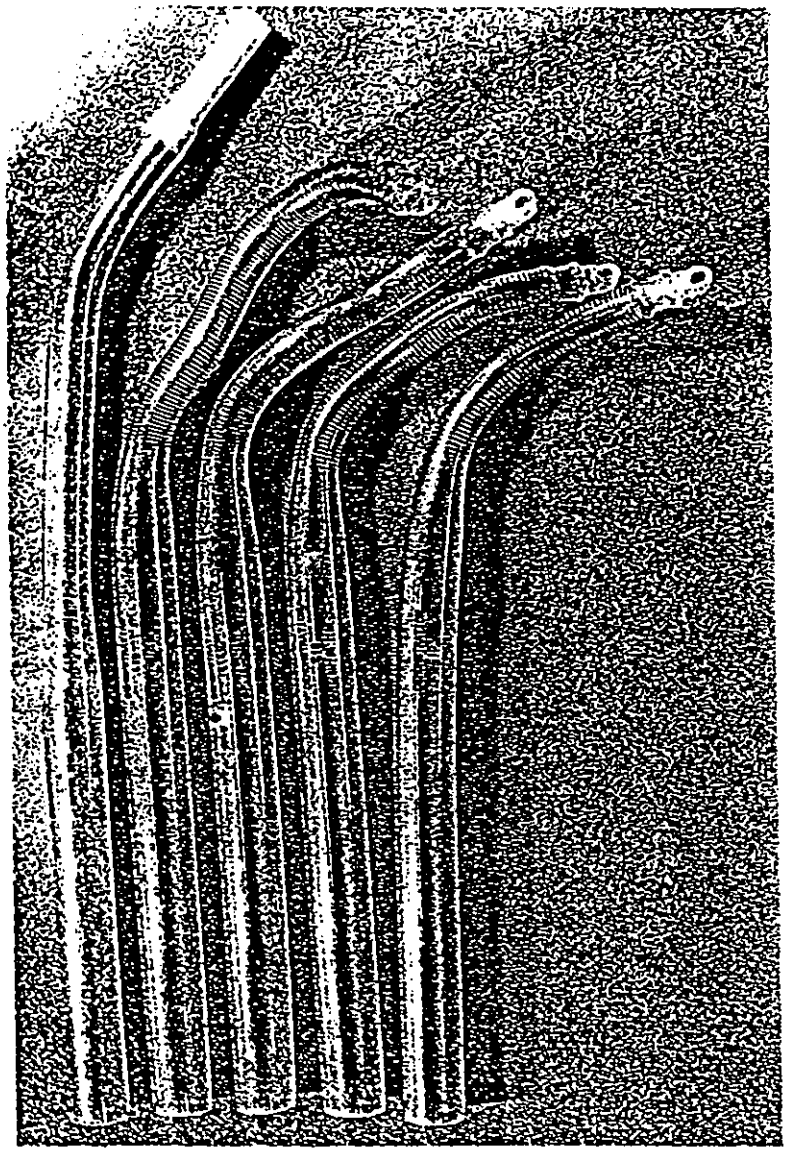

Figure 1.4: Different Types of Surgical Cannulae (Akutsu, 1988).

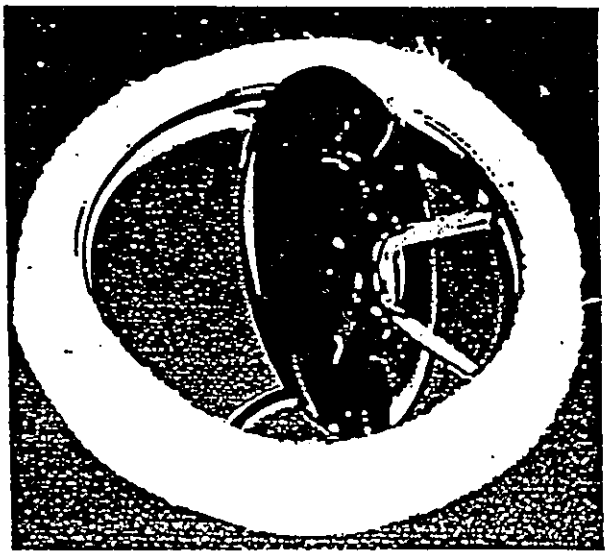

Figure 1.5: Bjork-Shilley Monostrut Prosthesis (Yoganathan et al., 1983).

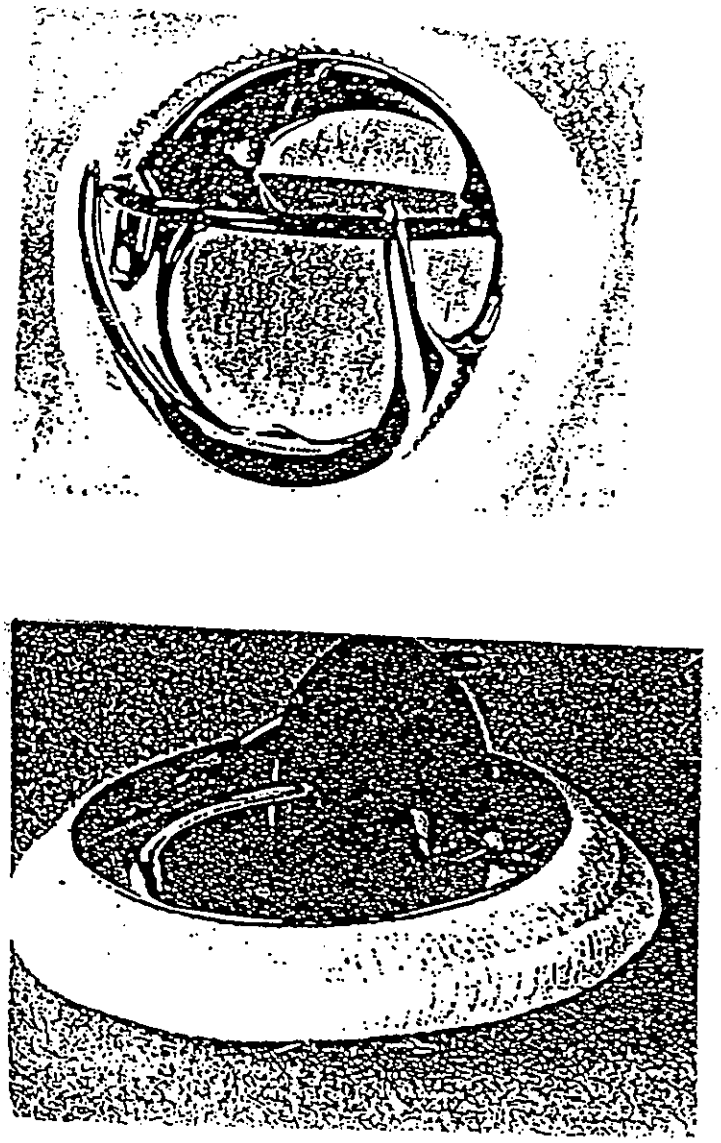

Figure 1.6: Lillehei-Kaster Mitral (left) and Aortic (right) Valves (Yoganathan et al., 1983).

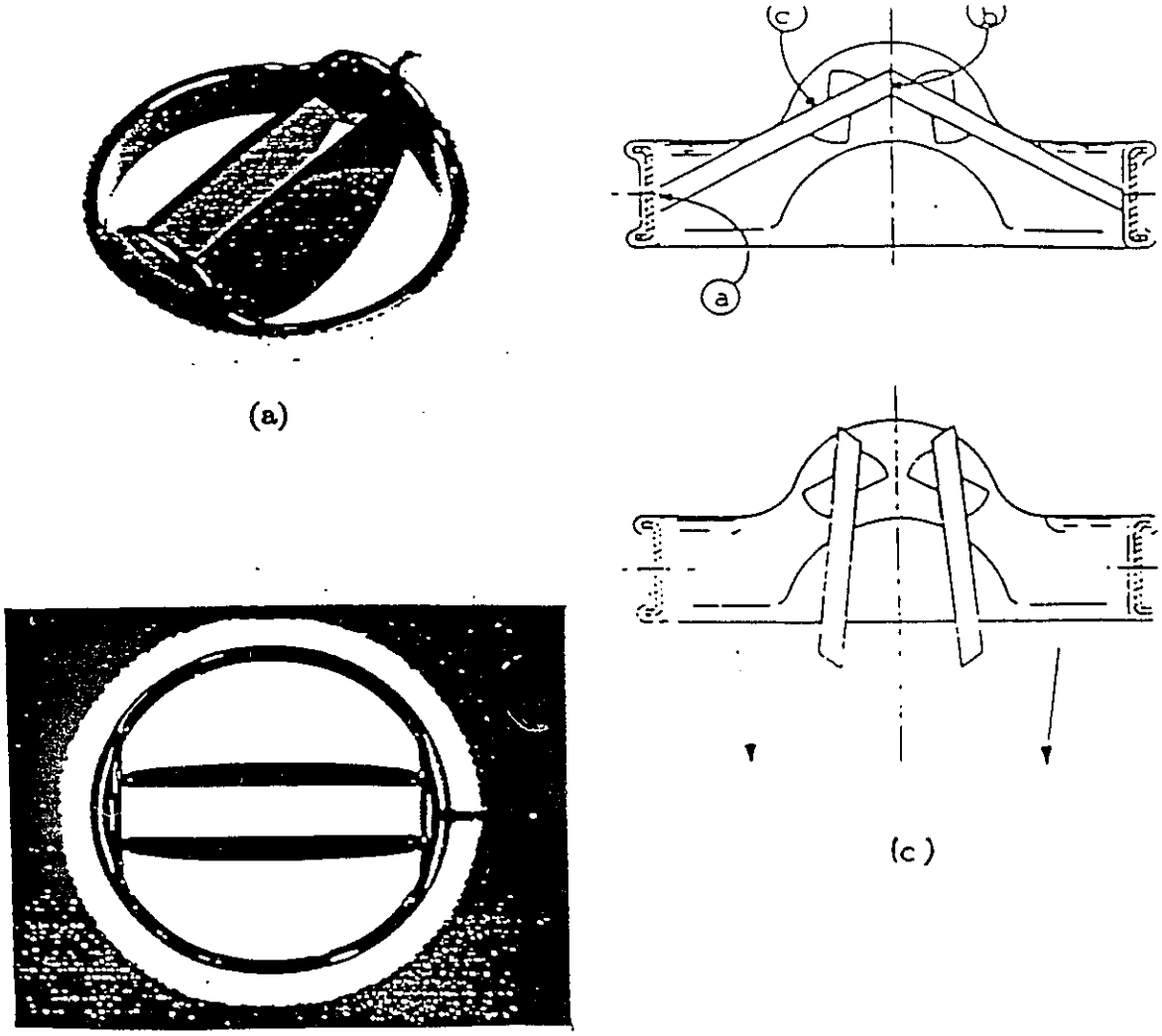

Figure 1.7: St-Jude Medical Prosthesis in Open Position (Yoganathan et al., 1983).

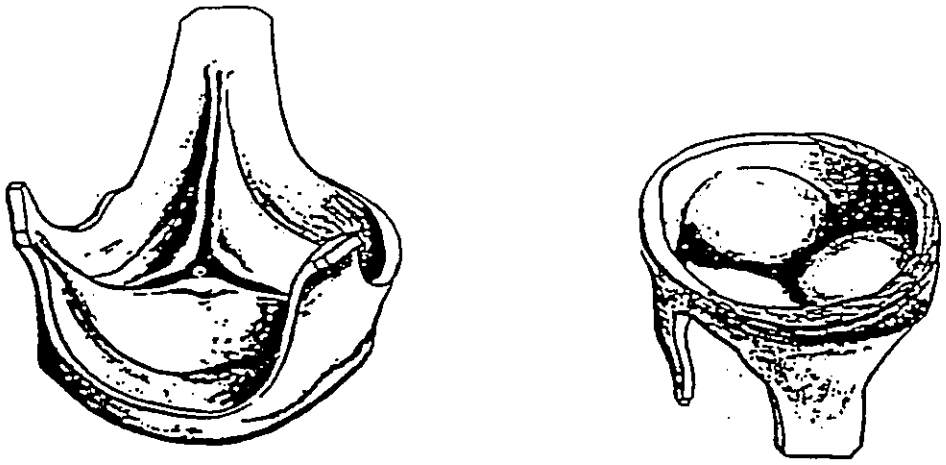

Figure 1.8: Homograft Aortic Valve (Yoganathan et al., 1983).

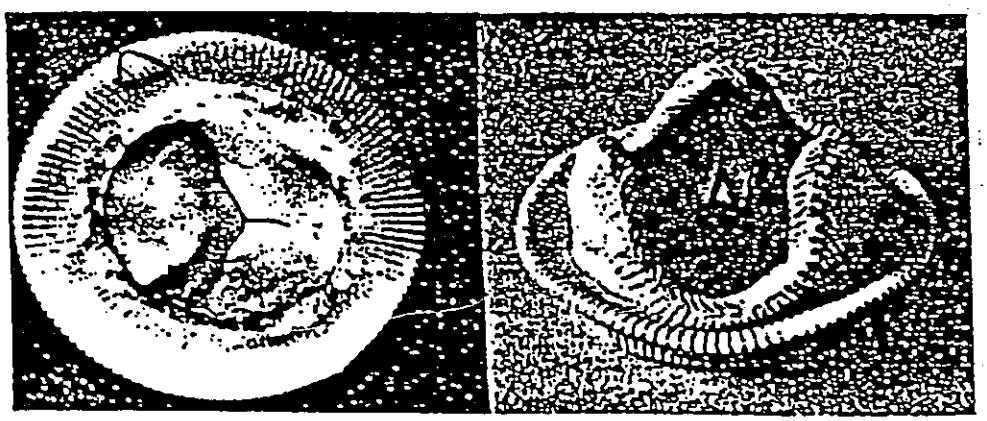

Figure 1.9: Hancock Porcine Xenograft Valve Inflow (left) and Outflow (right) (Yoganathan et al., 1983).

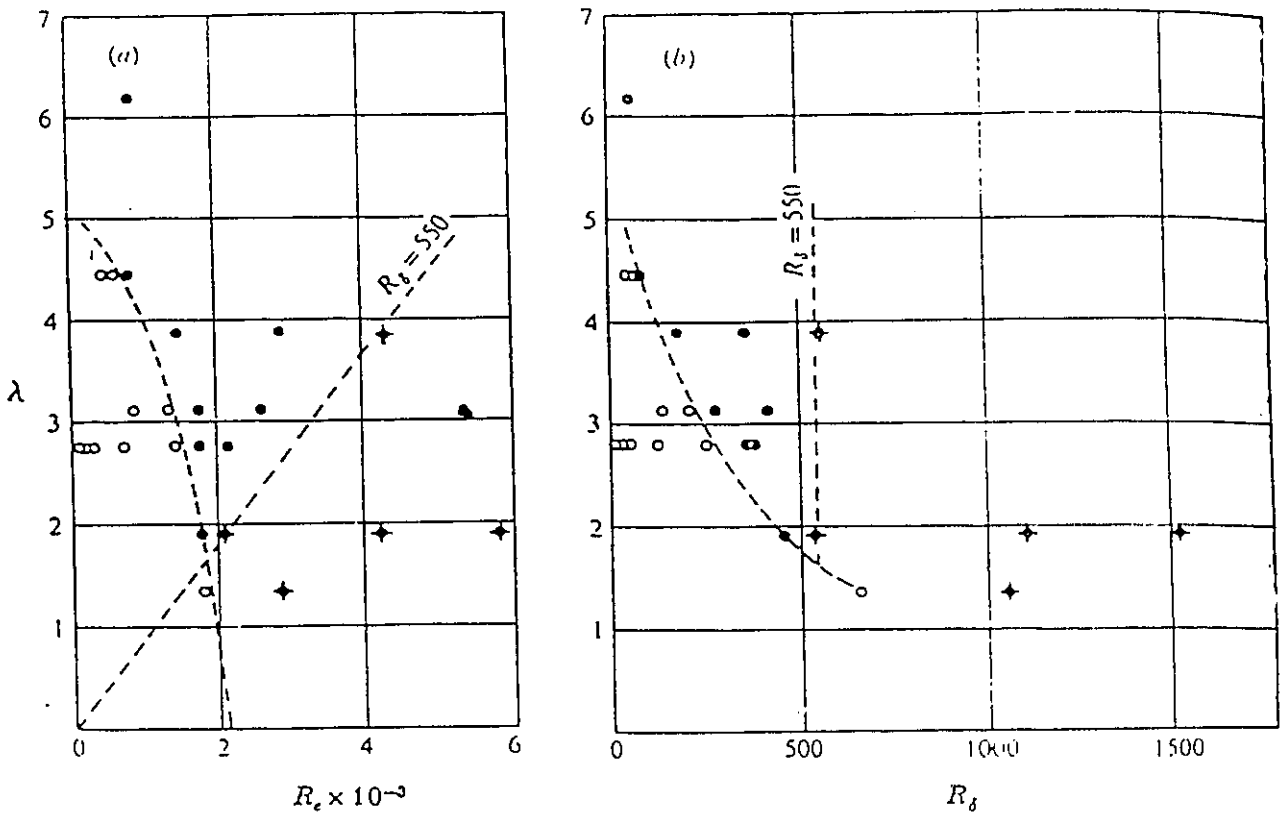

Figure 2.1: Stability Diagrams: (a) R_e vs. λ and (b) R_δ vs. λ. ○, Laminar or Distorted Laminar Flows; •, Turbulent Flows of Type (c), i.e. Weakly Turbulent; ✦, Turbulent Flow of Type (d), i.e. Conditionally Turbulent (Hino et al., 1976).

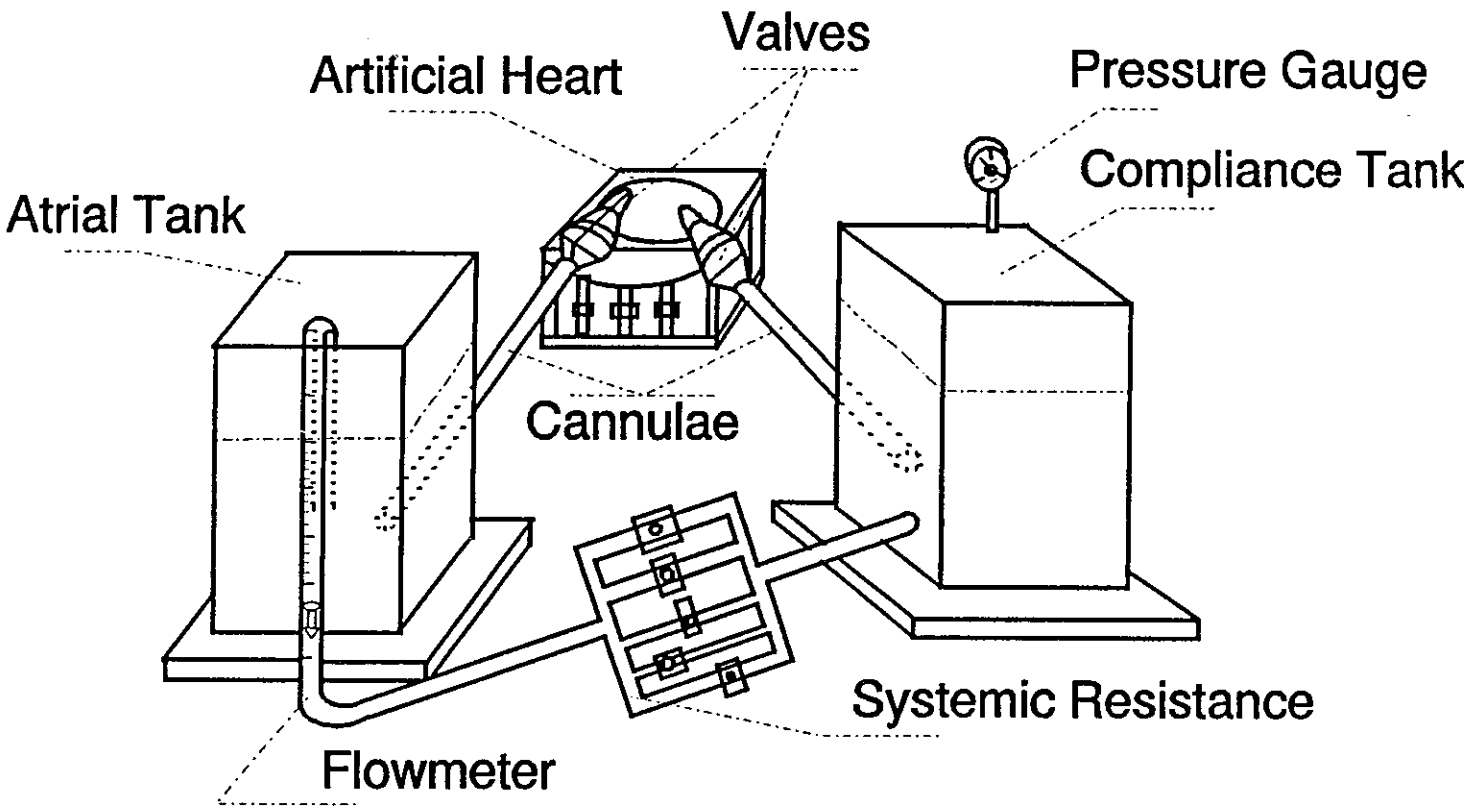

Figure 3.1: Schematic Diagram of the Mock Circulatory Loop.

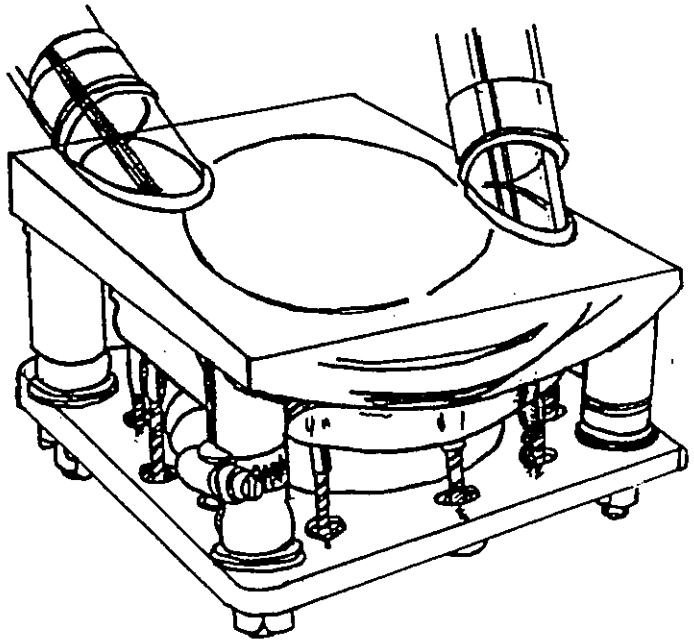

Figure 3.2: Duplicate of the Pneumatic Pusher Plate Blood Pump.

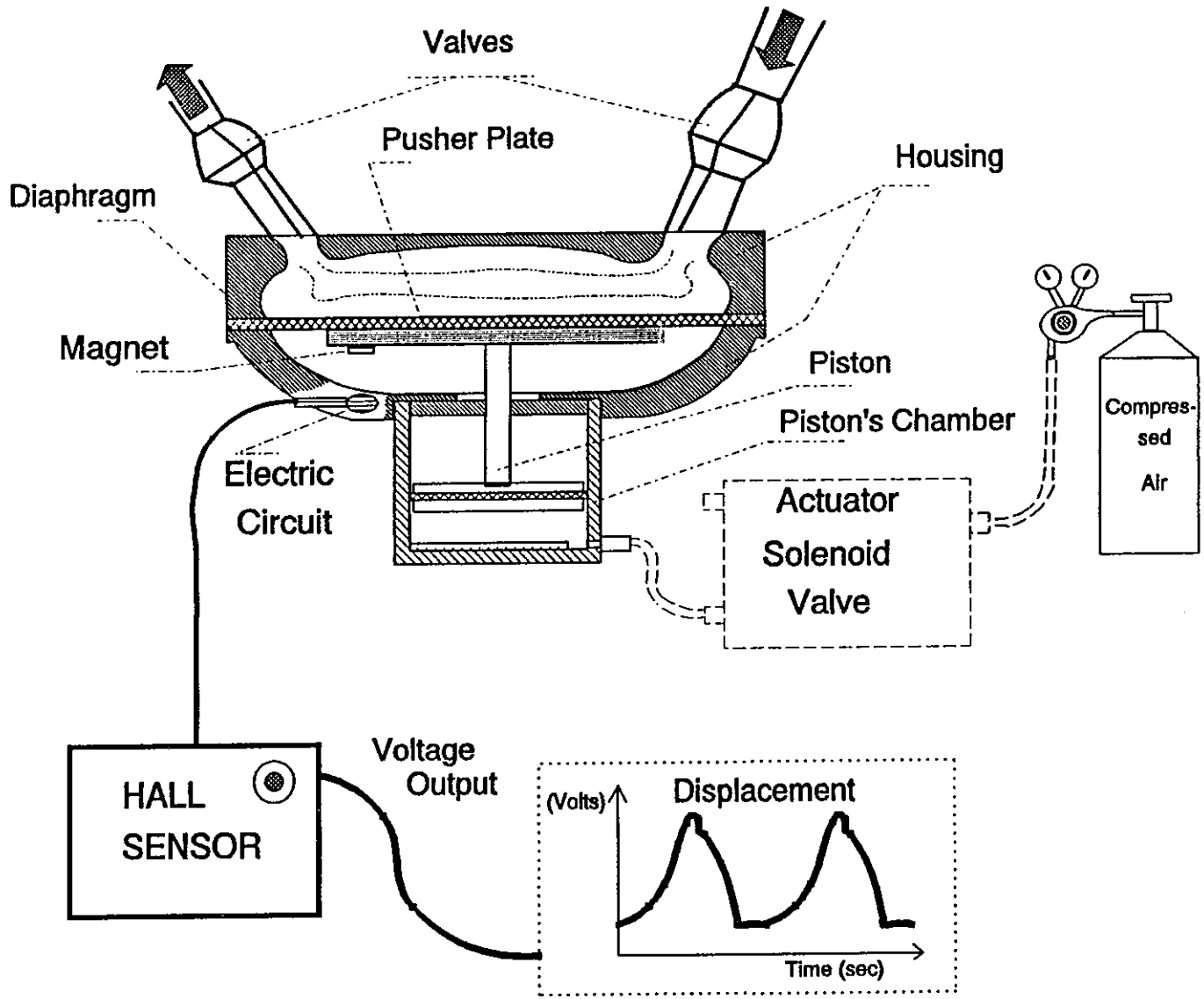

Figure 3.3: Schematic Representation of the Hall Effect Sensor Used to Determine the Pusher Plate/Diagram Displacement.

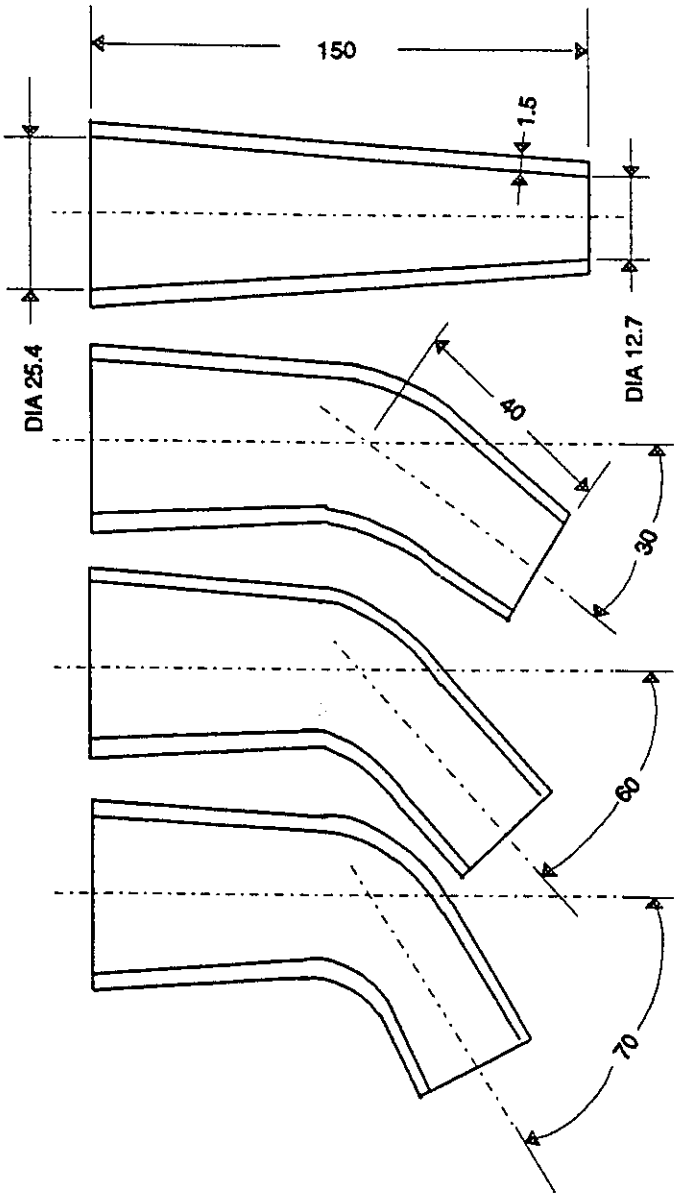

Figure 3.4: Pyrex Tubes.

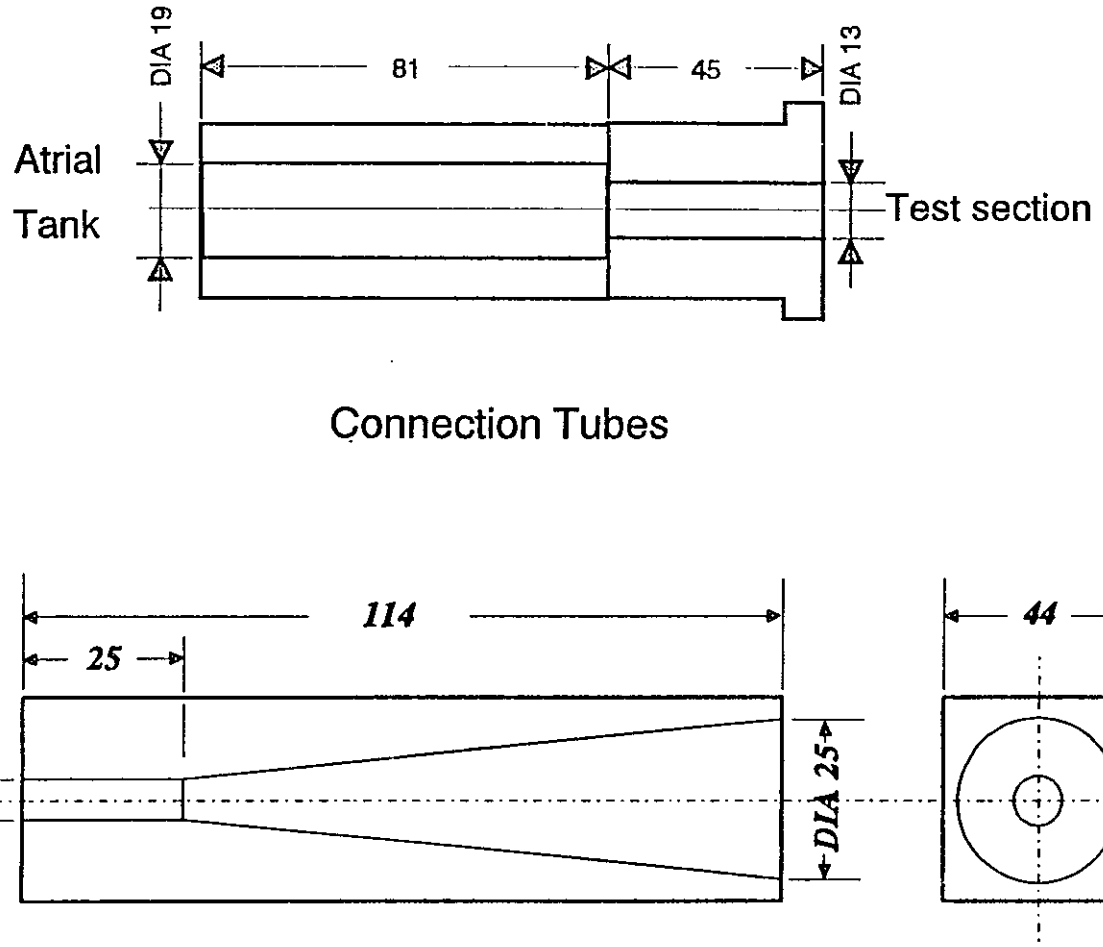

Figure 3.5: Plexiglas Tube.

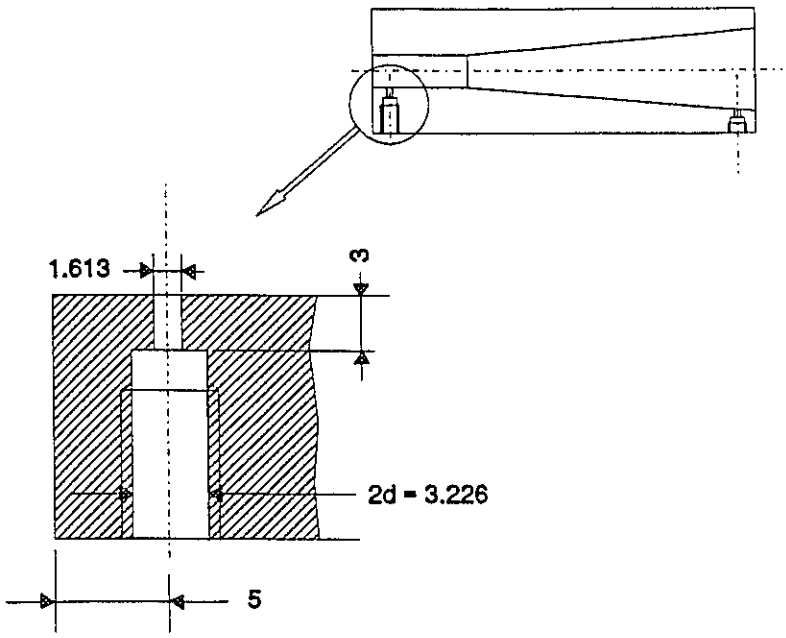

Figure 3.6: Positions of the Taps Machined on the Test Section.

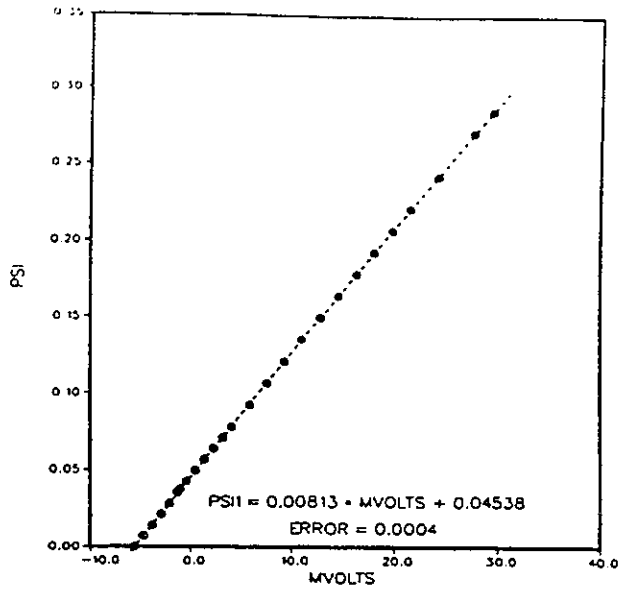

CALIBRATION CURVE OF TRANSDUCER 1

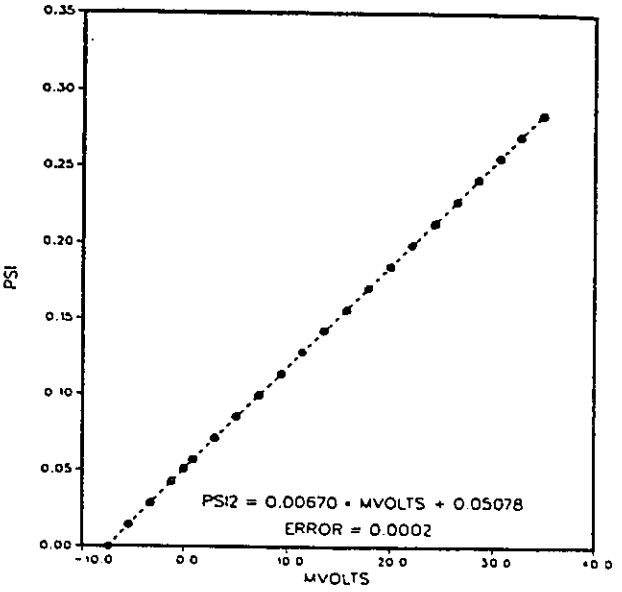

CALIBRATION CURVE OF TRANSDUCER 2

Figure 3.7: Calibration Curves for both Pressure Transducers.

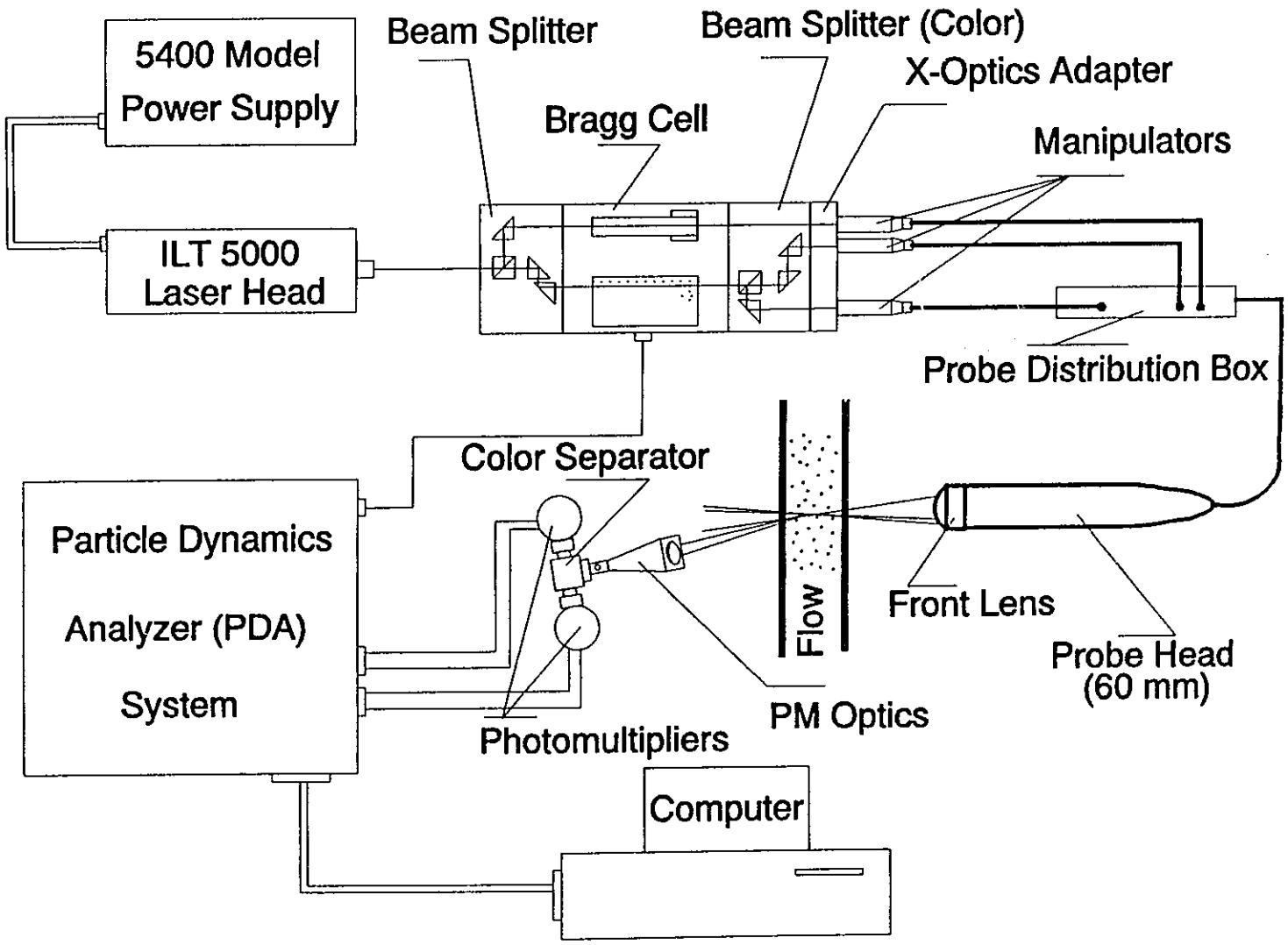

Figure 3.8: The Laser Doppler Anemometry (LDA) System.

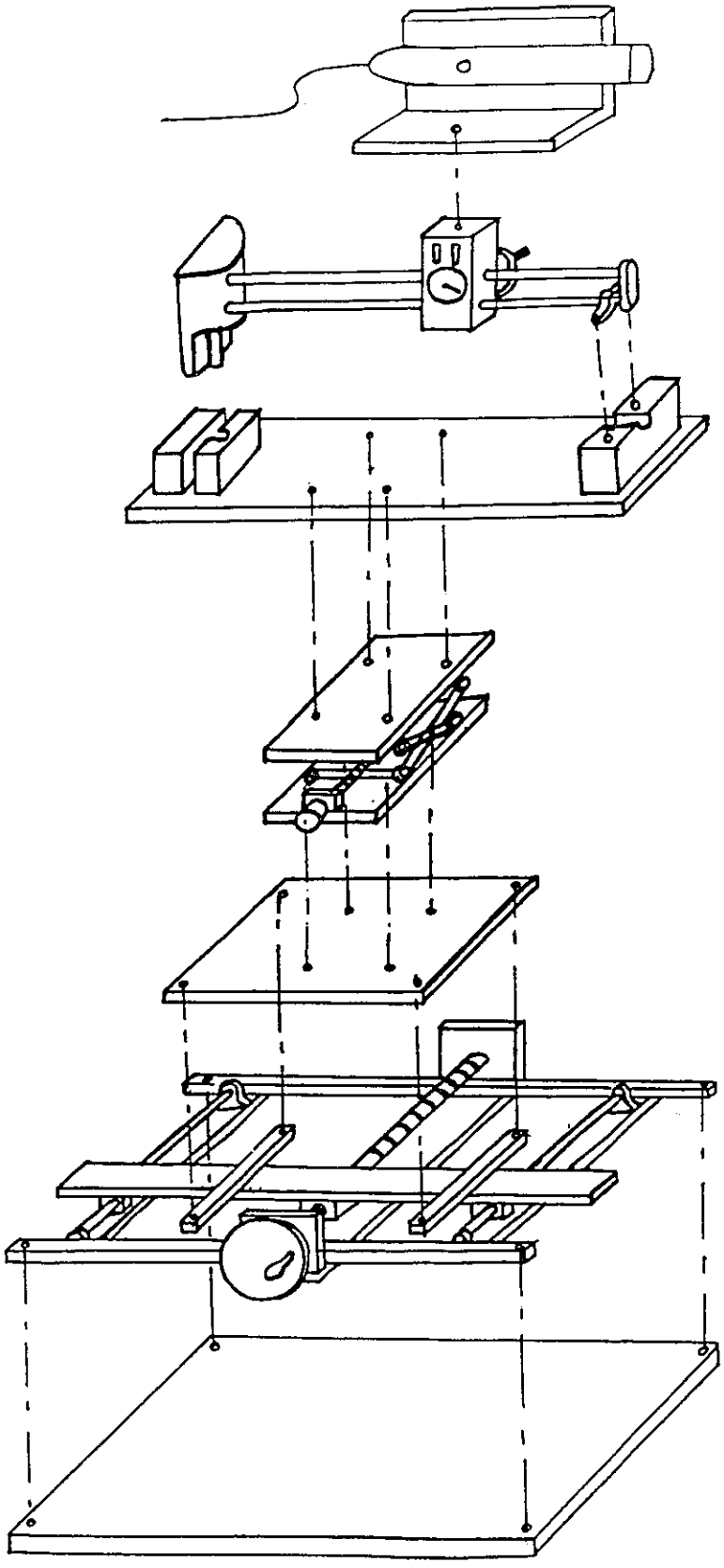

Figure 3.9: Traversing System.

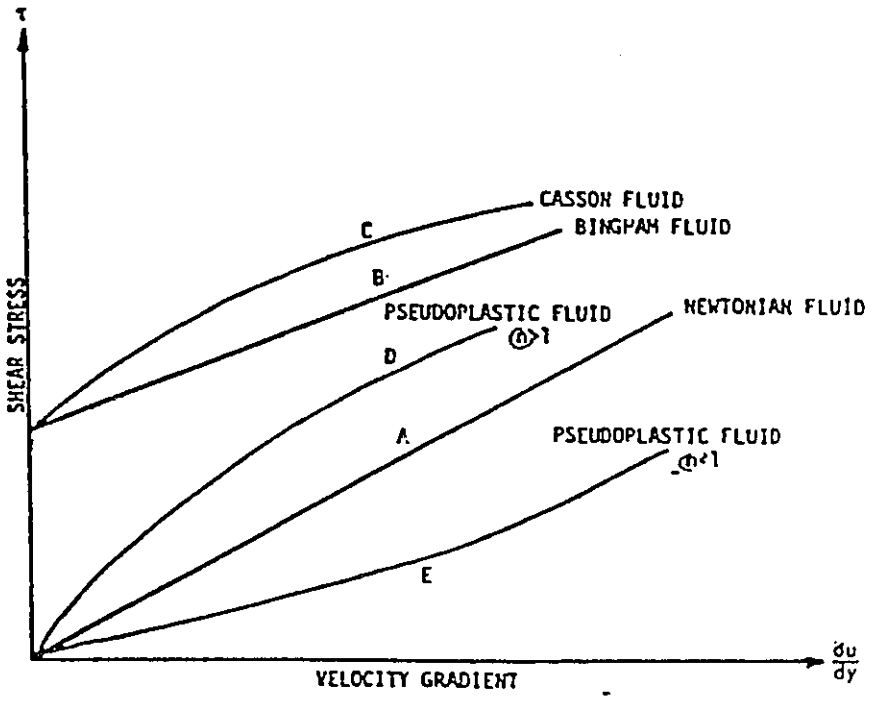

Figure 4.1: Behavior of Newtonian and non-Newtonian Fluids (Dinnar, 1981).

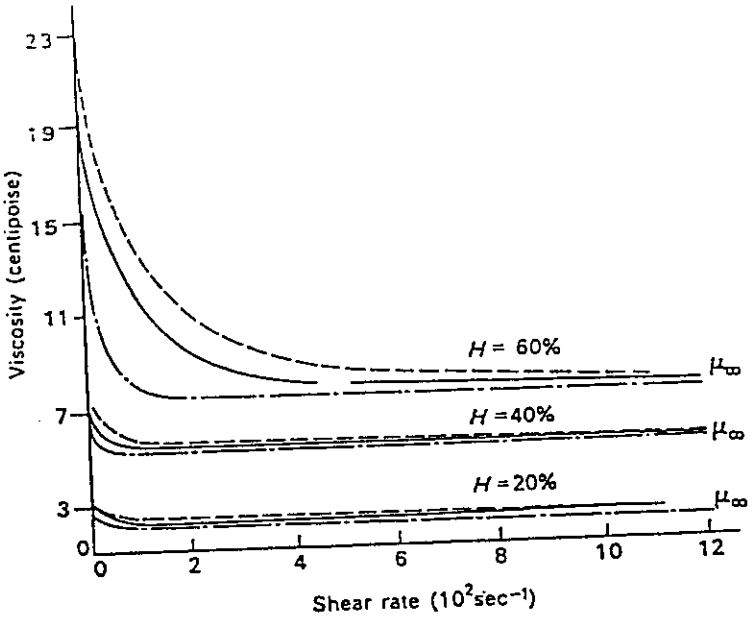

-) - apparent viscosity calculated from Poiseuille's law
-) - "differential" viscosity which is proportional to the slope of the pressure flow curve
-) - "generalized" viscosity which is proportional to the ratio of the applied stress to the shear rate at the wall.

Figure 4.2: Apparent Viscosity as a Function of Shear Rate and Hematocrit in a Small Diameter Tube (747 μm I.D.) (Mcdonald, 1974).

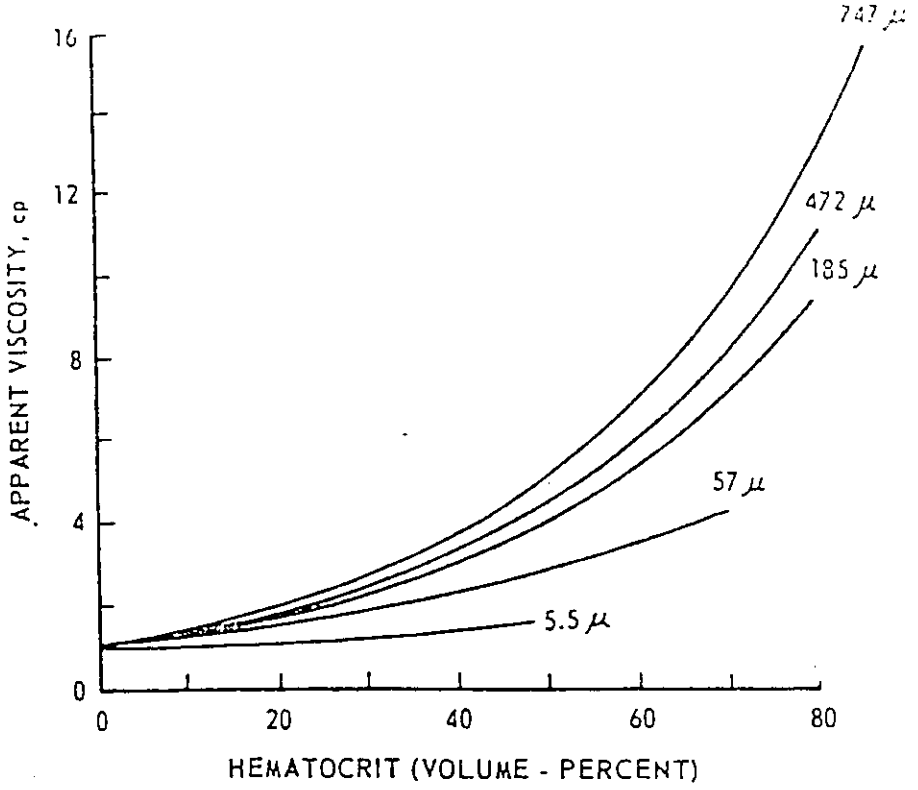

Figure 4.3: Apparent Viscosity of Blood as a Function of Hematocrit and Capillary Diameter (Rudinger, 1966).

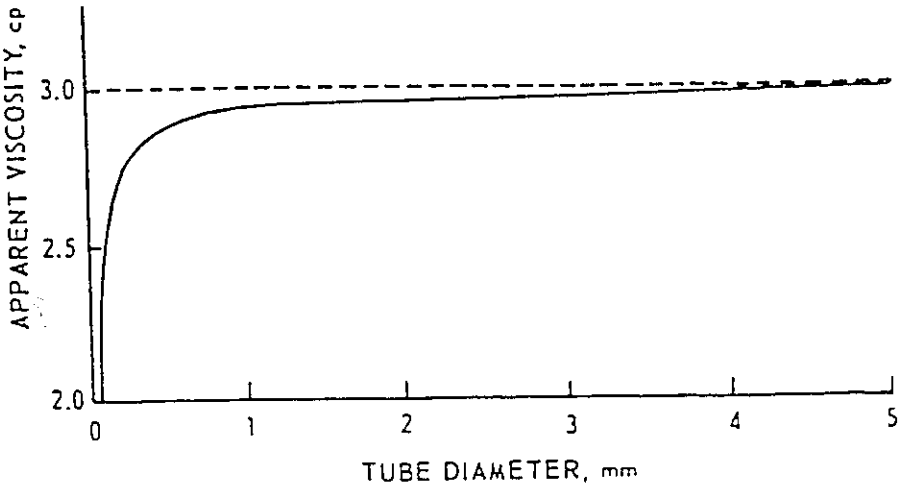

Figure 4.4: Effect of the Tube Diameter on Apparent Viscosity of Blood for a Hematocrit of 40% and a Temperature of $38°C$ (Rudinger, 1966).

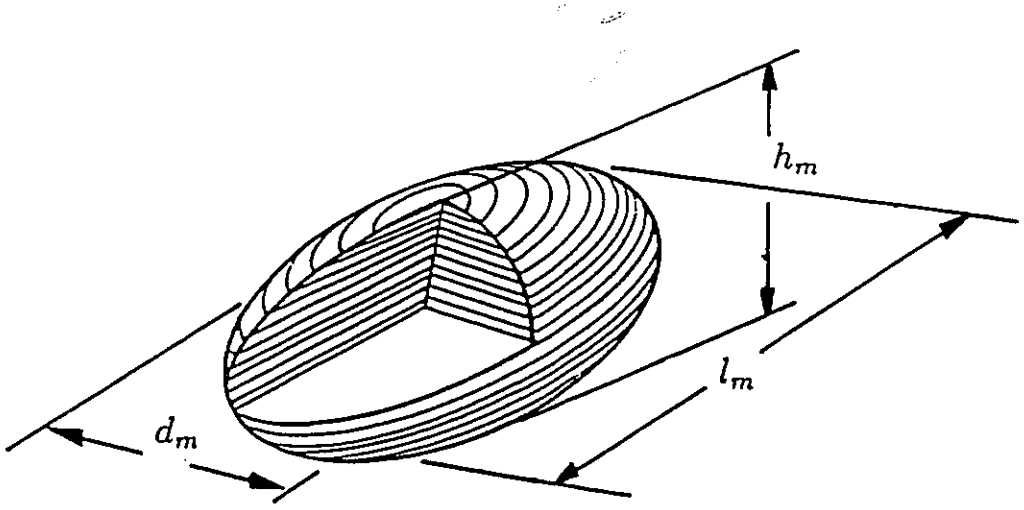

Figure 4.16: Probe Volume Parameters.

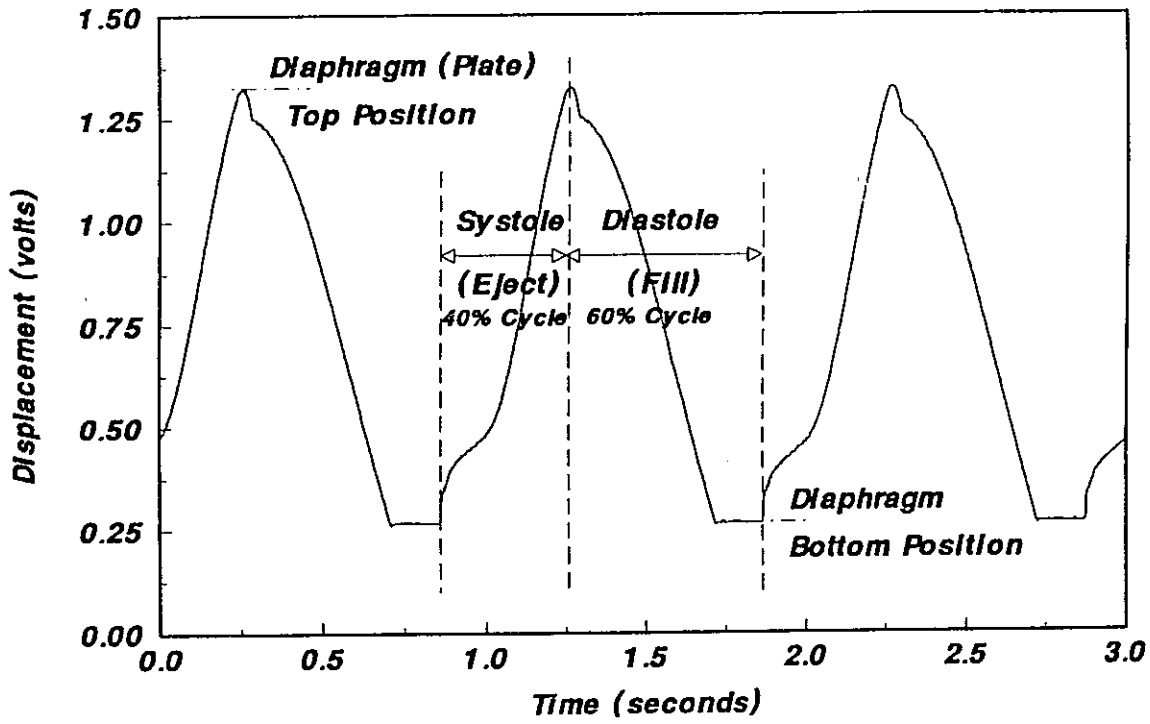

Figure 5.1: Diaphragm Displacement Signal During the Pumping Cycle.

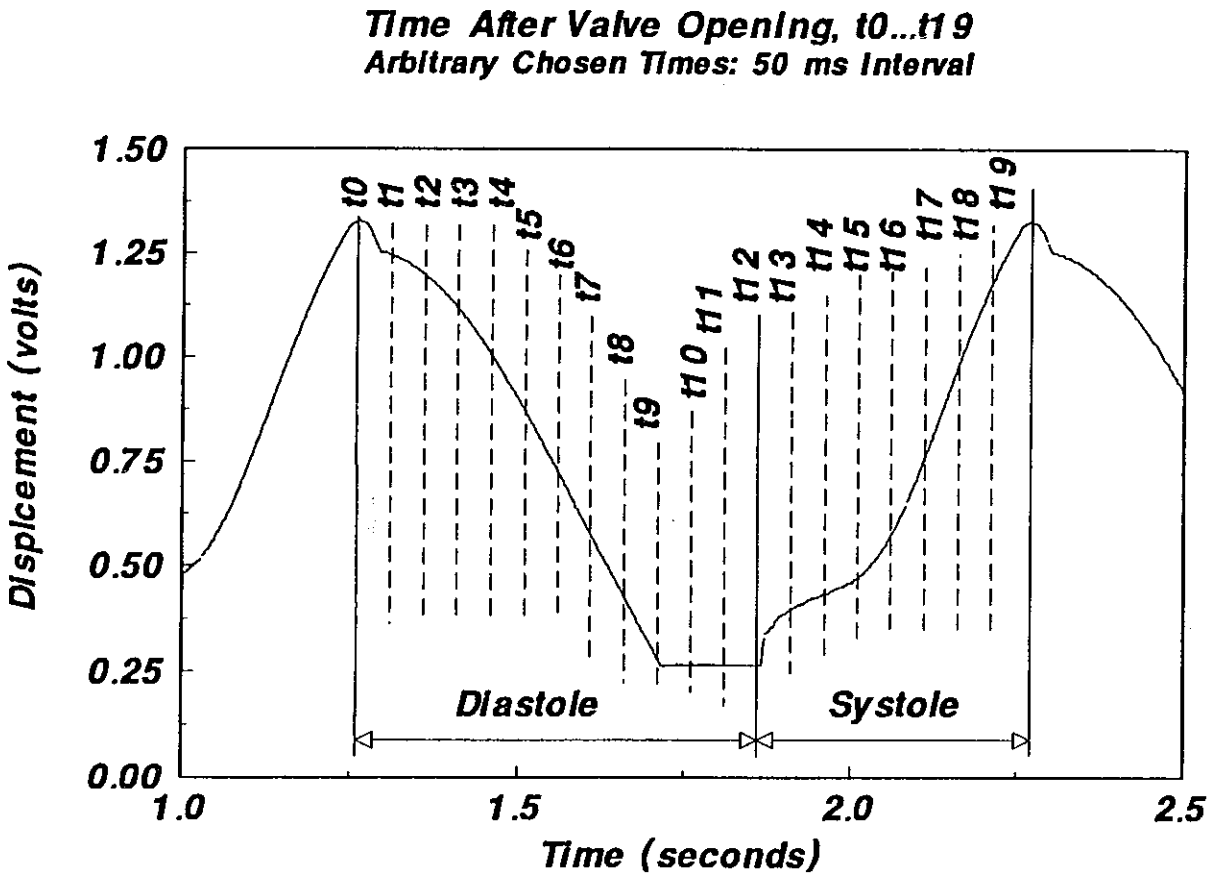

Figure 5.2: Arbitrary Equal Time Intervals used to Analyse the Flow Profiles During one Cycle.

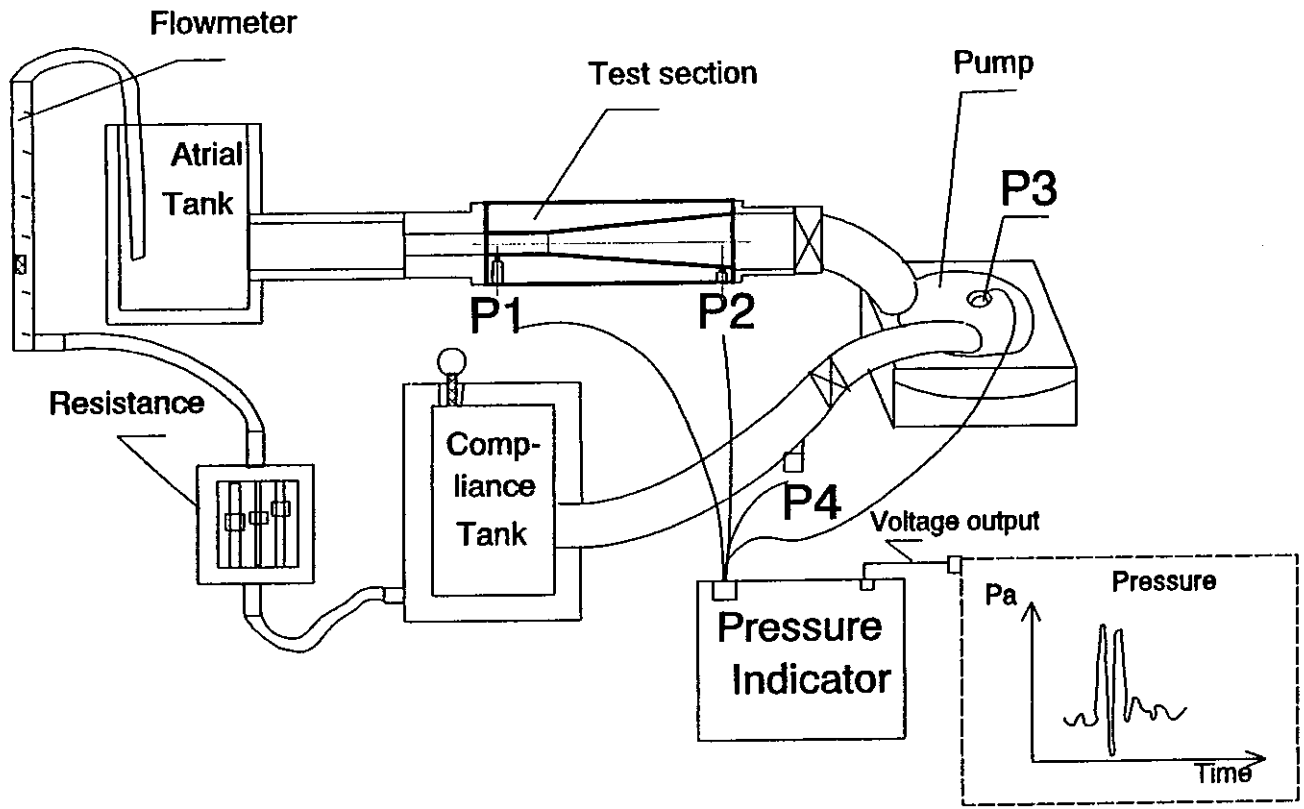

Figure 5.3: Schematic Representation of the Experimental Setup, indicating the Four Locations, P1, P2, P3 and P4, for Pressure Measurements.

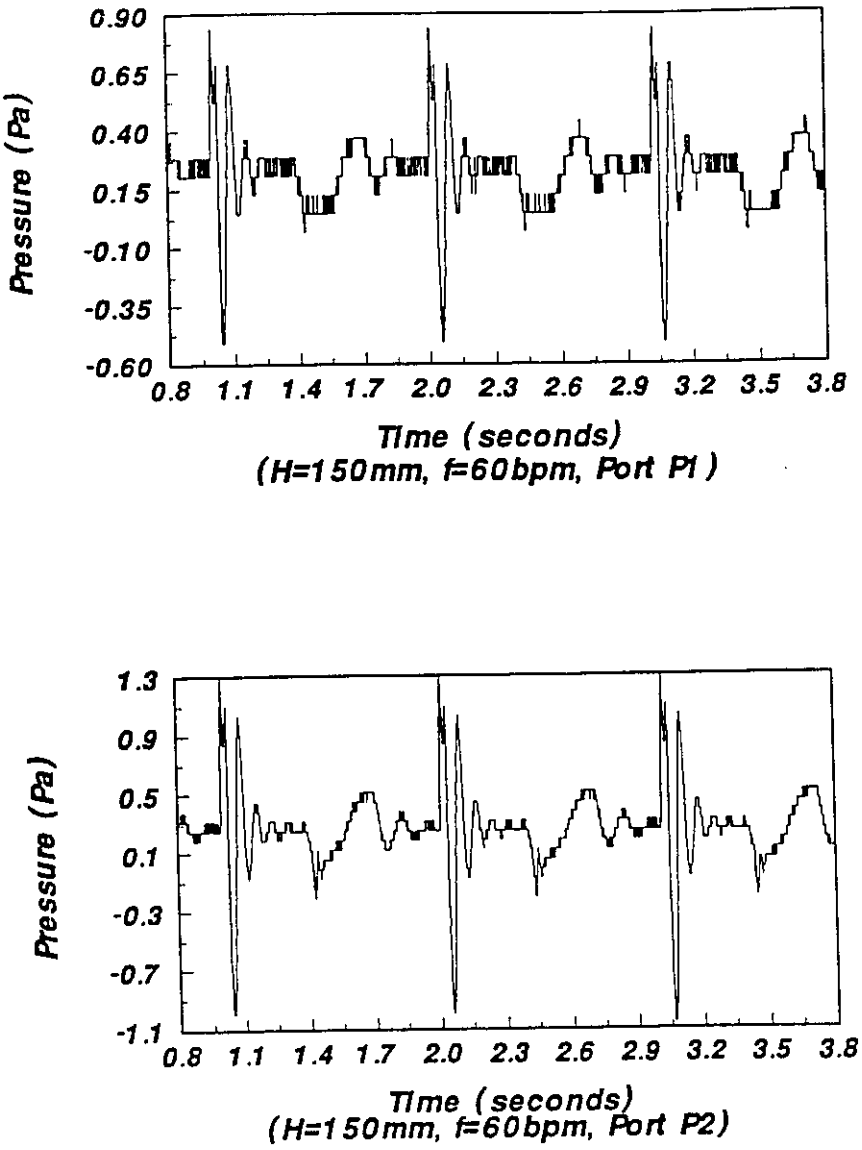

Figure 5.4: Pressure Variation near the Entrance (top) and the Exit (bottom) of the Conical Tube Section.

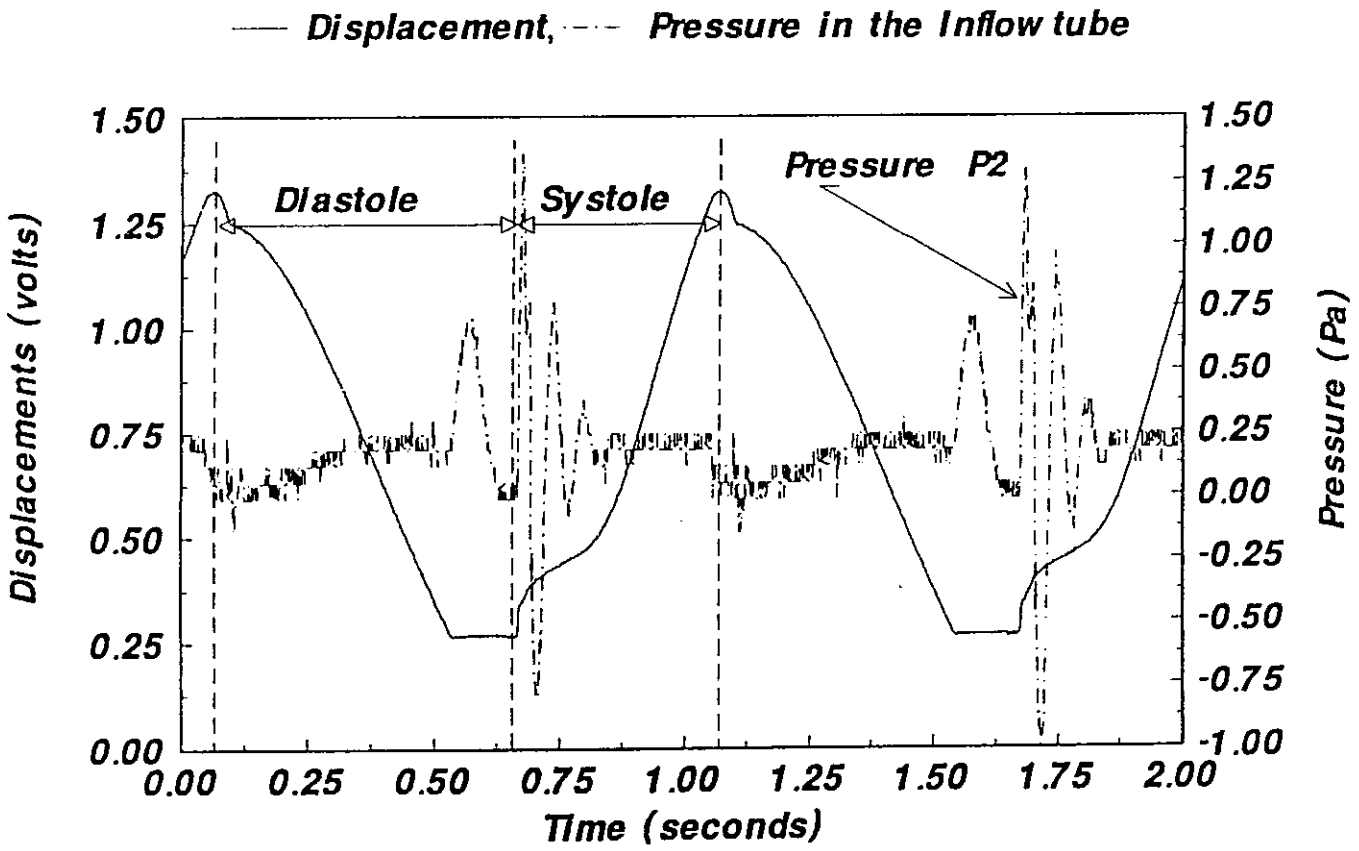

Figure 5.5: Simultaneous Measurements of the Displacement and the Pressure in the Inflow Tube at P2.

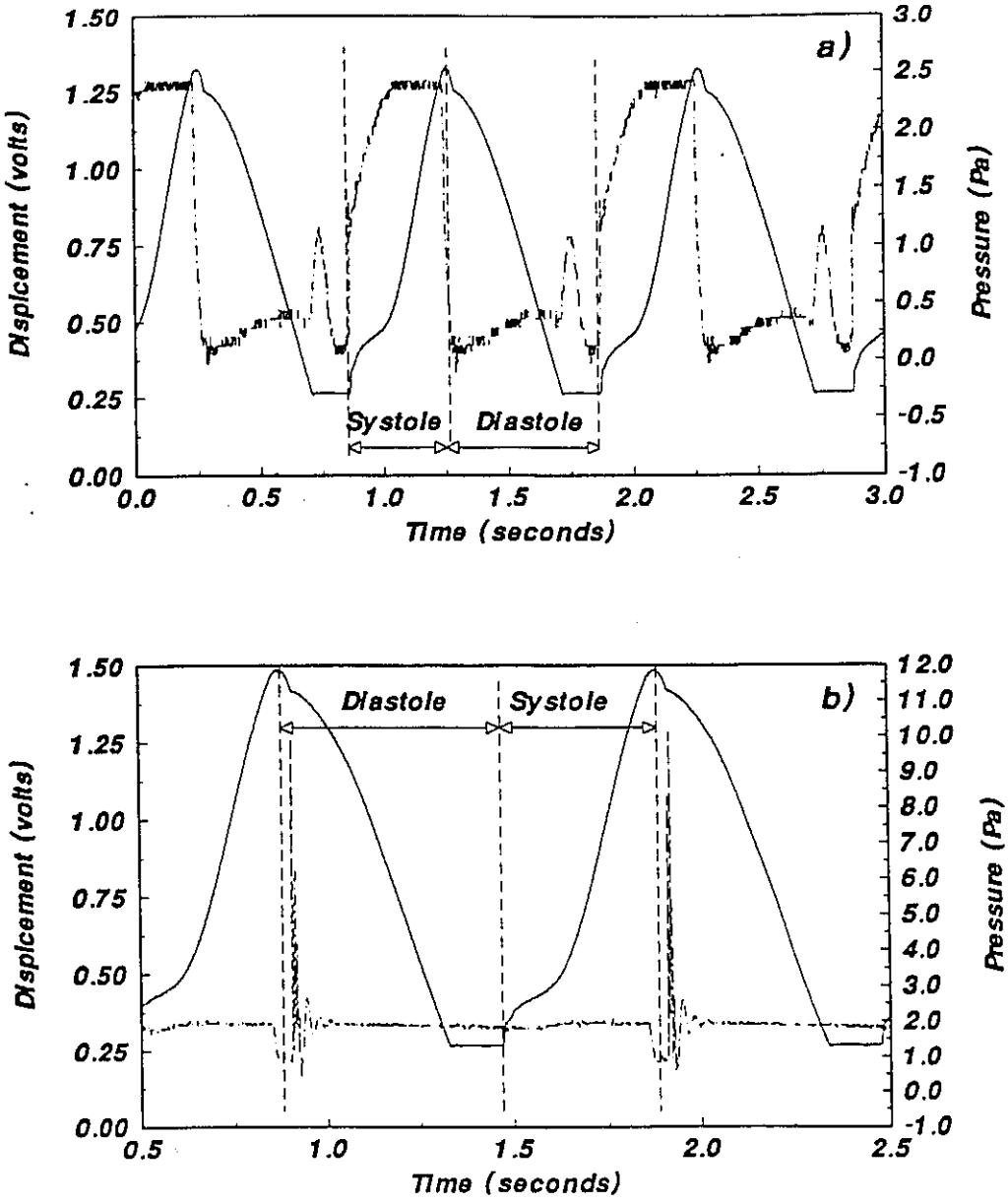

Figure 5.6: Simultaneous Measurements of: a) Displacement and Pressure in the Heart Chamber at P3, b) Displacement and Pressure in the Outflow Tube at P4.

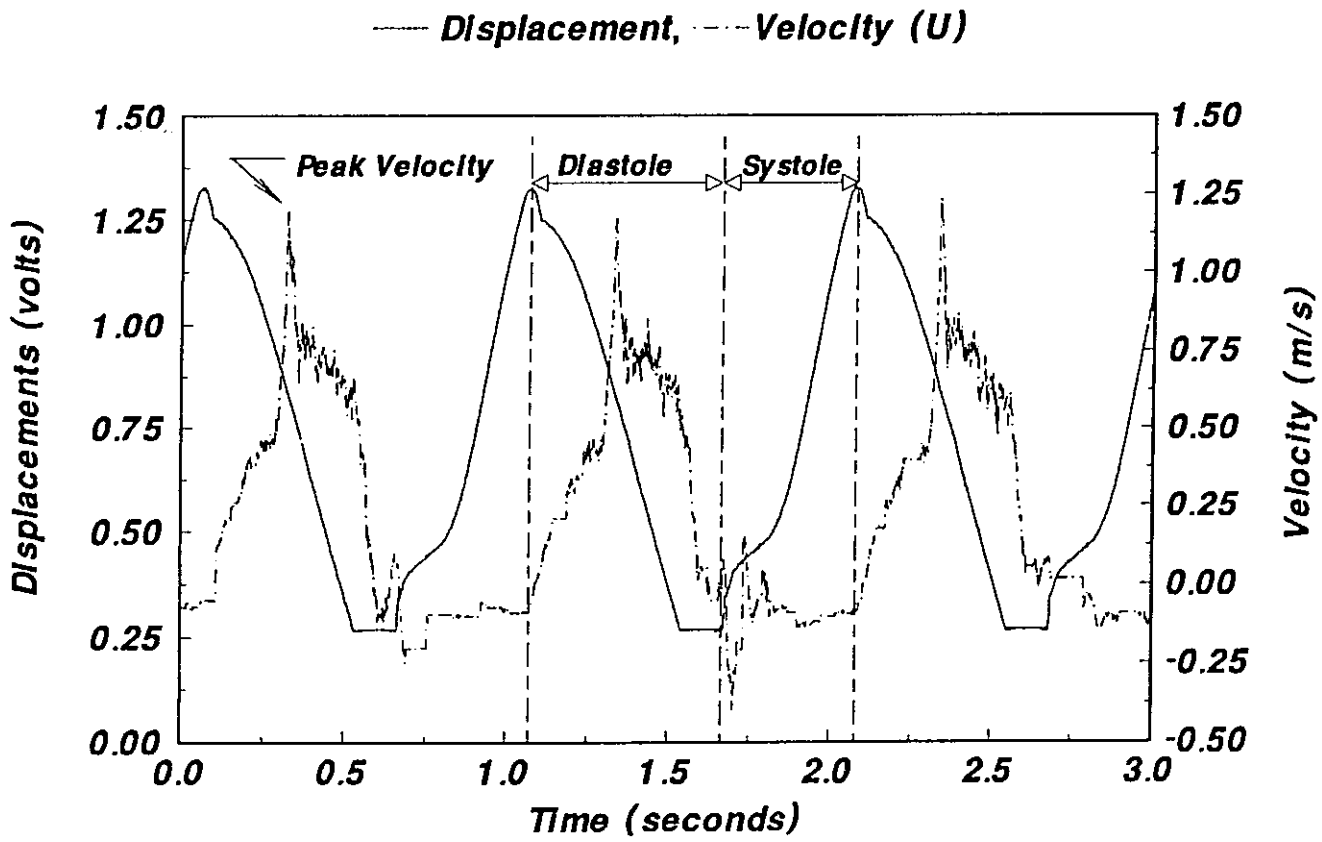

Figure 5.7: Simultaneous Measurements of the Displacement and the Velocity in the Conical Part of the Tube.

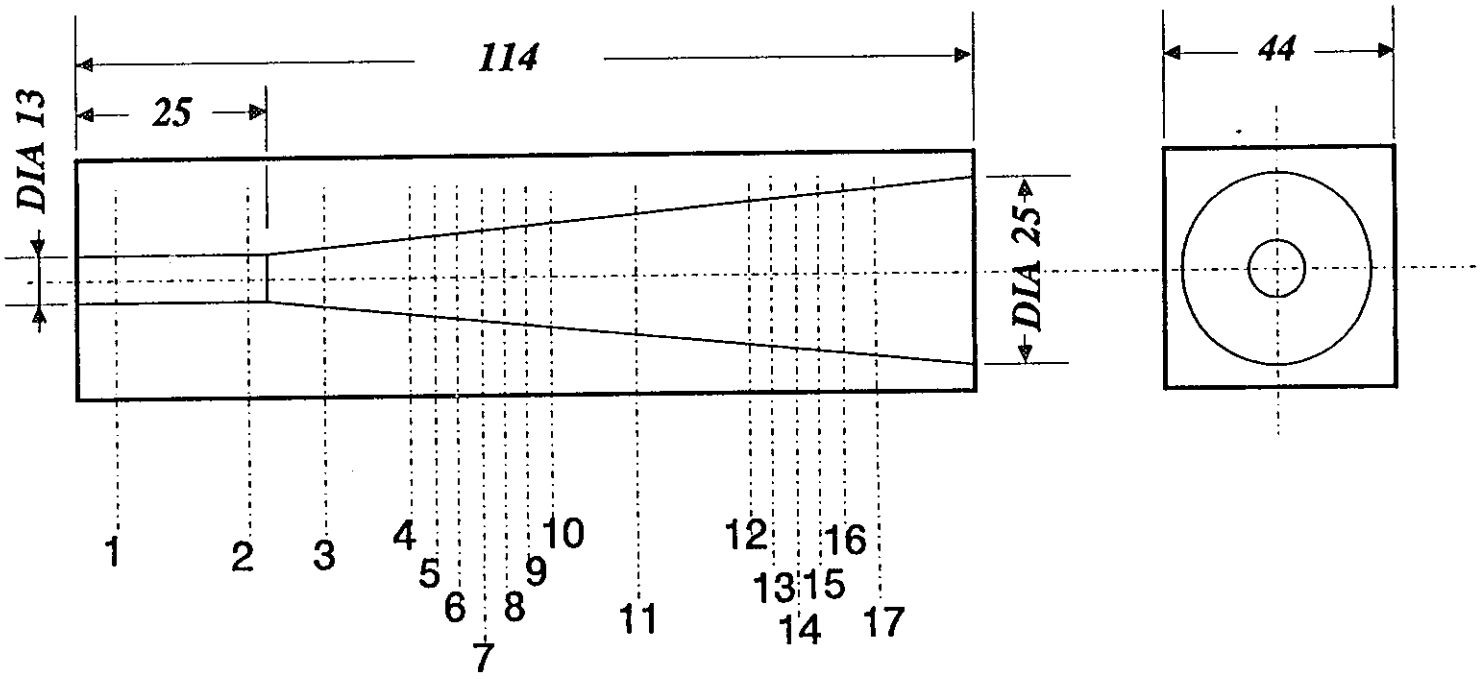

Figure 5.8: Radial Profiles Positions for the Velocity Measurements in the Test Tube.

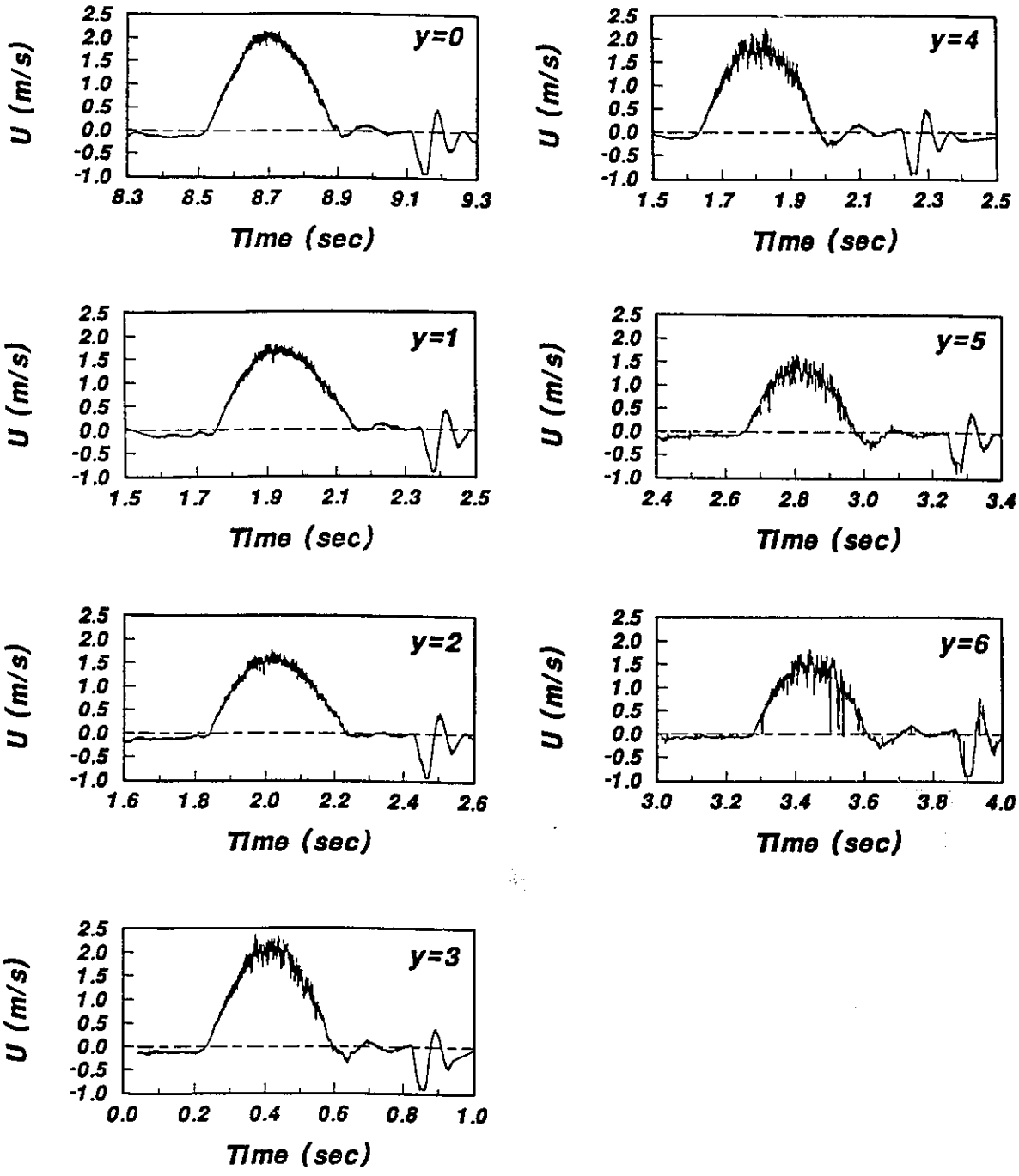

Figure 5.9: Axial Velocity Cycles at Different Locations along the Radial Profile 2.

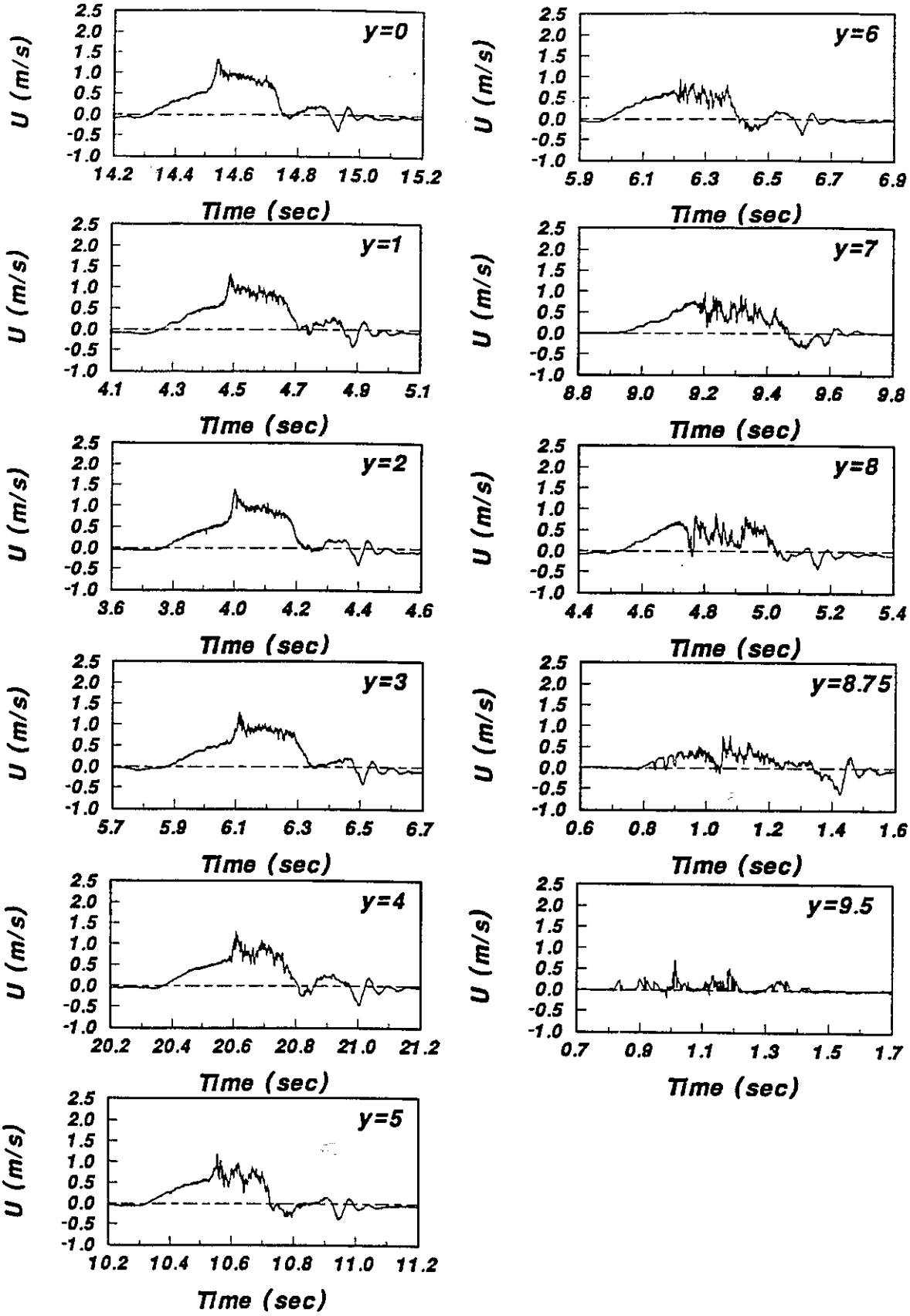

Figure 5.10: Axial Velocity Cycles at Different Locations along the Radial Profile 11.

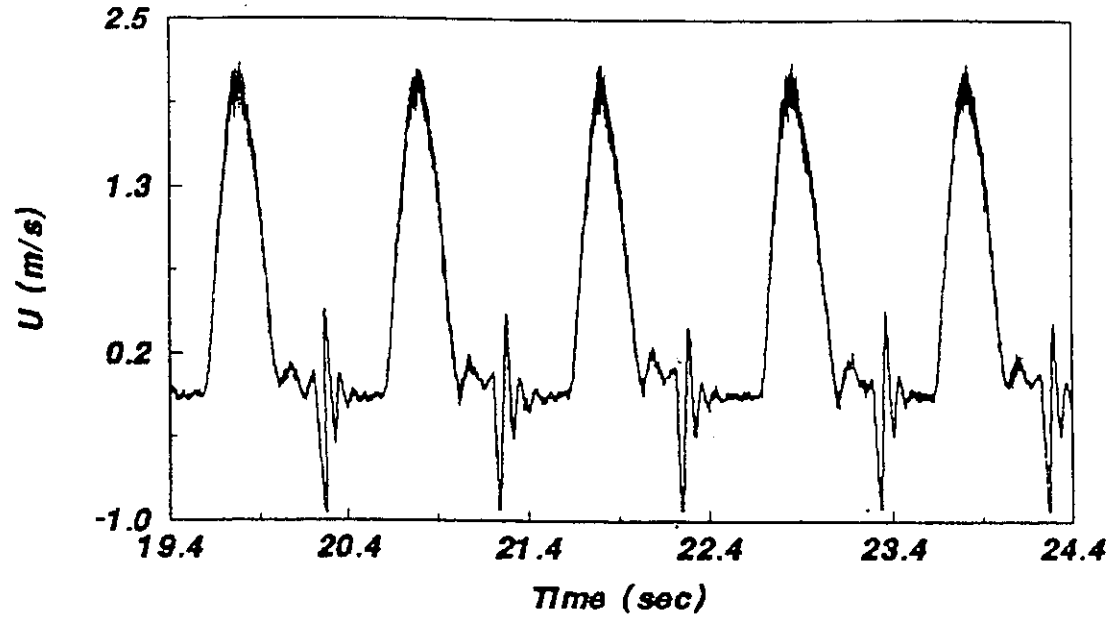

Figure 5.11: Axial Velocity Cycles at the Centerline of Profile 2.

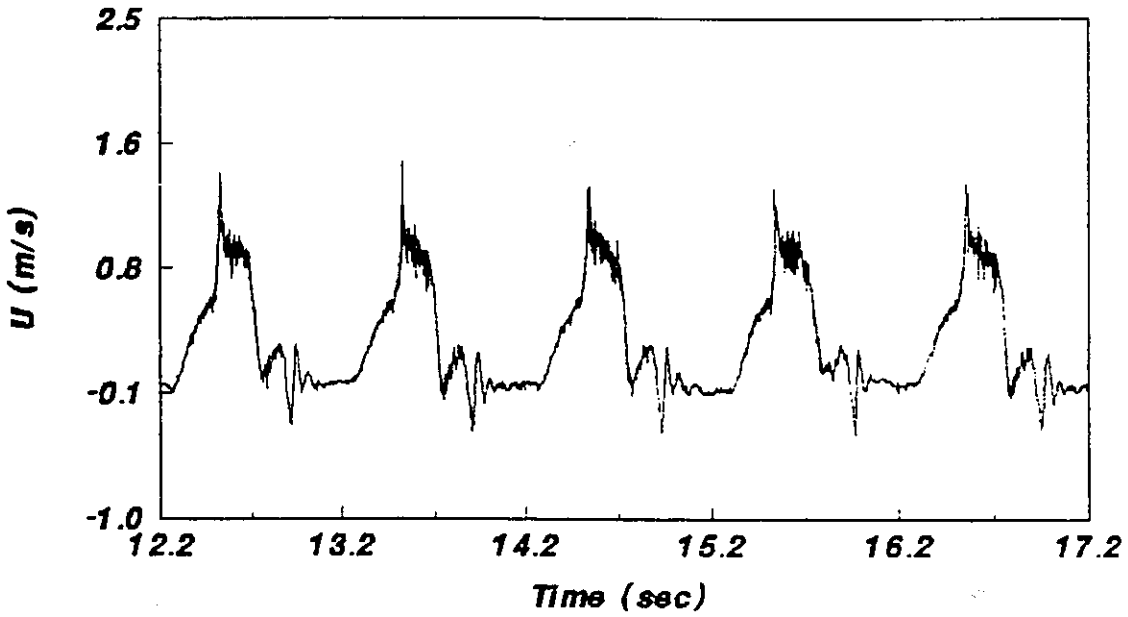

Figure 5.12: Axial Velocity Cycles at the Centerline of Profile 11.

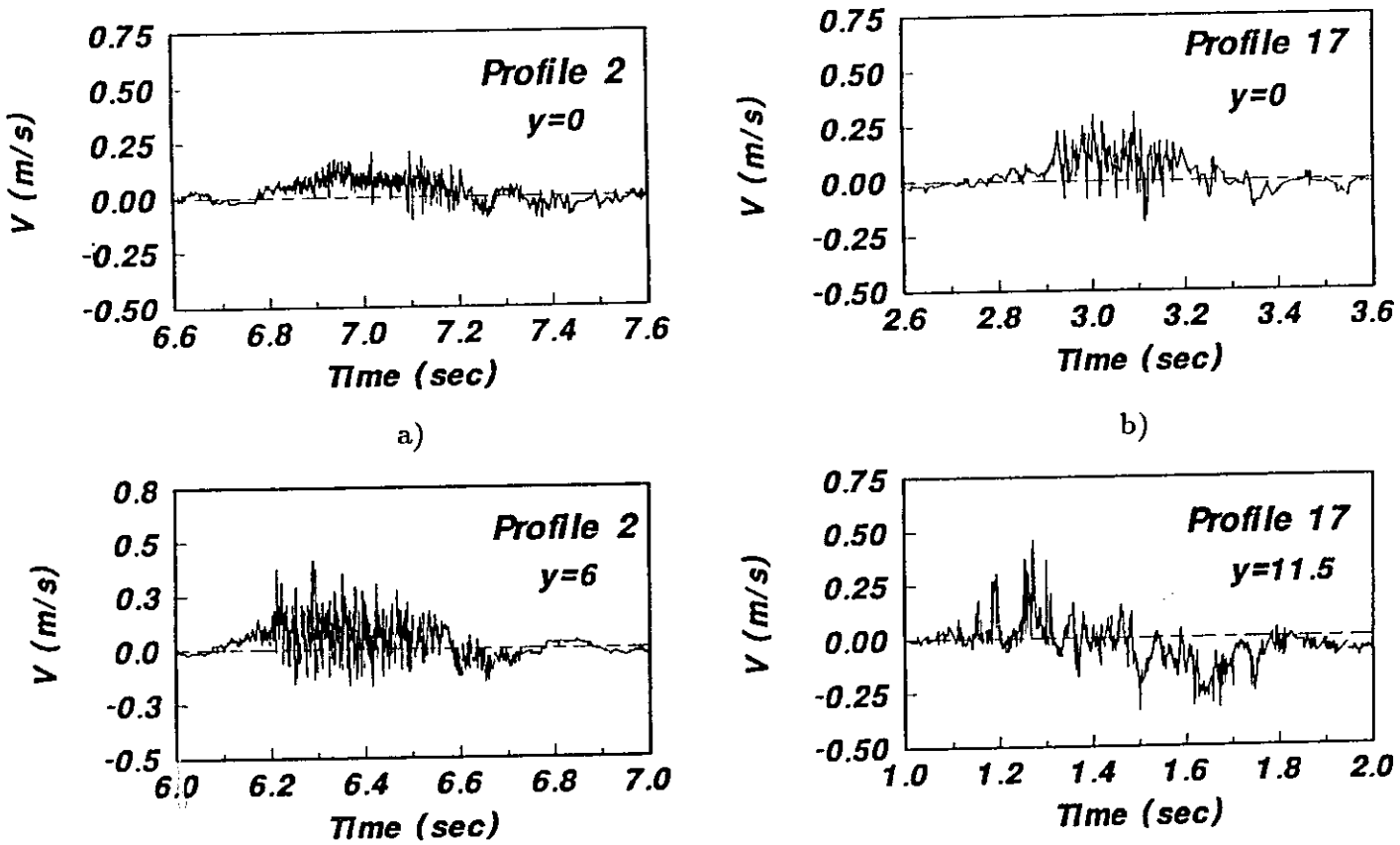

Figure 5.13: Azimuthal Velocity Cycles at the Centerline and near the Wall for Profiles 2 and 17.

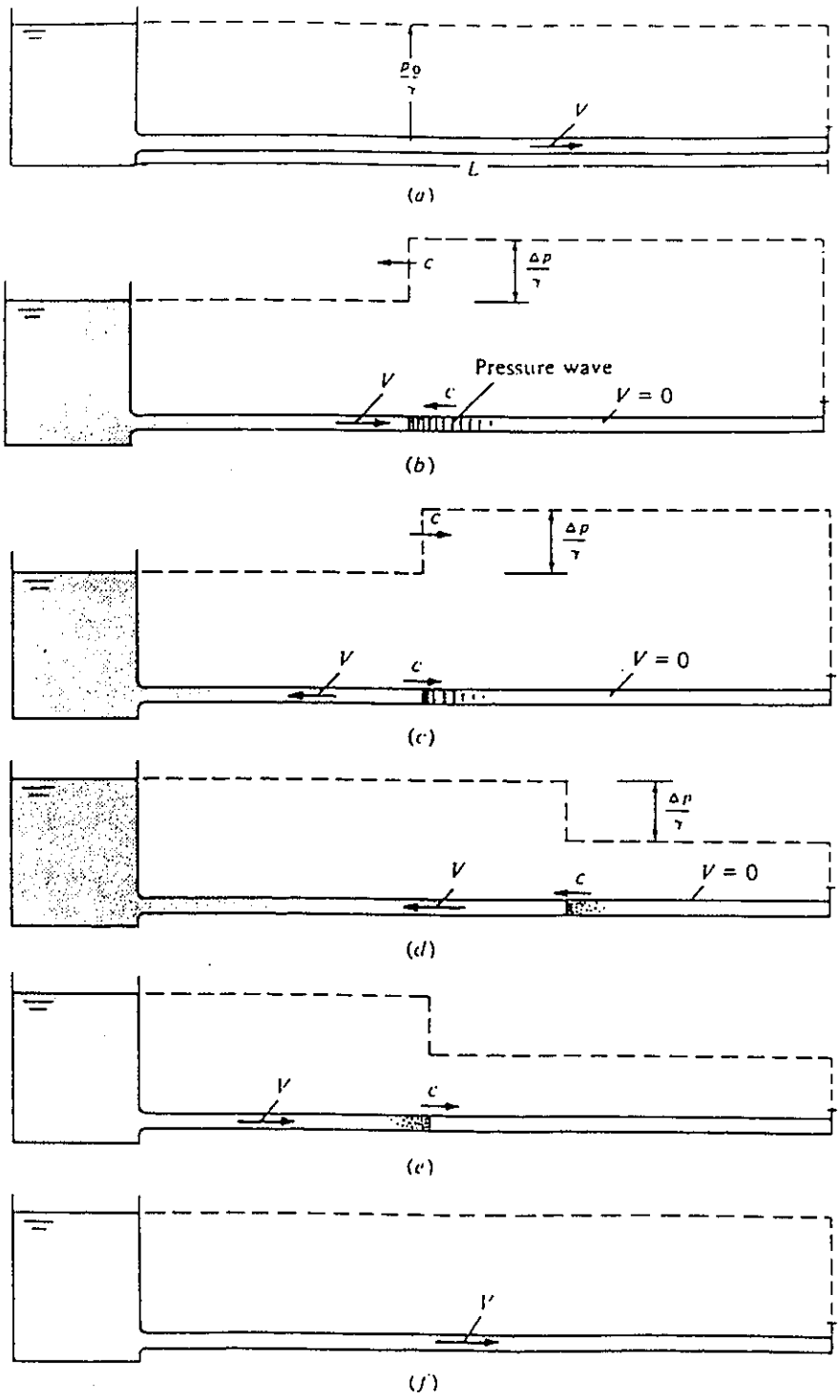

Figure 6.1: Water-Hammer Process. (a) Initial Condition. (b) During Time $0 < t < L/c$. (c) During Time $L/c < t < 2L/c$. (d) During Time $2L/c < t < 3L/c$. (e) During Time $3L/c < t < 4L/c$. (f) During Time t = 4L/c. (Roberson et al., 1985).

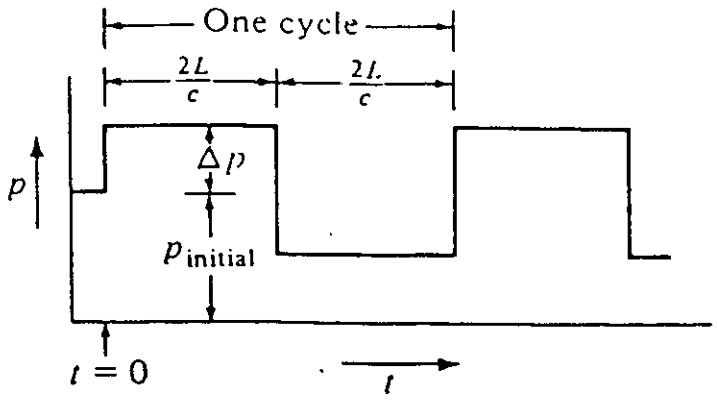

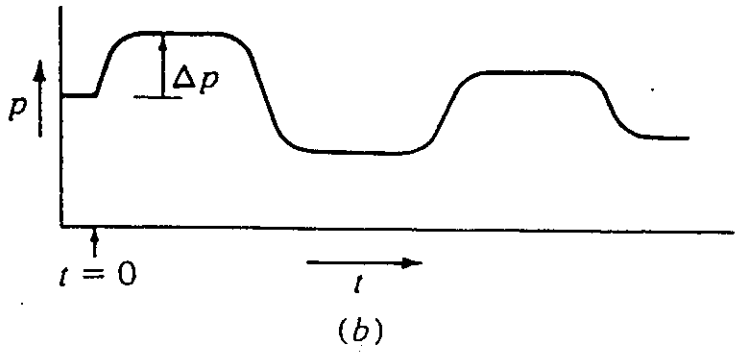

Figure 6.2: a) Variation of Water-Hammer Pressure with Time at an Adjacent Location to the Valve. b) Actual Variation of Pressure. (Roberson et al., 1985).

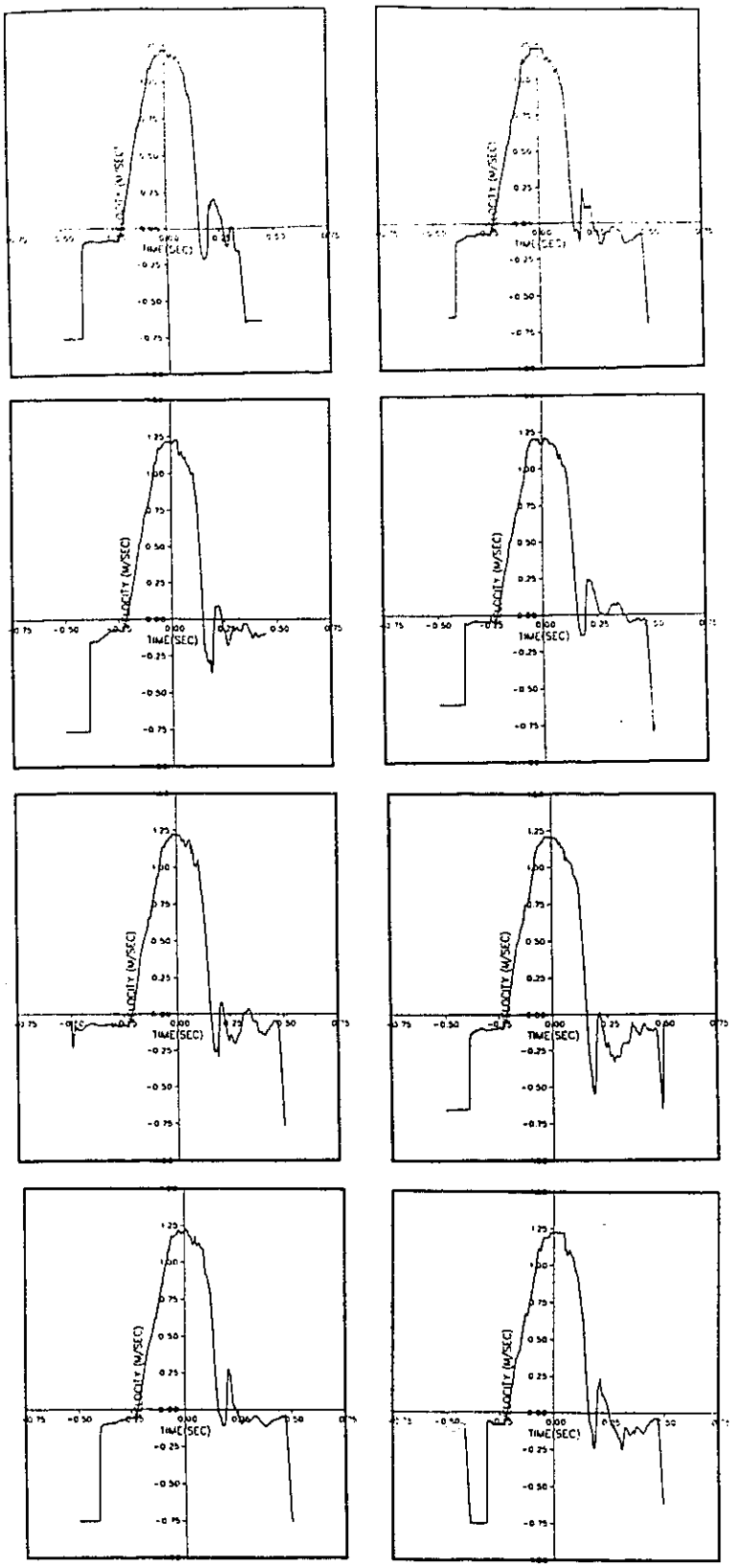

Figure 6.3: 8 Cycles of the Axial Velocity at the Centerline of the Tube's Straight Section.

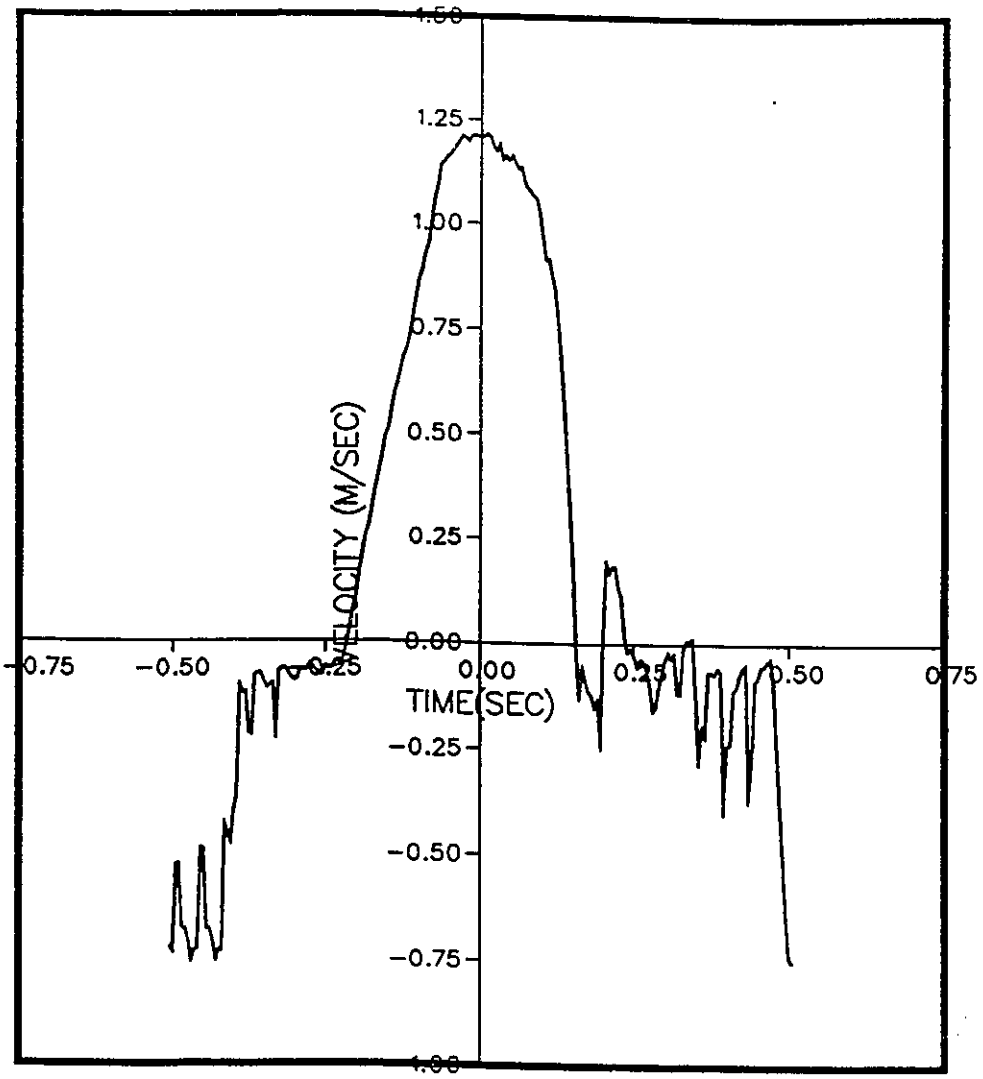

Figure 6.4: Average Cycle of the 8 Cycles Shown in Figure 6.3.

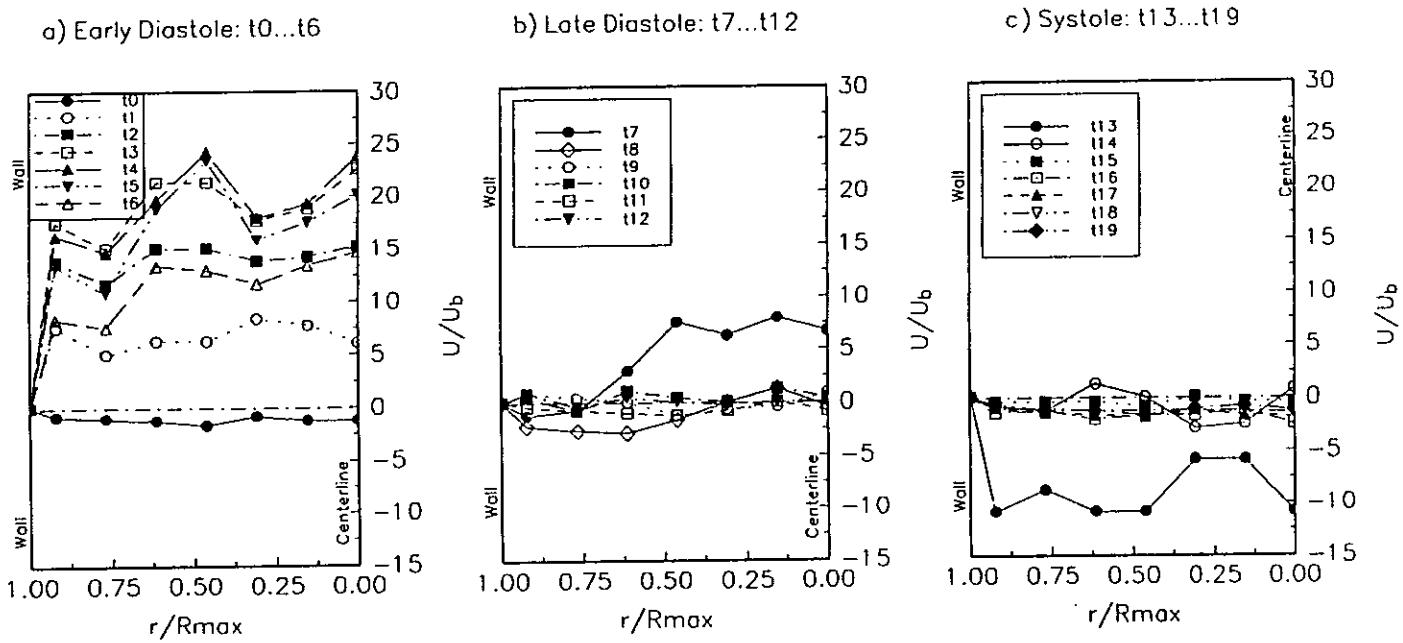

Figure 6.5: Radial Profile 2 of the Axial Velocity: a) Early Diastole, b) Late Diastole, c) Systole.

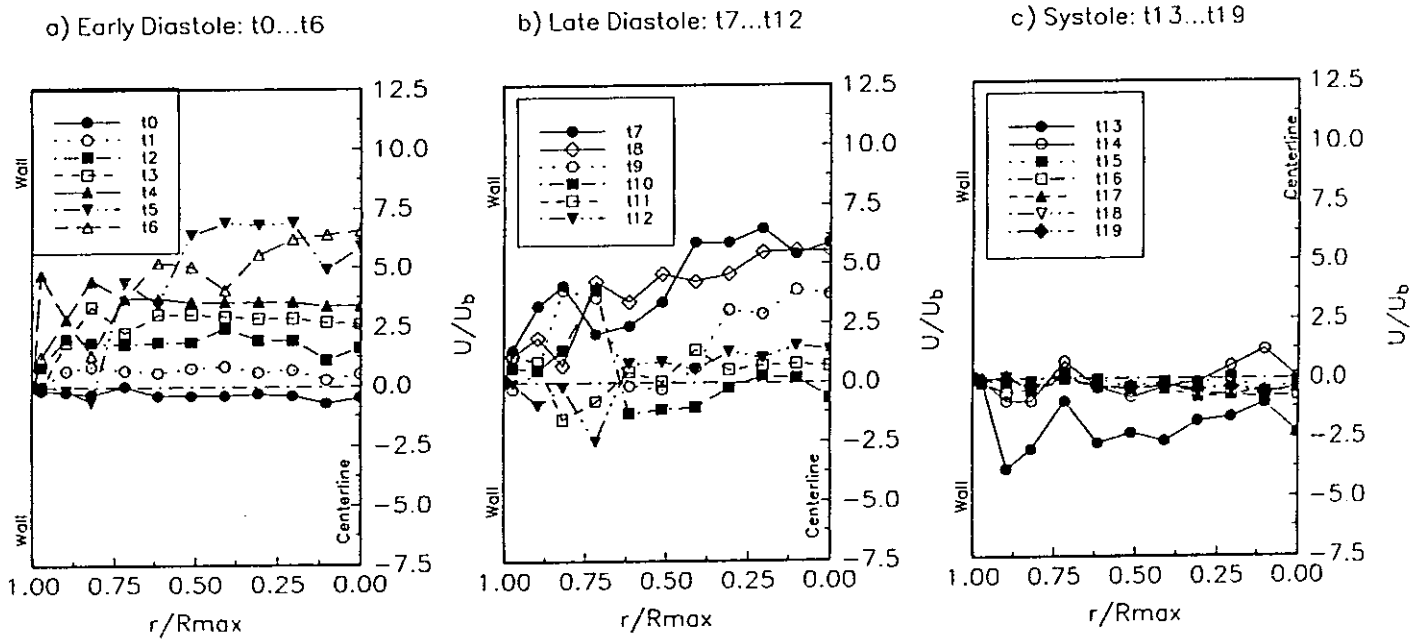

Figure 6.6: Radial Profile 11 of the Axial Velocity: a) Early Diastole, b) Late Diastole, c) Systole.

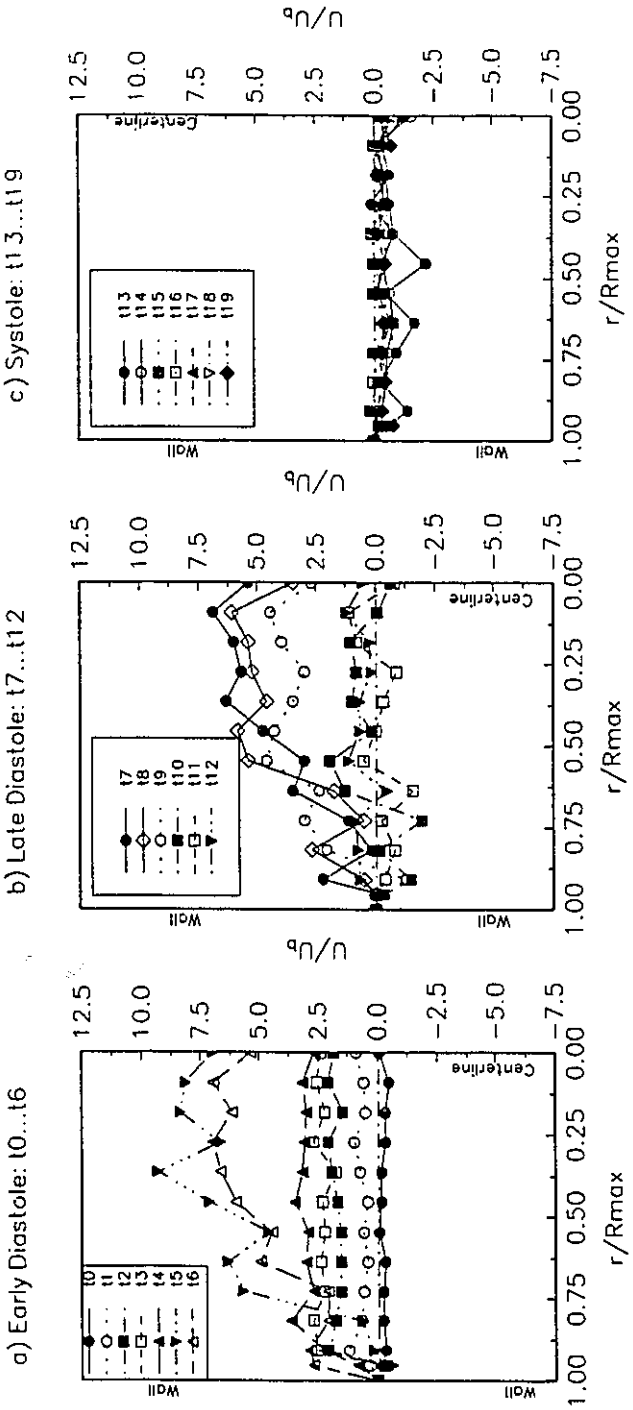

Figure 6.7: Radial Profile 12 of the Axial Velocity: a) Early Diastole, b) Late Diastole, c) Systole.

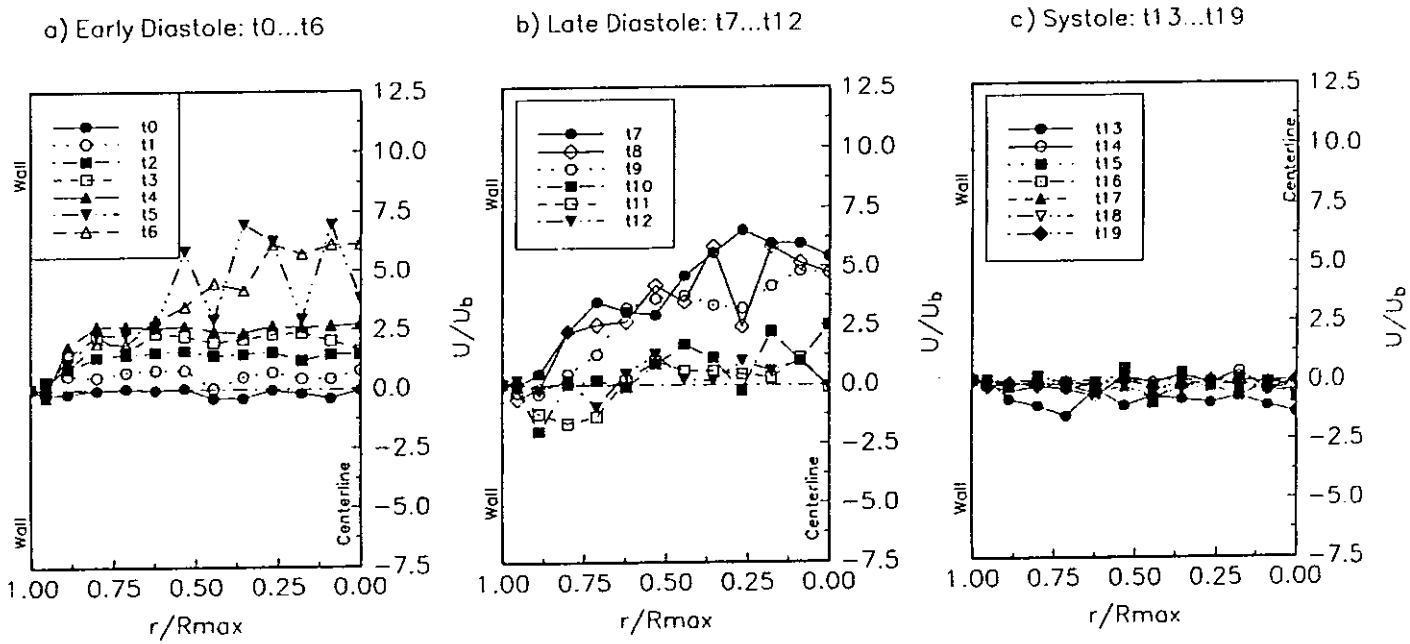

Figure 6.8: Radial Profile 13 of the Axial Velocity: a) Early Diastole, b) Late Diastole, c) Systole.

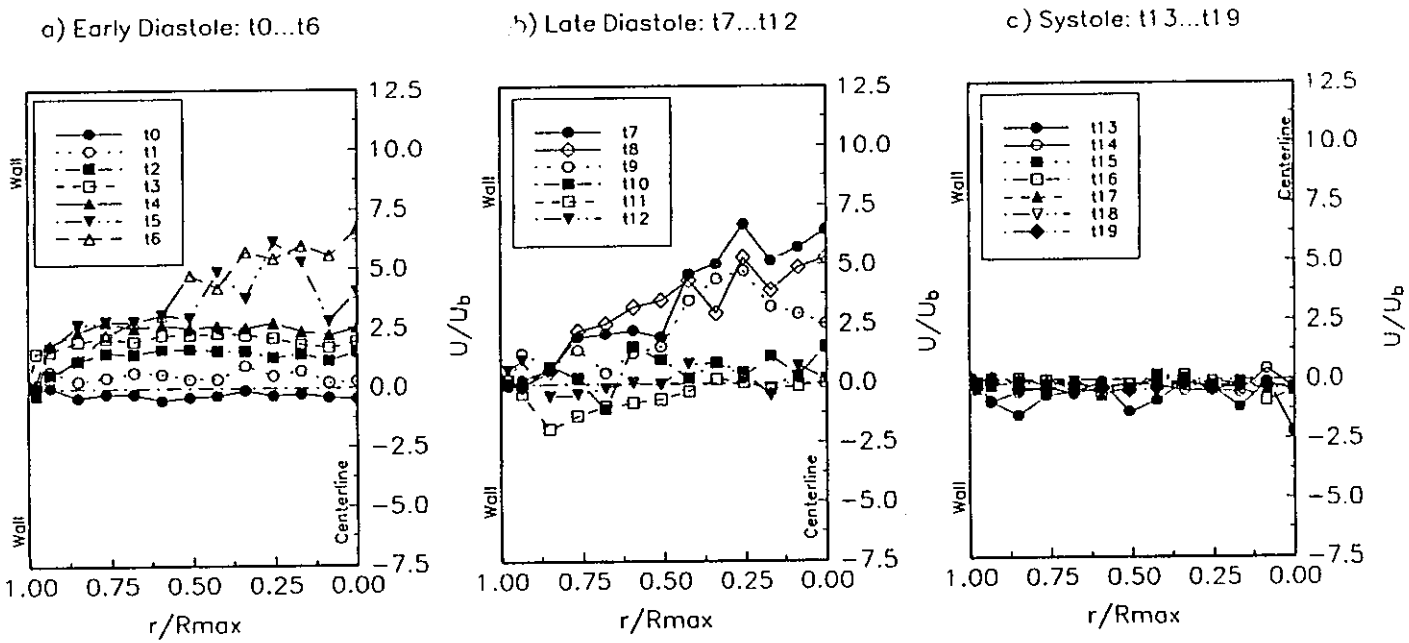

Figure 6.9: Radial Profile 15 of the Axial Velocity: a) Early Diastole, b) Late Diastole, c) Systole.

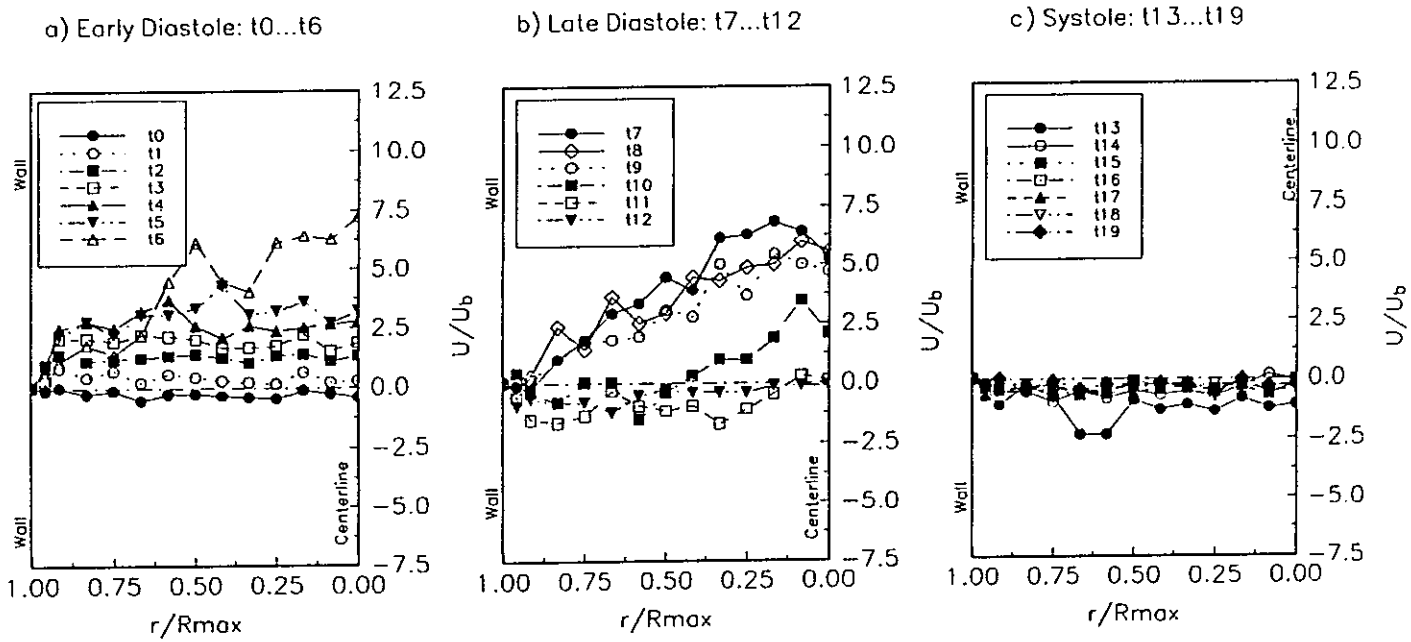

Figure 6.10: Radial Profile 16 of the Axial Velocity: a) Early Diastole, b) Late Diastole, c) Systole.

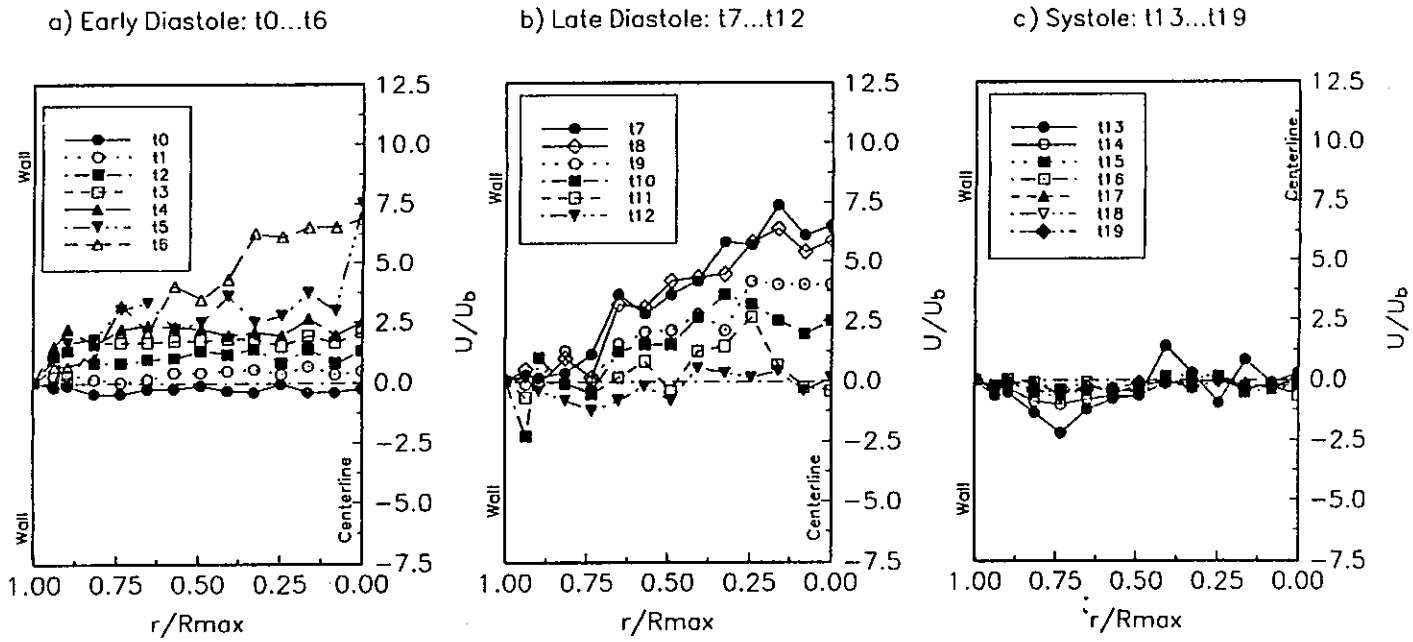

Figure 6.11: Radial Profile 17 of the Axial Velocity: a) Early Diastole, b) Late Diastole, c) Systole.

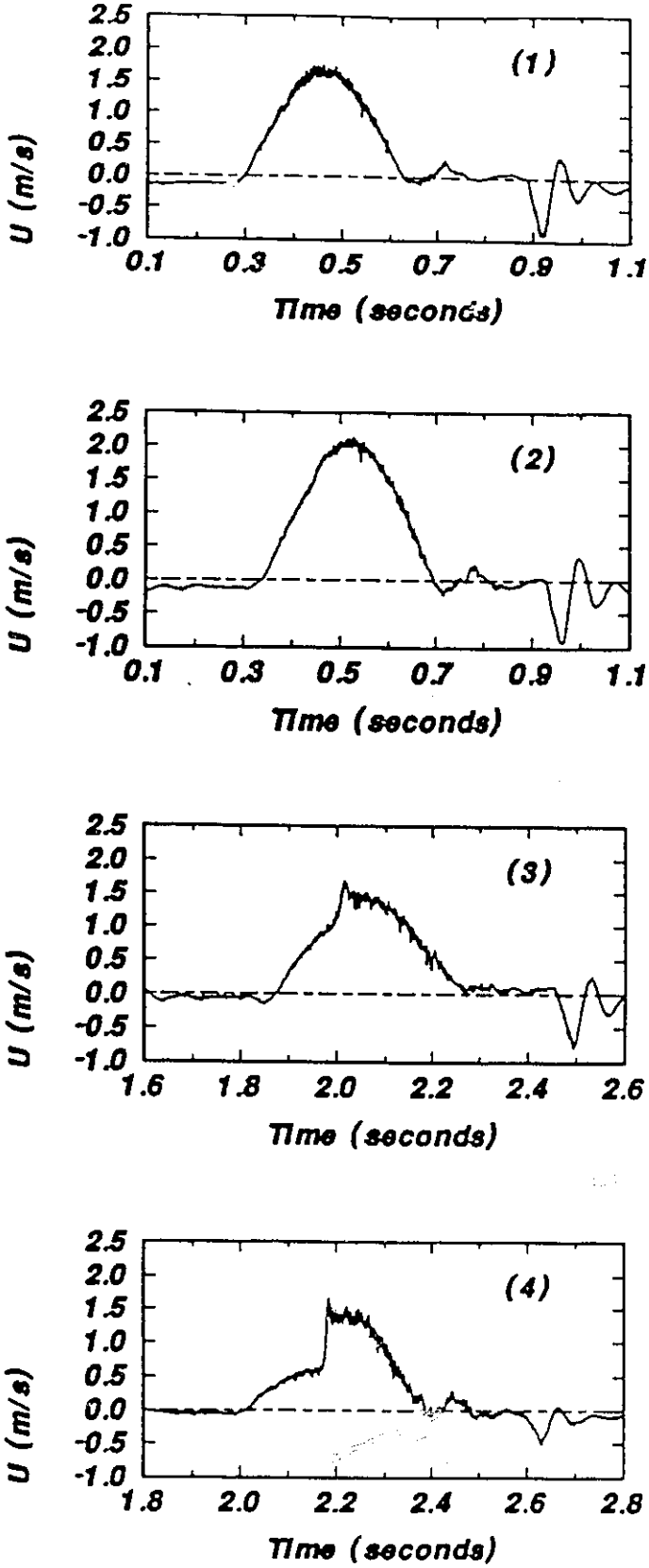

Figure 6.12: Axial Velocity Variation at Four Stations along the Axis of the Test Section: (1) At Profile 1, (2) At Profile 3, (3) At Profile 7, (4) At Profile 11.

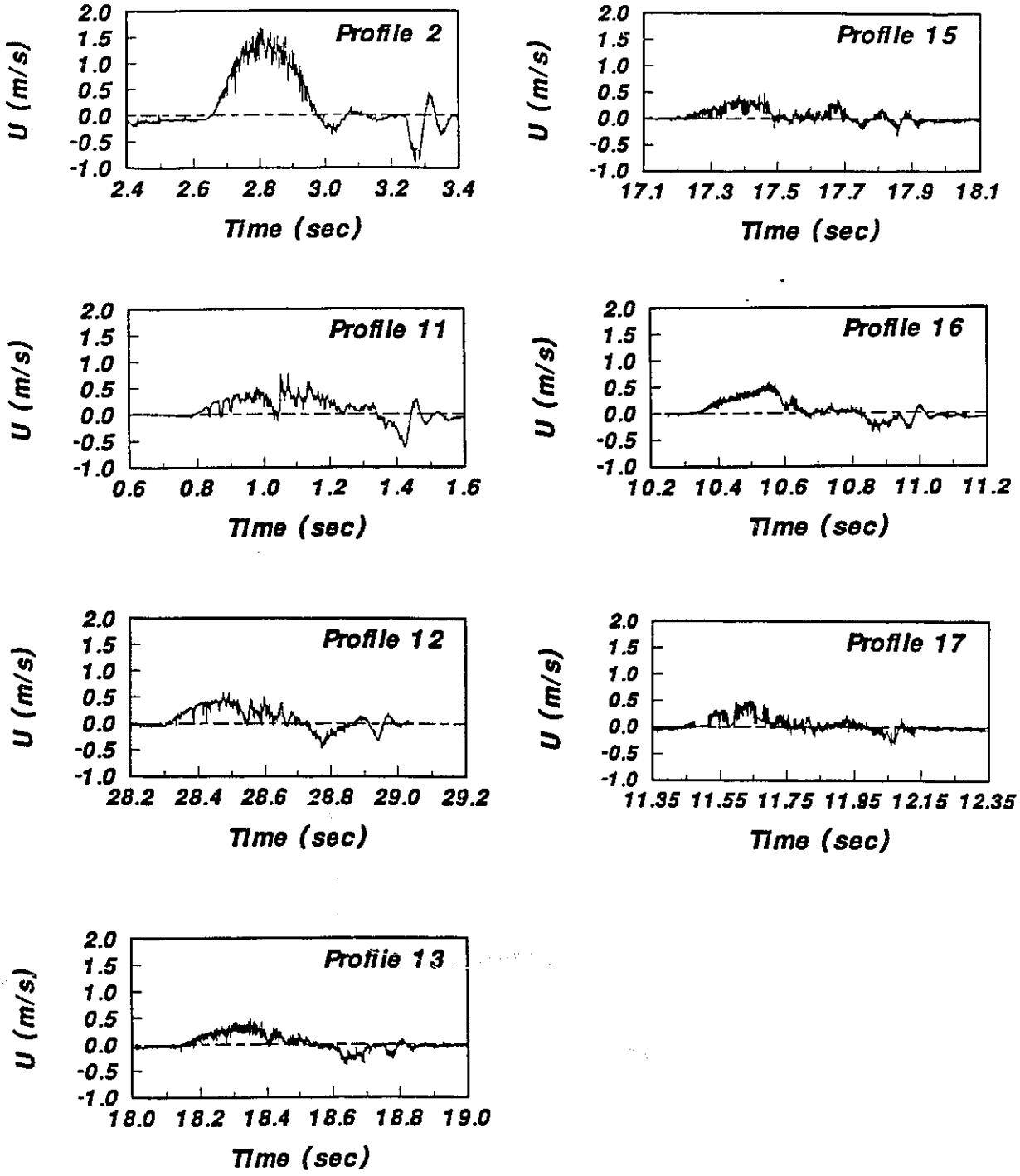

Figure 6.13: Axial Velocity Variation near the Wall Region for Profiles 2, 11, 12, 13, 15, 16 And 17.

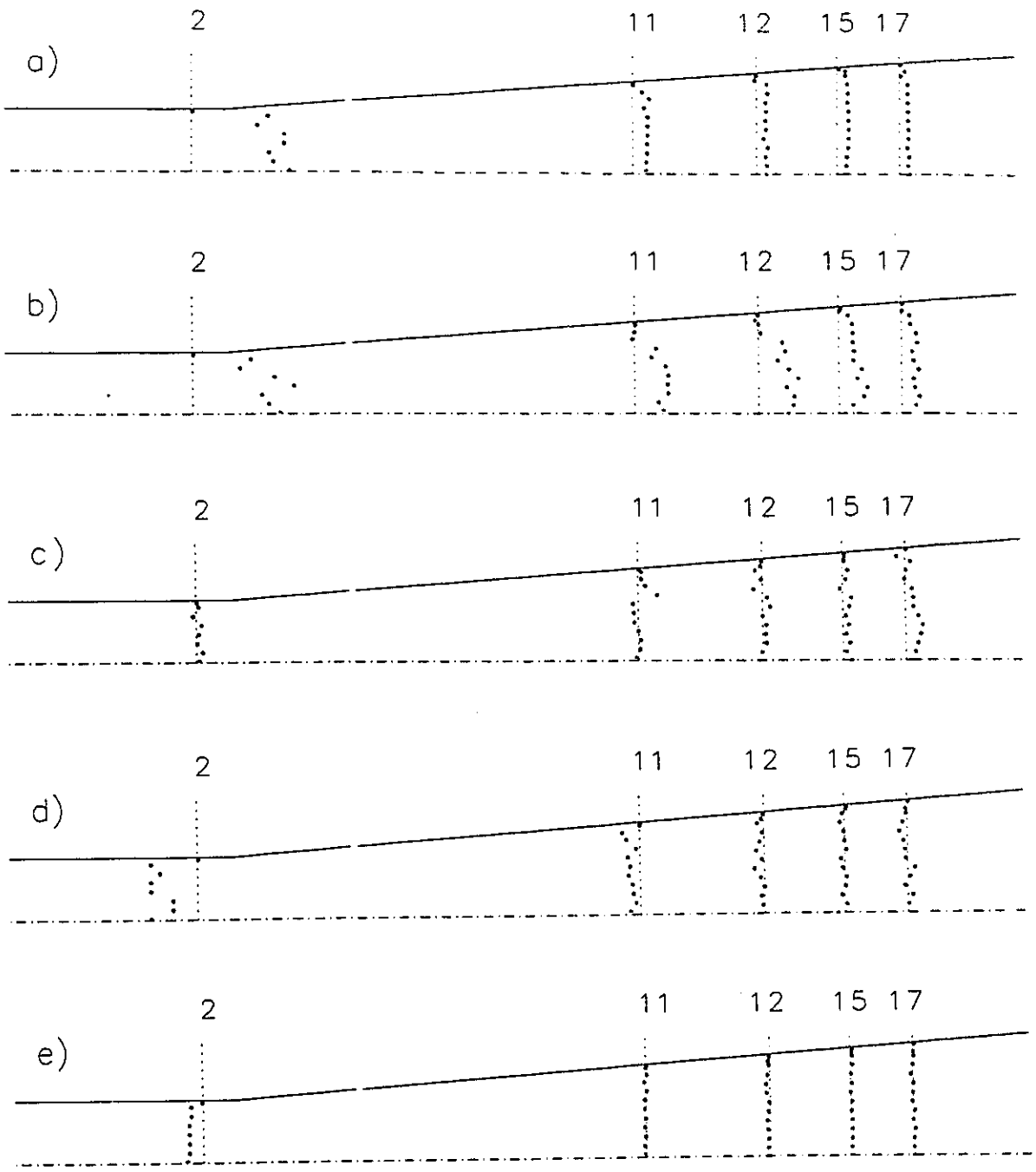

Figure 6.14: Axial Velocity profiles 2, 11, 12, 15 and 17 at different times: a) At t3, b) At t5, c) At t10, d) At t13 and e) At t18.

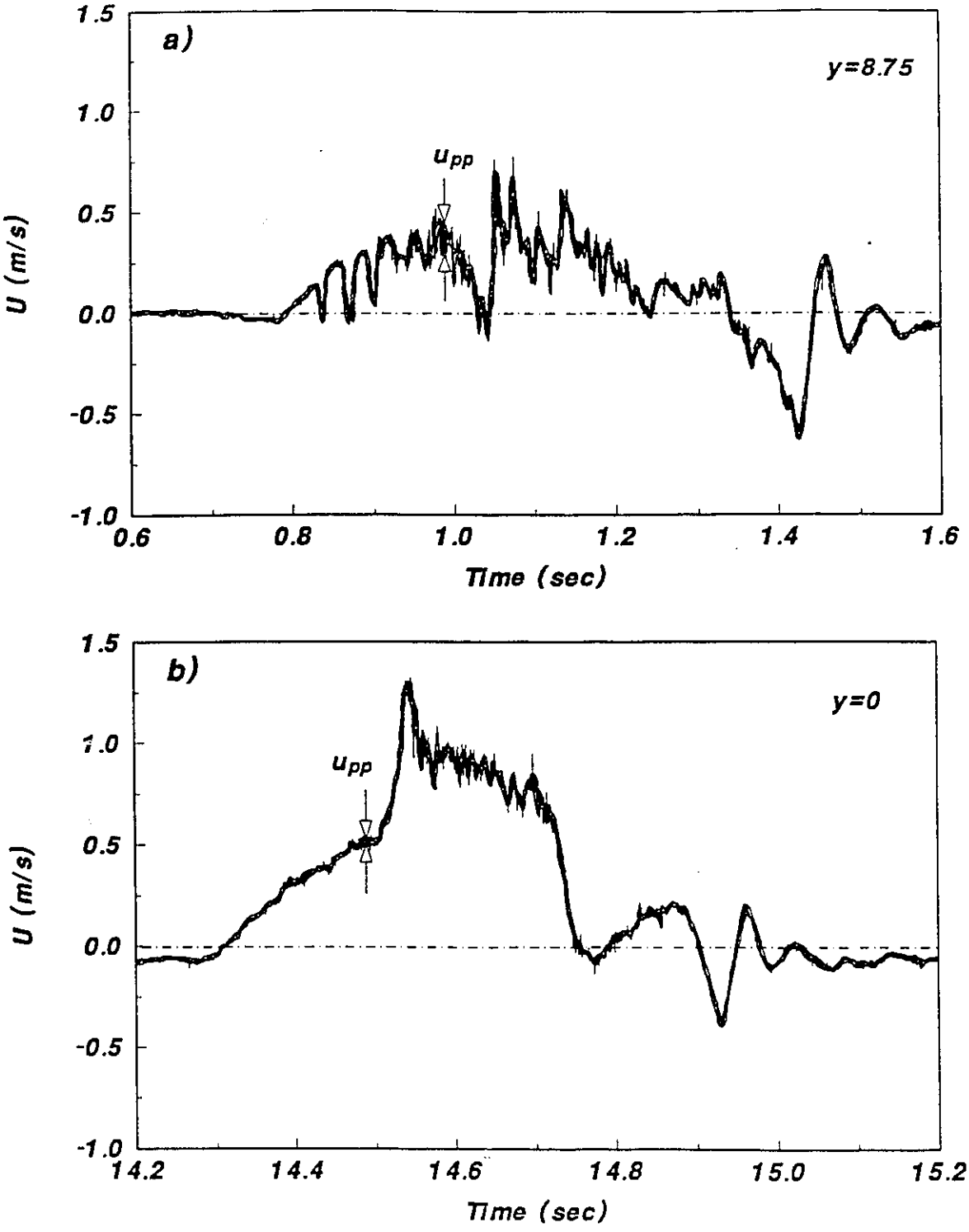

Figure 6.15: Envelope Used to Find Axial Velocity Fluctuations, e.g. Profile 11: a) Near the Wall and b) At the Centerline.

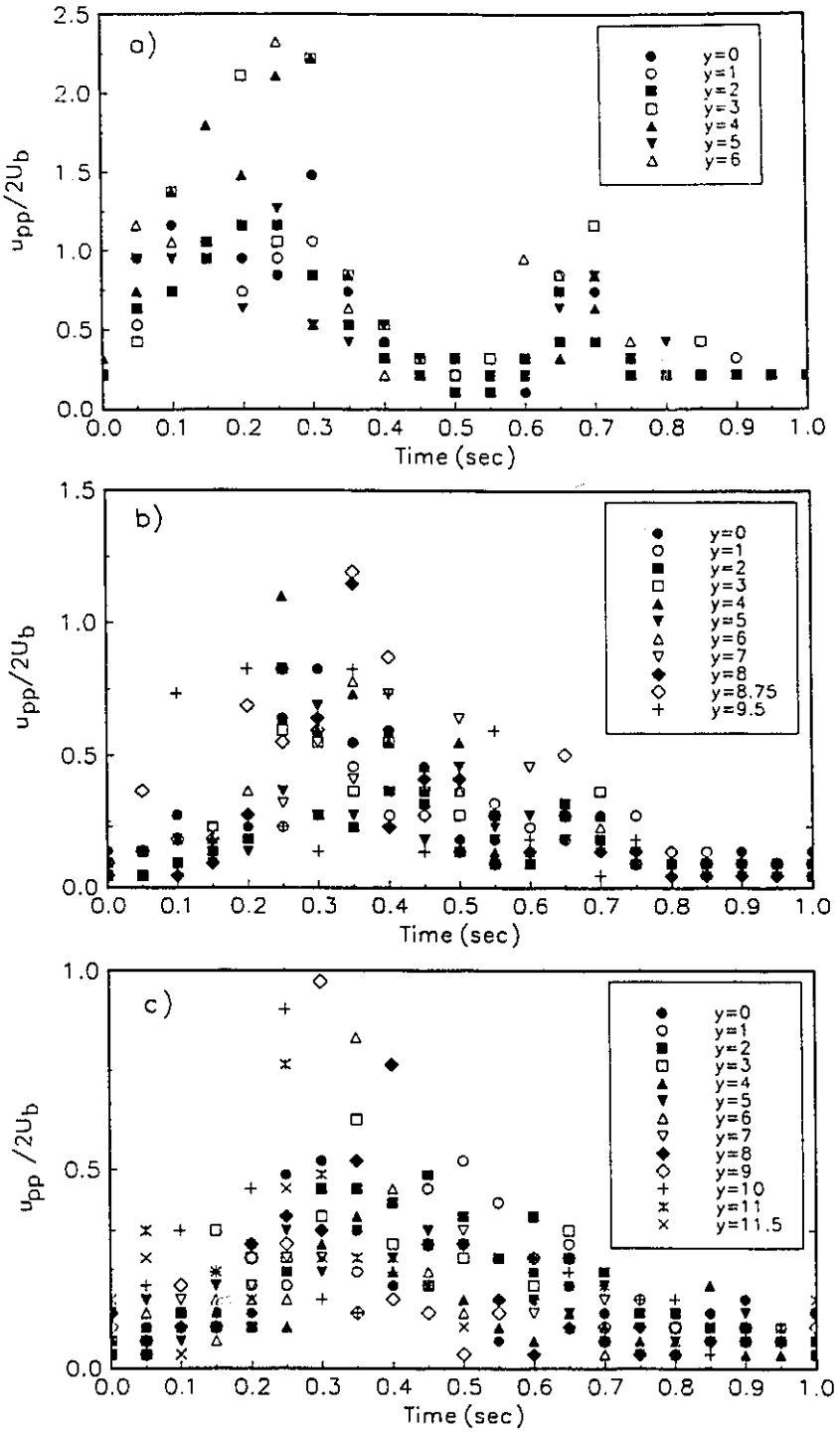

Figure 6.16: Axial Velocity Fluctuations for a) Profile 2, b) Profile 11 and c) Profile 17.

Appendix A

Basics of the LDA Technique

A.1 Doppler Shift

The LDA principle to determine velocities in a flow is based on the physical phenomenon known as the Doppler shift: in any form of wave propagation, frequency changes occur due to the movement of the source, receiver, propagating medium, or intervening reflector or scatterer. These shifts are called "Doppler shifts".

There are two commonly used techniques (or modes) of operation of the LDA. One is called the Reference Beam technique (also called Optical Beating technique) and the second is called the Differential Doppler technique. The Reference Beam technique uses the principle of heterodyning or "beating" of the two frequencies in a device having a non-linear response. Laser beams are heterodyned by being focussed simultaneously on a light detector. The output of the detector then contains a component of the difference or heterodyne beat frequency. A simple illustration of the use of this technique is shown in figure A.1. The Differential

Doppler technique uses instead two beams of equal intensity, which are focused and crossed at the point of measurement. In this experiment, the Differential Doppler technique is used because it provides a good signal to noise ratio for low scattered light intensity and it does not require alignment of the photomultiplier with the optical unit as it is the case for the other technique. In brief, the operating principle of the Differential Doppler technique involves focusing laser beams at a small volume surrounding the point under investigation (as mentioned earlier) and then sensing with a photomultiplier the light scattered by tiny particles carried along with the fluid as it passes through the laser focal volume. The velocity of the particles (assumed to be identical to the fluid velocity) causes a doppler shift of the scattered light's frequency and produces a photomultiplier signal directly related to the velocity. Figure A.2 shows a basic LDA configuration using the Differential Doppler technique. Figures A.3 and A.4 give some details on this technique. The frequency, f, of the signal (shown in figure A.4) produced by a particle moving across the dark and light fringe pattern with a velocity V normal to the fringes is given by

$$f = \frac{2V \sin \frac{\theta}{2}}{\lambda} \tag{A.1}$$

where λ is the laser light wavelength and θ is the angle of intersection of the laser beams.

A.2 Photomultiplier Signal

Photomultipiers are vacuum tubes in which electrons are released by light (scattered light collected from the measuring volume) falling on a special photoemissive surface. These electrons are collected by a positive electrode (anode) to produce a measurable current. Most photomultipliers have their highest sensitivity in the blue and green regions of the spectrum, which overlap with the colors of the laser used in this investigation. The two photomultipliers used are mounted in a backward scatter mode. To explain the effect of the particle path through the control volume on the photomultiplier signal, figure A.5 shows two particles crossing the control volume at different paths. The particle crossing through the center of the fringe pattern formed by the intersecting beams of equal intensity gives the ideal photomultiplier signal shown in figure A.6a. It has the maximum depth of modulation possible, corresponding to the high fringe contrast in the central region. When the two intersecting beams have different intensity, or the particle is not small compared with the fringe spacing, one ends up with an imperfectly modulated signal, as shown in figure A.6b. The intensity variation shown in figure A.6c is due to the particle P_2 (figure A.5) following a path off-center. Besides, there is always a low frequency component of intensity variation (shown by the dashed lines in figure A.6) in addition to the burst of differential Doppler frequency. It is called the 'pedestal' and it is an undesired signal, which is normally eliminated by using a high-pass filter. However, if the frequency of the pedestal signal is close to that of the measured signal, it is very hard to distinguish between the

two signals. Another complication of the photomultiplier signal arises when the number of particles crossing the scattering volume changes. Figure A.7 shows the difference in the photomultiplier signals in the cases of one or several particles crossing the scattering volume. In the present work several particles are assumed to be crossing the scattering volume at the same time. However, the above complications are eliminated when the photomultiplier is used along with the PDA system.

A.3 Frequency Shifting

The basic LDA velocity-Doppler frequency relationship can not discriminate the direction of the velocity because, as shown in figure A.8, positive and negative velocities of the same magnitude correspond to the same Doppler frequency. Frequency shifting is the most convenient method to solve this problem by accounting for flow reversal. The use of a frequency shift has a number of advantages. It requires only one channel of reception and no major modifications to the optics and signal processing equipment. It enables velocity fluctuations to be followed smoothly through zero and it is not affected by depolarization on scattering.

In the present investigation, frequency shifting was applied to the differential Doppler technique, so that one laser beam was shifted by a frequency f_s, as shown in figure A.9. This results in a system of fringes in the control volume that moves

with a velocity

$$U_s = f_s S \tag{A.2}$$

where S is the distance between two fringes. Therefore, a stationary particle within the illuminated volume produces a signal of frequency equal to f_s. Movement in the same direction as the fringes lowers the frequency of the Doppler signal and movement in the opposite direction it raises it. There are several techniques used to produce this optical frequency shift. The one used in this experiment is the most popular technique and uses an acousto-optic cell, known as a Bragg Cell. A light beam from the laser is passed into a cell containing material in which acoustic waves are travelling. These are excited by a suitable piezoelectric transducer and diffracted beams are produced. If the angle between the light beam and the acoustic wave satisfies the so-called Bragg condition

$$\sin(\frac{\alpha}{2}) = \frac{\lambda}{2\lambda_A} \tag{A.3}$$

where $\frac{\alpha}{2}$ is the Bragg angle, λ_A is the acoustic wavelength and λ is the optical wavelength, reflections from successive acoustic wave fronts are reinforced. The Bragg cell used in this work produces a frequency shift of the laser beam frequency of around 40 MHz.

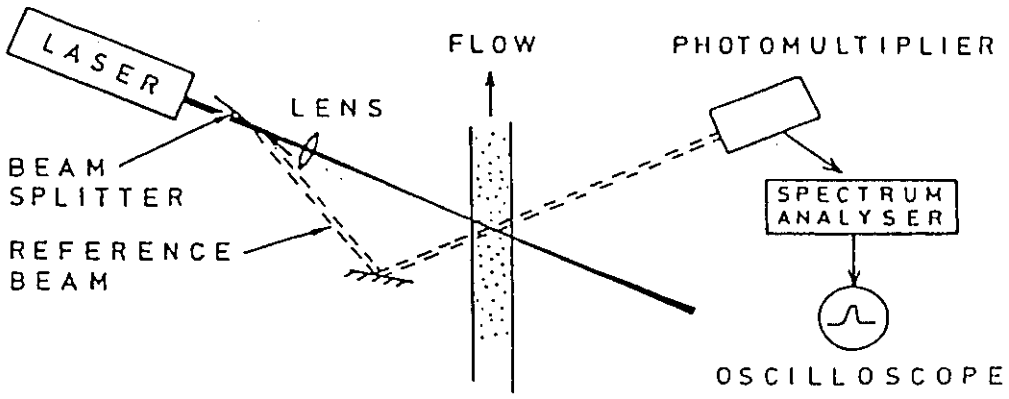

Figure A.1: A Basic Laser Doppler Configuration Using Reference Beam Technique for Heterodyning the Scattered Light (Drain, 1980).

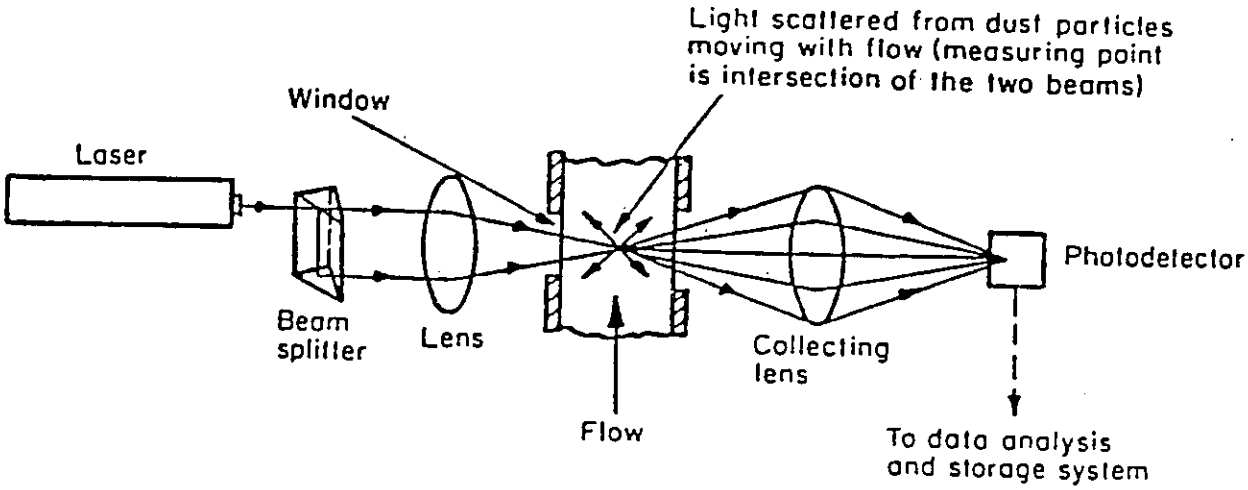

Figure A.2: Basic LDA Configuration Using the Differential Doppler Technique.

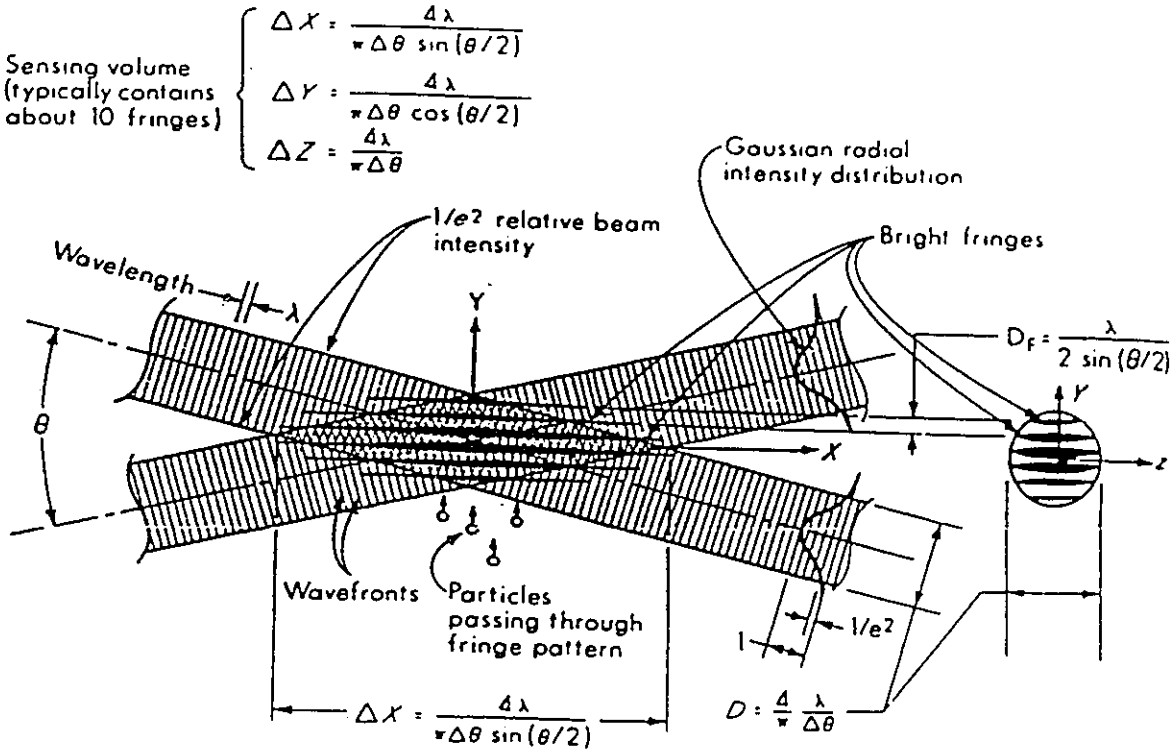

Figure A.3: Interference Fringes in the Sensing Volume (Doebelin, 1990).

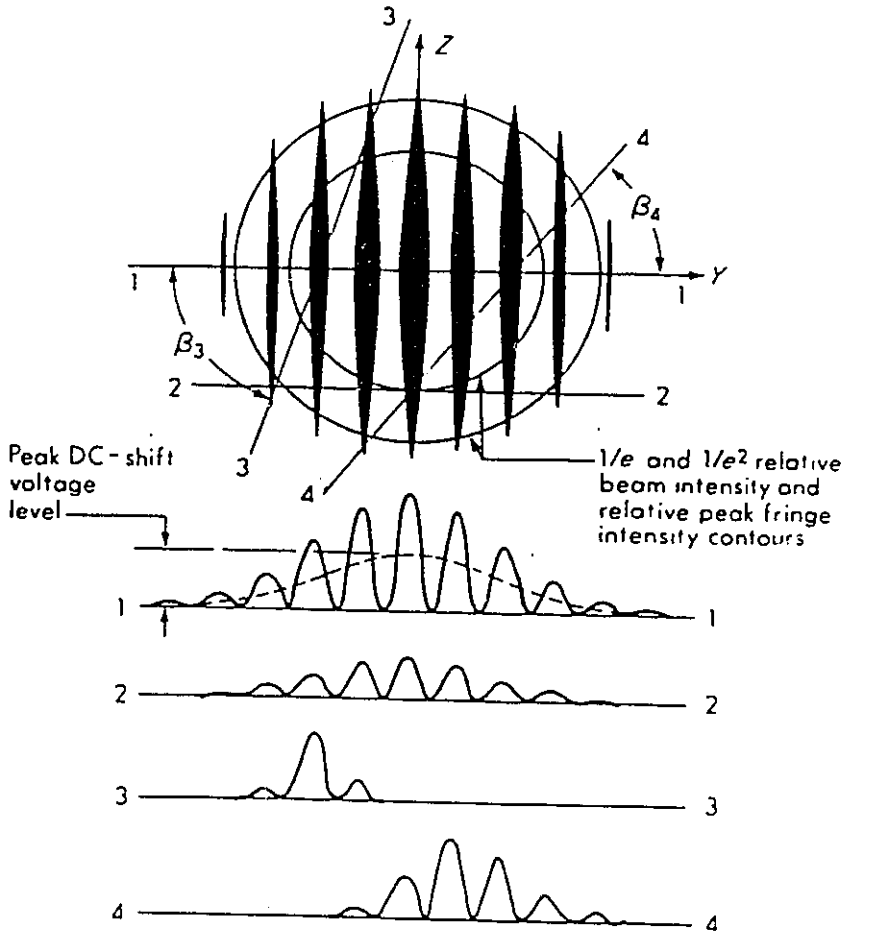

Signal amplitude vs particle position near $X = 0$ for a number of particle trajectories. The indicated fringe width is proportional to the local peak fringe intensity

Figure A.4: Photomultiplier Signals for a Number of Particle Trajectories (Doebelin, 1990).

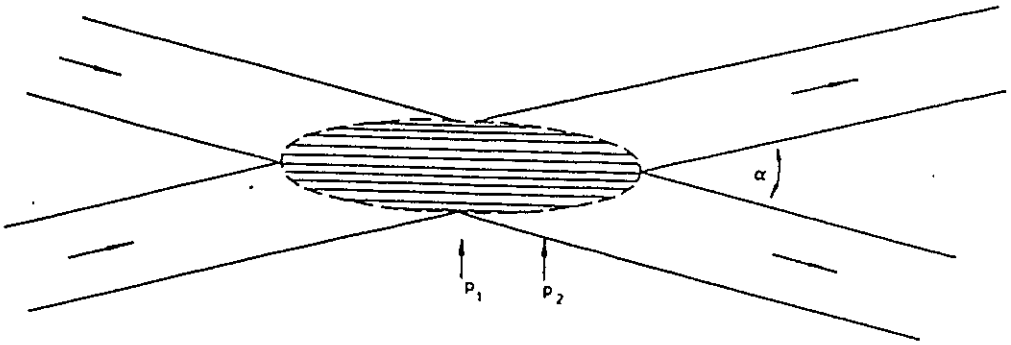

Figure A.5: Fringe Pattern Produced by Crossing Beams in the Differential Doppler Technique (Drain, 1980).

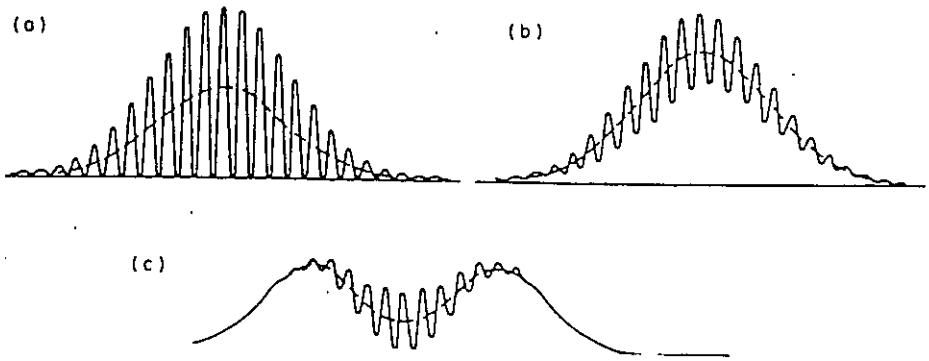

Figure A.6: Types of Signal from Particles Crossing a Region of Intersection of the Light Beams (Drain, 1980).

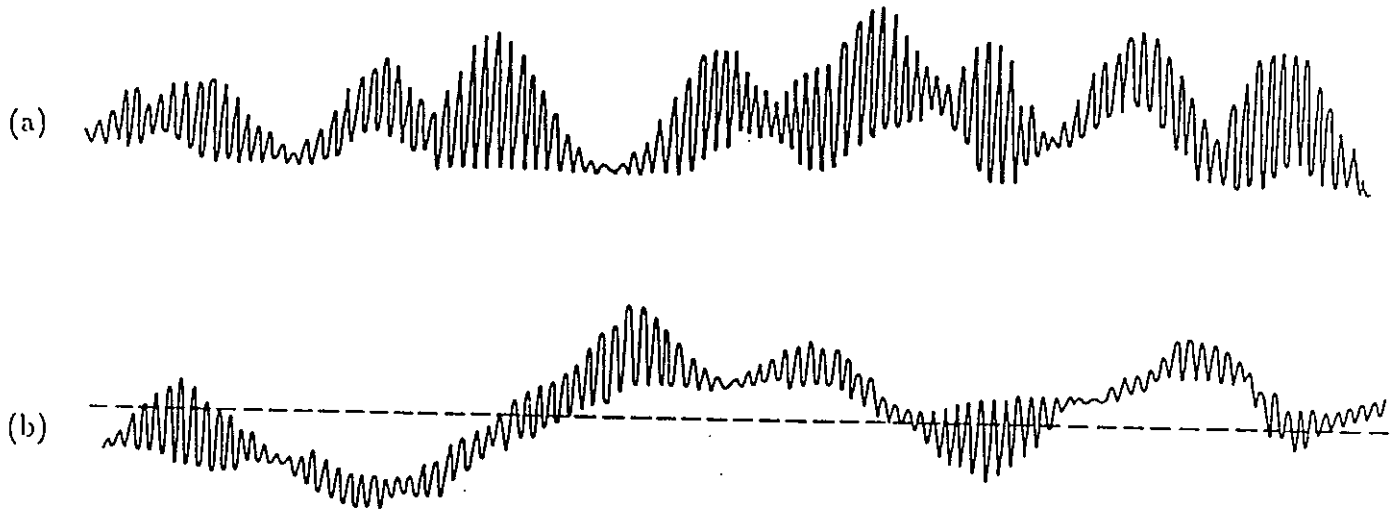

Figure A.7: Photomultiplier Signal: (a) One Particle Present at the Control Volume; (b) Several Particles Present at the Control Volume (Drain, 1980).

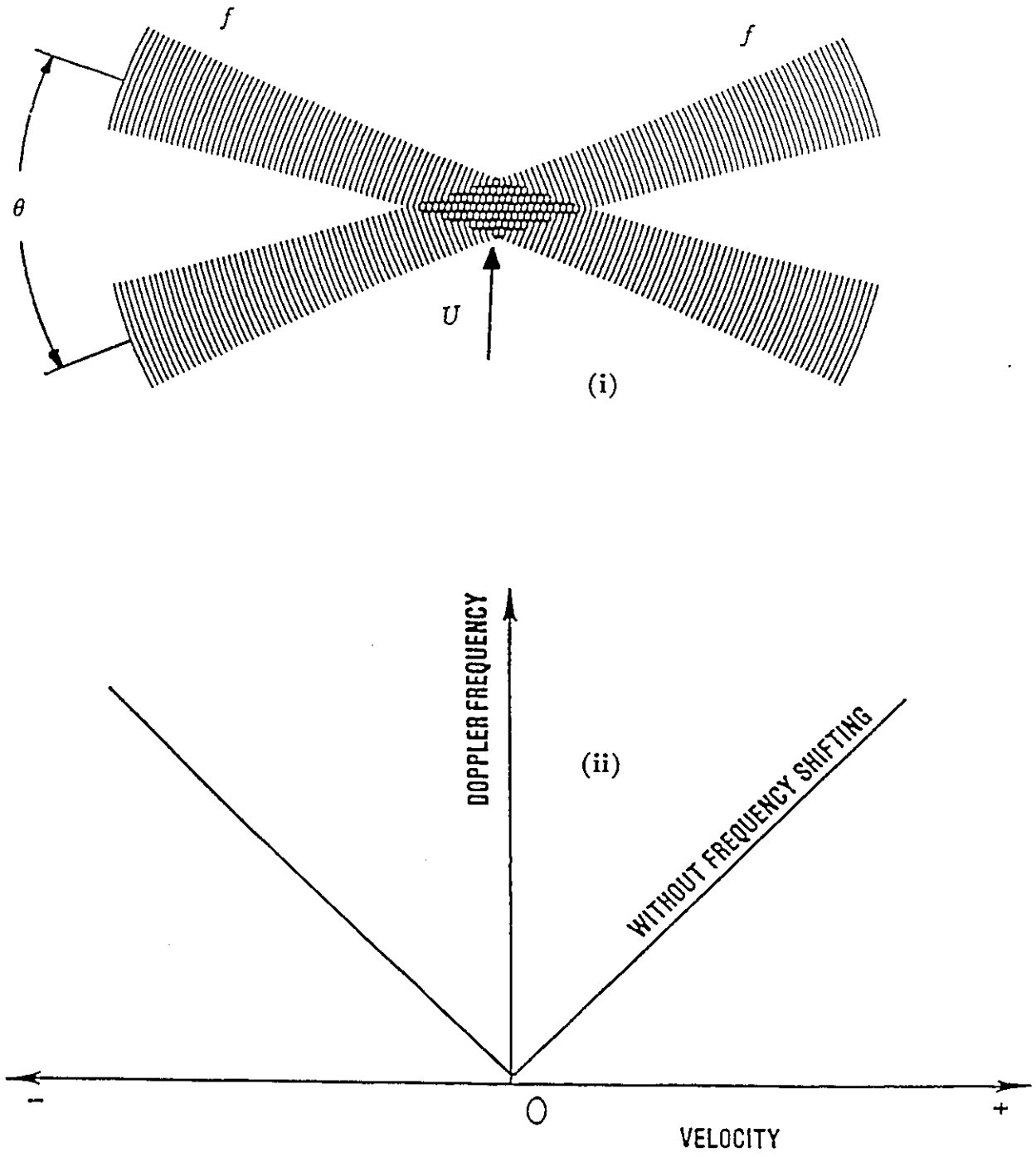

Figure A.8: No Frequency Shift: (i) Fringes in Beam Intersection; (ii) Frequency-Velocity Curve.

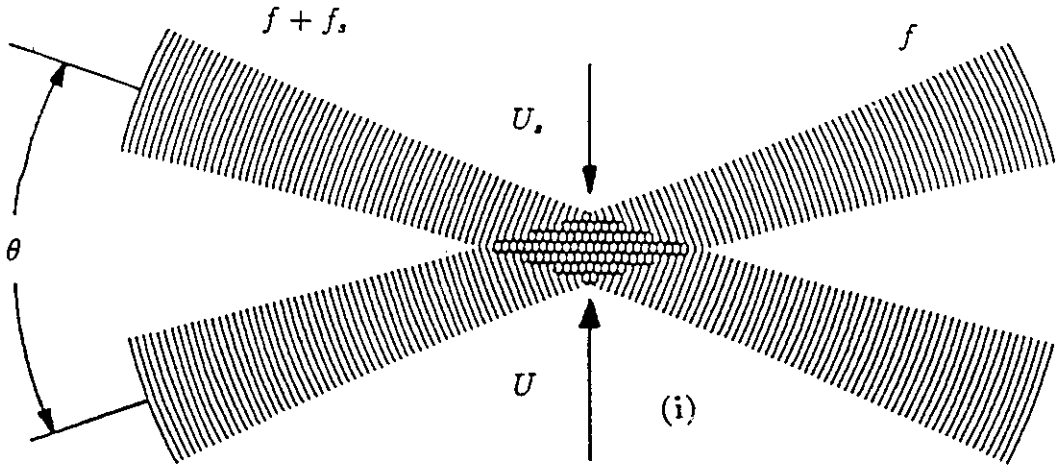

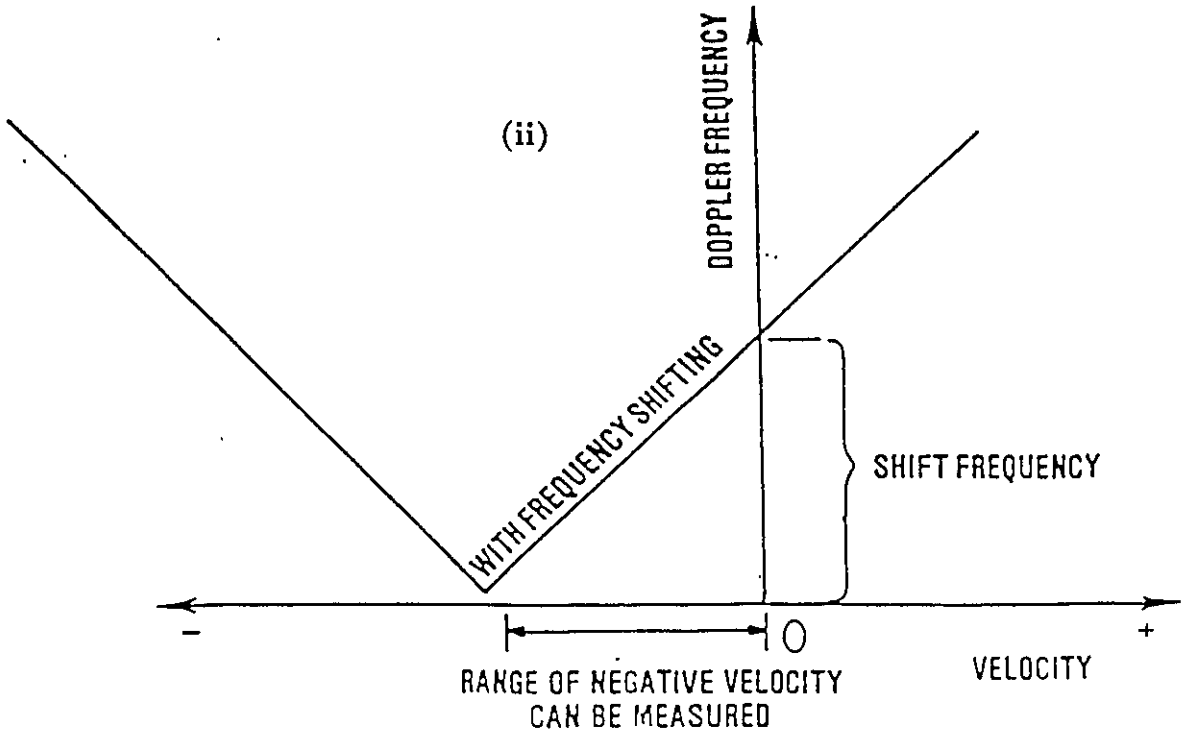

Figure A.9: With Frequency Shift: (i) Fringes in Beam Intersection; (ii) Frequency-Velocity Curve.

Appendix B

Refractive Index Matching for Velocity Measurements with the LDA

For the use of LDA in a flow system where all the material interfaces in the path of the laser beams are plane, it usually suffices to use walls of transparent materials and a transparent fluid with a uniform index of refraction. However, if the interfaces are curved, one should take some measures to avoid distortion of the optical path. For complex geometries, the laser beam path could be very complicated, and therefore one should not only make the object of transparent material, but also use a fluid whose index of refraction matches that of the object.

B.1 Problems Caused by Mismatch of the Index of Refraction

The effect of a mismatch in index of refraction will be discussed here primarily in terms of ray tracing and Snell's law. Snell's law for a ray crossing an interface marking a step change in the index of refraction, as shown in figure B.1a, is:

$$n_1 \sin\theta_1 = n_2 \sin\theta_2 \tag{B.1}$$

where n_1 and n_2 are the indices of refraction on sides 1 and 2 respectively, θ_1 is the angle of incoming ray at the point of incidence and θ_2 is the angle of outgoing ray at the same point . If $n_1 > n_2$, then there exists an incidence angle, θ_{1c}, for which the ray can not cross the interface at all. This critical angle is given by the relationship

$$\sin\theta_{1c} = \frac{n_2}{n_1} \tag{B.2}$$

Any ray with $\theta_1 > \theta_{1c}$ will not cross the interface. Therefore, even if the optical surfaces are plane, it may be necessary to adjust the indices of refraction to gain optical access.

B.1.1 Plane Interfaces

Consider two rays of light at different angles, crossing the plane interface between two media with different indices of refraction, as shown in figure B.1b. In

this figure O' is the point of apparent intersection and O is the point of actual intersection. Using simple geometrical arguments, one can see that

$$\frac{L'}{L} = \frac{\tan\theta_2}{\tan\theta_1} = f(\frac{n_1}{n_2}, \theta_1) \tag{B.3}$$

where θ_2 is found by Snell's law.

If one attempts to move the intersection point while keeping the angle θ_1 constant, one can see that

$$\frac{dL}{dL'} = f(\frac{n_2}{n_1}, \theta_1) \tag{B.4}$$

The measurement volume of LDA is displaced from its apparent intersection, and, if one moves the intersection of the beams, the displacement depends on the index of refraction mismatch.

The problem becomes more complicated if the angles that the rays make with the walls are not equal, as shown in figure B.1c. Again the point of intersection of the two rays moves with respect to the point of apparent intersection. One can easily see that

$$\frac{L}{L'} = \frac{\tan\theta_{11} - \tan\theta_{12}}{\tan\theta_{21} - \tan\theta_{22}} \tag{B.5}$$

$$\frac{Y}{Y'} = \frac{\left(\frac{\tan\theta_{11}}{\tan\theta_{12}} - 1\right)}{\left(\frac{\tan\theta_{21}}{\tan\theta_{22}} - 1\right)} \tag{B.6}$$

where θ_{21} and θ_{22} are found from Snell's law.

The position of the intersection is a nonlinear function of the input angles, even for a plane interface. Furthermore, the bisection angle at the intersection changes. This means that in laser anemometry, the measured velocity component would not be equal to the one that would have been measured in the absence of

the interface, as

$$\tan\theta_s = \frac{L}{L'}\tan\theta_s' + \frac{(Y' - Y'')}{L} \tag{B.7}$$

where θ_s is the bisection angle in the presence of interface and θ_s' is the bisection angle in the absence of interface.

There is one more complication caused by the mismatch of the index of refraction. If a third ray at a different angle is passed through the interface that would have intersected the other beams at O' in the absence of the interface, it may not have a common intersection with the two other beams in the presence of the interface. Each pair of beams may intersect, but there may not be a common intersection. Therefore, a two-component LDA with three-beam arrangements aligned with the intersection in medium 1 will not necessarily be aligned when the rays cross into medium 2 (Edwards and Dybbs, 1984).

It can be shown that, to first order, the size of the beam waist of a laser beam focussed through an interface has the same size as in medium 1, but its position is shifted along the beam by the ratio $\frac{n_2}{n_1}$. If $n_2 > n_1$ the position of the waist is shifted further away from the intersection of the beam with the interface by $\frac{n_2}{n_1}$. The distance is shortened by the same amount if $n_2 < n_1$. Given the nonlinear behavior of the position of beam intersections, it is possible that the beam waists of an LDA system may not be at the intersection point.

B.1.2 Curved Interfaces

As shown in figure B.1d, problems due to light refraction are more severe with curved interfaces. A curved interface acts like a poor lens, bending the rays toward or away from the axis, depending on the relative values of n_1 and n_2. Refraction also depends on the height of intersection above the horizontal axis (h), as

$$\sin\theta_2 = \frac{n_1}{n_2}\frac{h}{R} \tag{B.8}$$

Curved interfaces can even cause rays that enter parallel to intersect in medium 2. However, two pairs of rays would, in general, not intersect at the same point. Rays that would have intersected, if solely contained in medium 1, may still intersect in medium 2, but again the location of the intersection would be moved.

If $n_1 > n_2$, there would be some rays that would never enter the medium 2, because their angles with the normal surface would be greater than θ_{1c}. The height above the axis, h, above which no rays would enter is given by:

$$h = R\frac{n_2}{n_1} \tag{B.9}$$

Likewise, if $n_2 > n_1$, a ray parallel to the horizontal axis in medium 2 would not be able to exit at heights higher than

$$h = R\frac{n_1}{n_2} \tag{B.10}$$

If a parallel set of rays intercepts the interface of a cylinder or a sphere, there would be regions of the surface where no rays would cross the interface. The frac-

tion of the radius outside of this zone is given by the ratio of indices of refraction, which must be less than 1.

For a simple curved surface, computation of the position of intersection, if any, of two rays can be complicated. For the more complicated curved surfaces encountered in some flows, the calculations would indeedbe formidable.

B.1.3 Effect of the Ratio $\frac{n_1}{n_2}$

In the present investigation, the interior of the test section is conical while its exterior is prismatic. Therefore, the above described effects on the intersection of the laser beams would be present and as a consequence the velocity measurements would be affected. These problems can be mitigated by making the ratio $\frac{n_1}{n_2}$ close to unity. In other words, to avoid distortions, one should choose a working fluid with an index of refraction that matches that of the material of the test section (Plexiglas).

B.2 Refractive-Index Matching Technique

The refractive index matching of a solid material and a liquid solution or mixture can be achieved as follows. First, a laser beam is passed through the liquid at a given composition and temperature and the spot where it hits the target is

marked (see figure B.2). Then a rod of the same material as the test section is inserted in the liquid so that the laser beam crosses it. The deflection of the beam from the target (placed at a position 3 m away from the rod) is marked. The temperature and/or the composition of the liquid is adjusted until the laser beam shows no deflection.

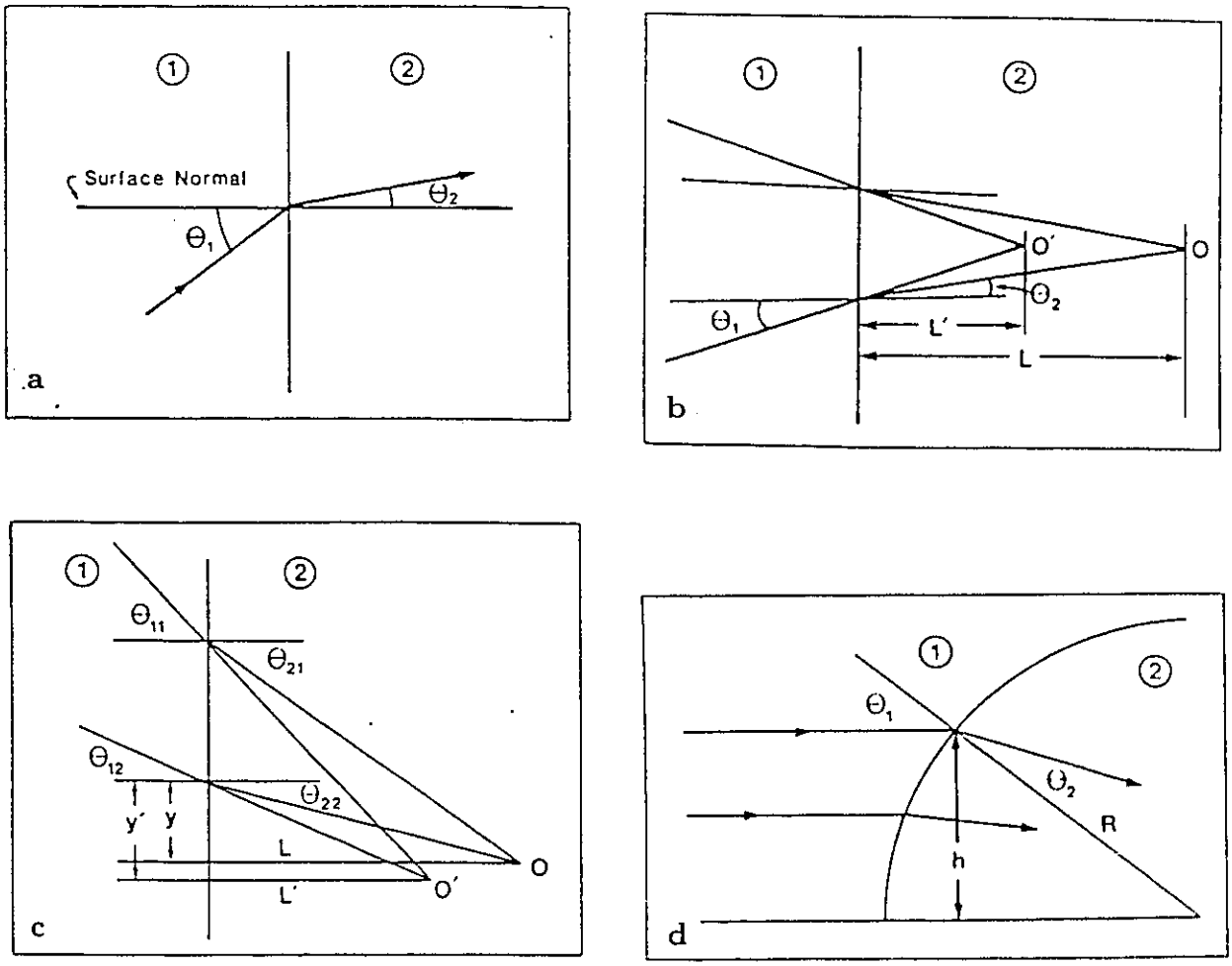

Figure B.1: Different Cases of Light Rays Crossing the Interface between Media having Different Indices of Refraction.

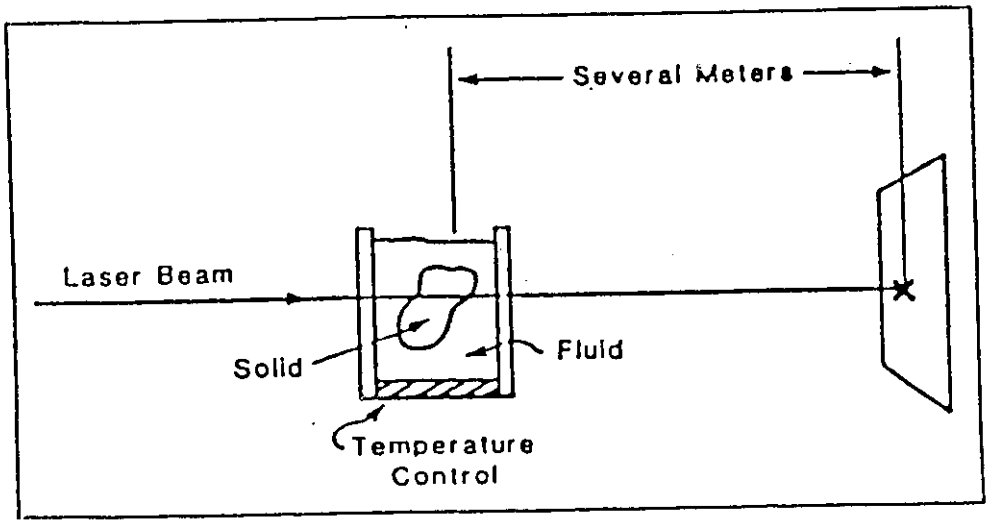

Figure B.2: Schematic of Refractive Index Matching Procedure.